

University of Warwick institutional repository: <http://go.warwick.ac.uk/wrap>

A Thesis Submitted for the Degree of PhD at the University of Warwick

<http://go.warwick.ac.uk/wrap/74315>

This thesis is made available online and is protected by original copyright.

Please scroll down to view the document itself.

Please refer to the repository record for this item for information to help you to cite it. Our policy information is available from the repository home page.



**Fabrication of TiNi Shape Memory Alloy Microactuators
By Ion Beam Sputter Deposition**

**Author : Kazuyoshi Tsuchiya B. Eng, M. Eng
Supervisor : Dr. S. T. Davies**

**Centre for Nanotechnology and Microengineering, School of Engineering,
University of Warwick**

LIST OF FIGURES.....	5
LIST OF TABLES	10
ACKNOWLEDGEMENT	11
DECLARATION.....	12
ABSTRACT	13
LIST OF ABBREVIATIONS	14
1 INTRODUCTION	17
1.1 BACKGROUND TO THIS WORK.....	17
1.1.1 <i>Micro Electro Mechanical Systems (MEMS)</i>	17
1.1.2 <i>Microfabrication strategies</i>	19
1.2 SHAPE MEMORY ALLOYS.....	20
1.2.1 <i>Shape memory effect</i>	21
1.2.2 <i>TiNi shape memory alloys</i>	22
1.2.3 <i>Application of shape memory alloys</i>	24
1.3 MOTIVATION AND PURPOSE OF THIS WORK.....	25
2 APPARATUS AND PRINCIPLES OF ION BEAM DEPOSITION TECHNIQUES.....	29
2.1 SHOWERED ION BEAMS AND THE KAUFMAN ION SOURCE	29
2.2 PRINCIPLES OF ION BEAM SPUTTERING.....	33
2.2.1 <i>General overview of ion beam sputtering</i>	33
2.2.2 <i>Mechanism of sputtering</i>	35
2.3 SPUTTERING PHENOMENA	37
2.3.1 <i>Sputtering yield</i>	37
2.3.2 <i>Ion energy</i>	38
2.3.3 <i>Angle of incidence effects</i>	39
2.4 PRINCIPLE OF ION BEAM DEPOSITION	41
2.4.1 <i>RF and DC sputter deposition</i>	41
2.4.2 <i>Magnetron sputter deposition</i>	44
2.4.3 <i>Ion beam sputter deposition</i>	47
2.5 SUMMARY.....	48
3 SIB SOURCE CHARACTERISATION	50
3.1 INTRODUCTION	50

3.2	CURRENT DENSITY	51
3.2.1	<i>Current density as a function of distance from the ion source</i>	52
3.2.2	<i>Effect of accelerator voltage on current density</i>	53
3.3	BEAM PROFILE	55
3.3.1	<i>Beam profile variations with various grid types</i>	55
3.3.2	<i>Effect of grid type on current density</i>	58
3.4	SUMMARY	59
4	ION BEAM SPUTTER DEPOSITION	62
4.1	INTRODUCTION	62
4.2	ARRANGEMENT OF APPARATUS FOR IBSD	63
4.3	TARGET AND SUBSTRATE TEMPERATURE AS A FUNCTION OF SPUTTERING	64
4.4	OPERATING CONDITIONS FOR THIN FILM DEPOSITION BY ION BEAM SPUTTERING	66
4.4.1	<i>Sputtering yield from targets of Al, Ti and Ni</i>	66
4.4.2	<i>Relationship between film thicknesses, beam voltages and beam current</i>	68
4.5	TITANIUM-NICKEL (TiNi) ALLOYS	71
4.5.1	<i>TiNi thin film</i>	71
4.5.2	<i>Target of Ti/Ni</i>	71
4.5.3	<i>TiNi thin films produced by SIB</i>	73
4.6	SUMMARY	74
5	CHARACTERISATION OF TiNi SHAPE MEMORY ALLOY THIN FILMS	77
5.1	INTRODUCTION	77
5.2	PROPERTIES OF TiNi SHAPE MEMORY ALLOYS	77
5.2.1	<i>Crystal structure of martensitic phase</i>	77
5.2.2	<i>Shape memory effect</i>	79
5.2.3	<i>Electrical and thermal characterisation of TiNi</i>	82
5.3	DEPOSITION OF TiNi SHAPE MEMORY ALLOY THIN FILMS	83
5.3.1	<i>Annealing temperature of TiNi shape memory alloy deposited by magnetron sputtering</i>	84
5.3.2	<i>Conditions for IBSD, compared with magnetron sputtering</i>	85
5.4	TiNi THIN FILM CHARACTERISATION BY X-RAY REFLECTOMETRY	87
5.4.1	<i>Physical principles of X-ray reflectometry</i>	88
5.4.2	<i>Characterisation of TiNi thin films</i>	90
5.5	ELECTRICAL CHARACTERISATION OF TiNi THIN FILMS	92
5.5.1	<i>Resistivity of TiNi thin films</i>	92
5.5.2	<i>Resistance of TiNi thin films</i>	94

5.6 SUMMARY.....	97
6 THERMAL CHARACTERISATION OF TINI SMA THIN FILMS.....	99
6.1 INTRODUCTION	99
6.2 THERMAL MODELLING	100
6.3 THERMAL CHARACTERISATION OF TINI SHAPE MEMORY ALLOYS.....	105
<i>6.3.1 Radiative heat transfer coefficient</i>	<i>105</i>
<i>6.3.2 Temperature - time profiles measurements.....</i>	<i>107</i>
<i>6.3.3 Thermal Imaging</i>	<i>108</i>
6.5 SUMMARY.....	116
7 TINI MICROACTUATORS : TECHNOLOGY, FURTHER WORK AND CONCLUSIONS	
.....	119
7.1 INTRODUCTION	119
7.2 DEVICE SCALING.....	119
<i>7.2.1 Introduction.....</i>	<i>119</i>
<i>7.2.2 Effect of scaling.....</i>	<i>120</i>
<i>7.2.3 Summary.....</i>	<i>123</i>
7.3 FOCUSED ION BEAM TREPANNING.....	123
<i>7.3.1 Introduction.....</i>	<i>123</i>
<i>7.3.2 Focused ion beams.....</i>	<i>125</i>
<i>7.3.3 Production of micro-parts by FIB.....</i>	<i>125</i>
7.4 FUTURE WORK	130
<i>7.4.1 Out-of-plane 3-D microstructures.....</i>	<i>130</i>
<i>7.4.2 Summary.....</i>	<i>133</i>
7.5 CONCLUSIONS.....	133
REFERENCES	136
BIBLIOGRAPHY	145
PAPER PUBLISHED.....	145

List of figures

- Fig.1.1 : Design of SMA microvalve and operation model. P_i denotes inlet pressure (p.19)
- Fig.1.2 : Thin film deposition process (p.20)
- Fig.1.3 : Temperature effect for shape memory alloy by L.M.Schetky (p.22)
- Fig.1.4 : Silicon micromachined proportional valve by MicroFlow,Inc (p.24)
- Fig.2.1 Schematic diagram of showered ion beam equipment
(a) showered ion beam system, (b) showered ion beam source (p.31)
- Fig. 2.2 : Showered ion beam apparatus (University of Warwick) (a) Kaufman type ion source, (b) Showered ion beam unit and (c) Diffusion pump (p.32-33)
- Fig. 2.3 : Angle of incidence and sputtering yield (p.36)
- Fig. 2.4 : Mechanism of sputter machining (p.37)
- Fig. 2.5 Angular distributions of sputtered particles from polycrystalline targets (p.41)
- Fig. 2.6 : DC and RF sputtering systems, (a) DC sputtering, (b) RF sputtering (p.43)
- Fig. 2.7 : Planar magnetron sputtering system (47)
- Fig. 3.1 : Movable directions of Faraday cup (51)
- Fig. 3.2: Relationship between the current density and accelerator voltage at various distances below ion source with 1000 eV, 20 mA Ar^+ ions (manual mode control) (p.54)
- Fig. 3.3 : Relationship between the current density and total current of a beam

of 1000 eV Ar^+ ions at various distances below the ion source, (automatic mode accelerator grid potential of 300 V) (p.55)

Fig.3.4 : Beam profile of 3 cm SIB source (p.57)

Fig.3.5 : Relationship between beam diameter for 90 % and 80 % uniformity and beam current (p.57)

Fig.3.6 : Effect of grid type on current density (p.59)

Fig.4.1 : Geometrical set-up for deposition (p.64)

Fig 4.2: Target and substrate temperature as a function of sputtering time (p.65)

Fig.4.3 : Relationship between sputtering yield and atomic number for Ar^+ (Selected elements are labelled) (p.67)

Fig.4.4 : Film thickness as a function of source operating voltage and deposition on the substrate (p.69)

Fig.4.5 : Relationship between maximum aluminium film thickness on silicon substrate and source operating voltage (p.70)

Fig.4.6 : Relationship between maximum titanium film thickness on silicon substrate and total beam current (p.70)

Fig.4.7 : Film thickness for TiNi as a function of position (p.72)

Fig.4.8 : Schematic of 8-sector Ti/Ni target (Equal areas of Ti and Ni were used) (p.73)

Fig.4.9 : TiNi film thickness as a function of position (p.74)

Fig.5.1 : Mechanism of shape memory effect (p.78)

Fig. 5.2 : Diagram of resistance curve and transformation temperature for TiNi (p.79)

Fig.5.3 : The stress-strain curve of shape memory alloy and super-elastic alloy (p.81)

Fig.5.4 : Schematic diagram representing the region of shape memory effect and superelasticity in temperature-stress coordinates; (A) represents the critical stress for the case of a high critical stress and (B) represents the critical stress for a low critical stress (p.81)

Fig.5.5 : Schematic diagram of electrical resistivity versus temperature curve (a) and DSC curve (b) of a TiNi shape memory alloy (p.83)

Fig.5.6 : Effect observable from grazing-incident X-ray scattering (p.88)

Fig. 5.7 (a): X-ray intensity versus angle of reflection for grazing angle reflection from TiNi film, where the best fit to the experimental data was obtained by varying the composition for a fixed normalised density of 1.0 (p.91)

Fig.5.7 (b) : X-ray intensity versus angle of reflection for grazing angle reflection from TiNi film. Best fit to the experimental data is obtained by varying the normalised density for a fixed equi-atomic composition (p.92)

Fig.5.8 : Resistivity of TiNi film versus relative position (p.93)

Fig.5.9 : Resistance of TiNi film during thermal cycling (p.94)

Fig.5.10 : Start temperatures of $B2 \Leftrightarrow R$ transformation of TiNi alloy films crystallised by holding at 773 K for 3.6 ks, plotted against Ni content (p.96)

Fig.6.1 : Heat flow during heating of SMA thin film by electrical current (p.100)

Fig.6.2 (a) : Effect of endothermic phase change during sample heating (p.103)

Fig.6.2 (b) : Effect of exothermic phase change during sample cooling (p.103)

Fig.6.3 : Black-body radiation spectrum for ℓ from 1 - 20 μm (p.104)

Fig.6.4 (a) : Radiative heat transfer coefficient as a function of heating current for 3.9 cm^2 sample (p.106)

Fig.6.4 (b) : Radiative heat transfer coefficient as a function of heating current for 1.3 cm^2 sample (p.106)

Fig.6.5 : Endothermic phase change during sample heating (p.108)

Fig.6.6 (a) : Endothermic phase change during sample heating (p.110)

Fig.6.6 (b) : Exothermic phase change during sample cooling (p.110)

Fig. 6.7 : Thermal image by non contact at 11 sec for heating ((a) thermal image (b) temperature at lines) (p.112)

Fig. 6.8 : Thermal image by non contact at 12 sec for heating ((a) thermal image (b) temperature at lines) (p.113)

Fig. 6.9 : Thermal image by non contact at 13 sec for heating ((a) thermal image (b) temperature at lines) (p.114)

Fig. 6.10 : Relationship between average temperature and rate of change, with the time for heating (p.115)

Fig. 6.11 : Relationship between minimum temperature and rate of change, with the time for heating (p.115)

Fig. 6.12 : Relationship between maximum temperature and rate of change, with the time for heating (p.116)

Fig.7.1 : Relationship between device lateral dimension, heating power and

maximum heating rate (p.121)

Fig.7.2 : Relationship between film thickness and maximum cooling rate (p.122)

Fig.7.3 : Micromachining strategy (p.124)

Fig.7.4 : Schematic of FIB column (p.125)

Fig.7.5 : Geometrical setup for micro-parts blank (p.127)

Fig.7.6 : CAD schematic of gearwheel (p.129)

Fig.7.7 : FIB micromachined gearwheel (p.129)

Fig.7.8 : FIB trepanning (p.131)

Fig.7.9 : Control of the "pop-up" process (p.132)

Fig.7.10 : SEM of 3-D out-of plane structures (p.132)

List of tables

Table.1.1 : A comparison of SMA with piezoelectric, electrostatic, and bimetal actuators (p.23)

Table.3.1 : Measured current density from 3 cm Kaufman-type SIB source under various operating conditions (* with neutraliser) (p.53)

Table.3.2 : Relationship between beam diameter for 90 % and 80% uniformity and vertical distance below sources for Type 1 and type 2 grids (p.58)

Table. 4.1 : Sputtering yields of various materials in Ar⁺ ion (p.67)

Table.5.1 : Annealing temperatures and times using magnetron sputtering quoted by various authors (p.85)

Table.5.2 : Argon pressure, deposition rate and cathode power using magnetron sputtering by various authors, which compared with ion beam sputtering deposition (p.87)

Table.5.3 : Parameters used to fit the x-ray reflectometry data in Fig.5.7 (p.91)

Table.5.4 : Resistivity, composition and film thickness for TiNi shape memory alloy by various authors (p.93)

Table.5.5 : Transformation temperature and composition for TiNi shape memory alloy by various authors (p.95)

Acknowledgement

I would like to thank Ph.D. supervisor, Dr. Sam. T. Davies for his valuable guidance, support and friendship throughout the course of the studies, that lead to the submission of this thesis. Without Dr. Davies contribution, this thesis would not have been possible. I would also like to thank Dr. David Hayton for his friendship, hospitality and help in preparing this thesis. I would also like to Dr. M. G. Krishna for his valuable opinions in preparing this thesis.

I would also like to acknowledge the help and friendship for the many technicians in the School of Engineering at Warwick. Particular thanks go to Steve Wallace, David Robinson and Huw Edwards.

Thanks are also due to Professor Nobuo Yasunaga at Tokai University who introduced me to the University of Warwick to study microengineering. Finally, I must thank my family for their support and patience, especially in the preparation of this thesis.

Kazuyoshi Tsuchiya, April 1999.

Declaration

The work described in this thesis is my own, except where stated as otherwise. It was carried out in The School of Engineering, Warwick University between April 1995 and April 1999. No part of this work has been submitted previously to the University of Warwick, or any other academic institution for admission to a higher degree. Some of the work has already appeared in the form of publications, which are listed in the bibliography.

Kazuyoshi Tsuchiya

April 1999

Abstract

TiNi shape memory alloy has been recently investigated for use in microactuators because of the high power to volume ratio. Conventional sputtering methods, such as RF and DC sputtering and magnetron sputtering, have previously been used by other workers in order to deposit TiNi thin films. As-deposited films produced by these methods are amorphous, and are then crystallised typically by annealing at 500 °C for 1 hour in order to exhibit the shape memory effect. These deposition methods have invariably used alloyed targets to grow thin films. In this thesis, an Ion Beam Sputter Deposition (IBSD) method has been used by which argon ions are used to bombard non-alloyed targets. The thin films grown by this technique demonstrate the characteristics of the shape memory effect. Films have been characterised by electrical resistivity, resistance and thermal measurements, giving physical properties in excellent agreement with those quoted in the literature. Compositional and density measurements were done by X-ray reflectometry and were consistent with equi-atomic composition and nominal density for TiNi. In addition thermal modelling was used to investigate implications of heating and cooling rates for microactuator operation. Finally, a novel fabrication process is proposed, combining ion beam milling and Focused Ion Beam (FIB) trepanning for the process of microactuator production.

List of abbreviations

A_f : Austenite finish temperature

A_s : Austenite start temperature

CMOS : Complementary Metal-Oxide Silicon

DSC : Differential Scanning Carorimetry

FIB : Focused Ion Beam

GIXA : Grazing Incidence X-ray Analysis

IBSD : Ion Beam Sputter Deposition

LIGA : Lithographie Galvanoformung Abformung

MEMS : Micro Electro Mechanical Systems

MOEMS : Micro Optical Electro Mechanical Systems

M-phase : Monoclinic structure

M_f : Martensite finish temperature

M_s : Martensite start temperature

SIB : Showered Ion Beam

SIMS : Secondary Ion Mass Spectrometry

SMA : Shape Memory Alloy

SME : Shape Memory Effect

PSU : Power Supply Unit

R-phase : Rhombohedral phase

1 INTRODUCTION

1 Introduction

This thesis describes the production and properties of shape memory alloy thin films, for micro actuators in microelectromechanical systems (MEMS), fabricated by an ion beam sputter deposition method. This chapter outlines the project, and introduces MEMS and the shape memory effect, shape memory alloys, and applications of shape memory alloy. This chapter finishes with a section describing the motivation for conducting this work.

1.1 Background to this work

1.1.1 Micro Electro Mechanical Systems (MEMS)

The microactuators and MEMS have transformed the conventional field of sensors and actuators in general. MEMS can be usually described as follows :

1. mechanical microstructures,
2. microsensors, microactuators
3. electronics integrated on a silicon chip .

MEMS research and development has progressed rapidly since 1988, when the electrostatic micromotor the size of a human hair was demonstrated[1]. MEMS are not only about the miniaturisation of present mechanical systems but they

also create a new paradigm for the design of mechanical devices and systems. The telecommunication industries, for example, have taken specific advantage of miniaturisation of mechanical systems[2]. MEMS in general, are becoming increasingly important in modern technology. The miniaturisation of mechanical systems has led to progress and new opportunities in many areas of science and technology.

MEMS have allowed microactuators to perform physical functions. For instance, shape or volume changes are caused by phase transformations resulting in the shape memory effect. Researchers have fabricated microactuators used in micropumps and microvalves, which can be operated by the shape memory effect.

Fig.1.1 shows the design of a shape memory alloy (SMA) microvalve, which was published in 1999[3]. TiNi SMA microdevices were fabricated from a thin sheet of equi-atomic Ti-Ni, which was made by melting Ti and Ni in a high frequency induction furnace followed by final cold-rolling to reduce the thickness to 100 μm . The polymethylmethacrylate substrate was fabricated by laser cutting as mechanical micromachining to establish the pressure chamber. The TiNi sheets, which were heat-treated for 530 $^{\circ}\text{C}$ for 1.8 ks, have been preformed by laser cutting to consist of a circular array of double-beam bending elements.

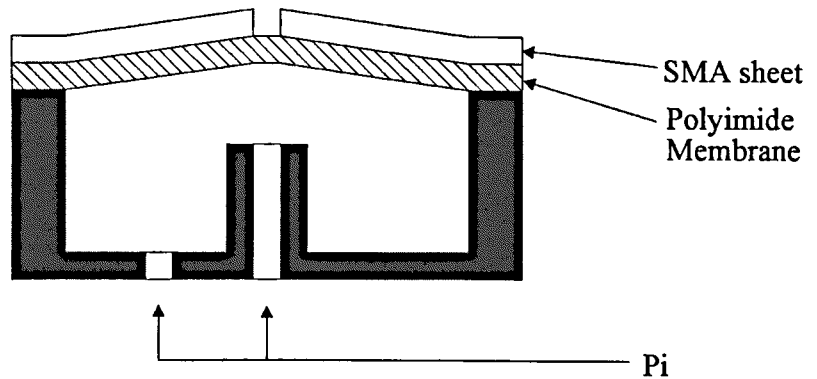


Fig.1.1 : Design of SMA microvalve and operation model.

P_i denotes inlet pressure[3]

Consequently, problems of fabrication, bonding and assembly for microactuators in MEMS research have also been of increasing importance.

1.1.2 Microfabrication strategies

Microfabrication is concerned not only with removing material physically by micromachining or micromilling. Microfabrication also involves deposition of materials such as in thermal processing, sputtering and chemical vapour deposition as shown in Fig.1.2.

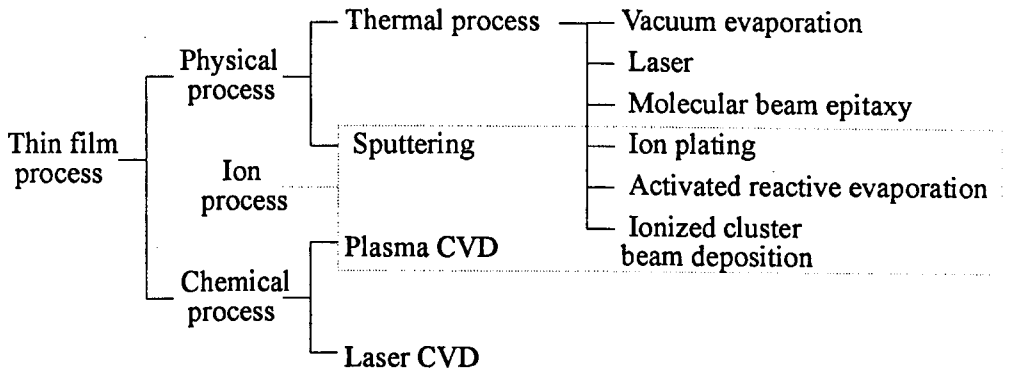


Fig.1.2 : Thin film deposition process[4]

Sputtering systems generally consist of RF and DC sputtering, magnetron sputtering and ion beam sputtering, which will be introduced in detail in Chapter 2. Thin films have been deposited by sputtering systems.

1.2 Shape memory alloys

Recently it has been widely published that SMAs have great potential for use as microactuators[5,6,7]. SMA materials have a number of desirable properties that make them strong candidates for microactuator applications. The properties of these materials in bulk form have been extensively investigated and reviewed in the literature[8]. More recently, attention has turned to the production and characterisation of these materials in thin film or wire form in order to exploit their potential as actuators in MEMS[9], in biomechanical systems[10] and in micromechatronics[11].

1.2.1 Shape memory effect

According to L.M.Schetky[12], in order for an alloy to exhibit the shape memory effect, it must have a crystal structure that can shift into the configuration known as martensite when it is subjected to a certain temperature or stress and then shift out of it.

If the recovery of shape is restrained, a proportional force or displacement will be available for doing work or gripping another object. An example is shown below in Fig.1.3, which shows the effect of temperature on shape memory alloys. If the rod is made from a shape memory alloy, and the rod is designed to deform above temperature A_p , a straight rod is heated to the "betatizing" temperature and then quenched. The rod now contains martensite phase. After the rod was deformed below the martensitic transformation temperature, the rod returns to the original shape when heated above the austenite transformation temperature.


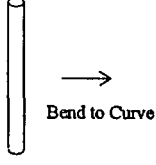

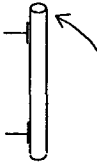


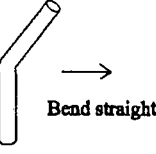

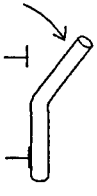
Initial Shape	Additional Cold or Hot Shaping	Shape after Betaizing and Quenching	Position at Room Temperature	"Remember" Position (above Af)
	None			
				

Fig.1.3 : Temperature effect for shape memory alloy by L.M.Schetky[12]

1.2.2 TiNi shape memory alloys

The shape recovers almost perfectly in more than ten alloys. However, because of performance and cost, only two - TiNi and Cu-Zn-Al - are used in practice. TiNi shape memory alloy thin film was first produced by Sekiguchi *et al*[13], using a vacuum deposition method. The shape memory effect was verified in 1983. Many workers have found TiNi to be especially suitable. This alloy resists corrosion and components made from it have a long lifetime. Industrial applications that require reliable switching mechanisms generally use TiNi. This alloy is also stable within the human body and TiNi has been used extensively in medical applications.

SMA actuators have several advantages over other methods of microactuation,

based on piezoelectric, electrostatic or bimetallic principles. These include high work output per unit volume, high power to mass ratio and the capability of being driven without high applied electric fields. Table.1.1 shows a comparison of TiNi shape memory alloy thin films with magnetic, electrostatic and piezoelectric actuators. The energy output per unit volume is very high compared with other actuators. The value is a factor of 10 larger than a DC magnet motor, when compared to TiNi shape memory alloy.

Principle	Maximum work energy density (J cm^{-3})	Drive conditions/ biocompatibility	Scalability (shrinkability)	Power/weight
DC magnet motor	0.9	B=1.5T Yes	Poor	Low
Micro-electrostatic	0.4	E=300V μm^{-1} No	Good	High
Piezoelectric(PVDF)	$4.8 \cdot 10^{-4}$	E=30V μm^{-1} No	Good	High
Shape memory alloy (TiNi)	10.4	P=1.4W mm^{-3} Yes	Good	High

Table.1.1 : A comparison of SMA with piezoelectric, electrostatic, and bimetal actuators[14]

Other desirable features such as biocompatibility and scalability to small dimensions can also be exploited. SMA materials can provide extremely large forces, movements intermediate between those of piezo devices and electrostatic microactuators, or a combination of both force and displacement if mechanically biased by a suitable spring. However, in common with all thermal actuator devices, the efficiency of SMA actuators will be relatively low ($\sim 5\%$) as the material must be heated above an austenite transformation temperature to recover the original, undeformed, martensitic state shape.

Moreover, the speed of response will be relatively slow due to the need to cool the material to revert to the deformed martensite structure.

1.2.3 Application of shape memory alloys

Shape memory alloys have been exploited in mechanical applications, which need a precise mechanical response to small repeated temperature changes. A micro valve produced by TiNi shape memory alloy, is shown in Fig.1.4 below as a typical example.

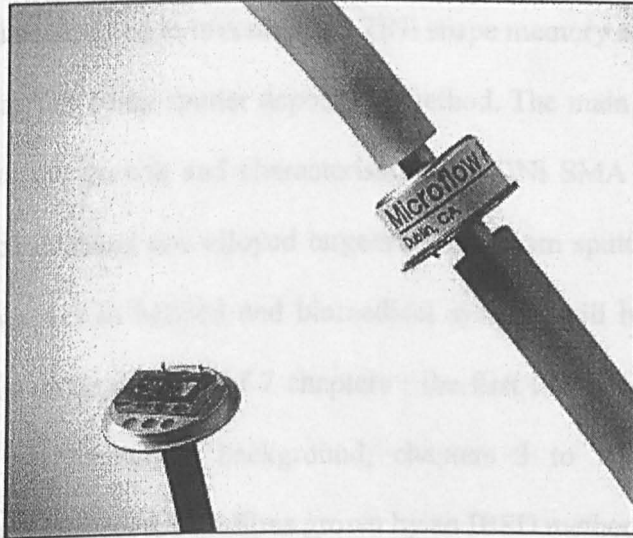


Fig.1.4 : Silicon micromachined proportional valve by MicroFlow,Inc[15]

This shape memory alloy actuated silicon microvalve is designed to provide either proportional flow or pressure control of gasses, using the shape memory properties of sputtered TiNi films. Microvalves can be produced as individual devices or as entire valve arrays on a silicon manifold by using standard integrated manufacturing processes, such as ion beam deposition,

photolithographic patterning, and chemical etching. The strips are deformed in tension as the valve normally closes through the force of an integral bias spring due to the one way shape memory effect. When the alloy is heated by passing a small current through it, the material recovers its original shape above an austenite transformation temperature. When the force lifts the silicon poppet off the valve seat, gas can flow.

1.3 Motivation and purpose of this work

This thesis will be devoted to investigating TiNi shape memory alloy thin films fabrication by an ion beam sputter deposition method. The main achievements of the work are the growth and characterisation of TiNi SMA thin films on unheated substrates using non-alloyed targets by ion beam sputter deposition. Potential applications in MEMS and biomedical systems will be emphasised throughout. This thesis consists of 7 chapters : the first two chapters describe the historical and theoretical background, chapters 3 to 7 then describe experimental data relating to thin films grown by an IBSD method.

Chapter 2 will describe the historical background of ion beam sputtering, showered ion beam equipment, and factors such as sputtering yield and angle of incidence effects for sputtering phenomena. Comparison with DC and RF sputtering, generally used for deposition of thin films in industry, will be described in the last section of this chapter. Ion beam sputter deposition allows thin film growth to occur in a clean environment of a high vacuum system. Due

to containment of the plasma in the discharge chamber, ions can reach the target without colliding with residual gas atoms.

In chapter 3, the SIB source, which was used in this work, will be characterised in respect of current density and beam profile properties. Current density was investigated in both manual and automatic modes of operation at various distances from the ion source, and effects of variations in accelerator grid voltage quantified. Beam profile measurements were made using various grid types, and effects of grid type on current density evaluated. The specific grid type required to optimise operating conditions for thin film deposition, was determined from the data presented in this chapter.

Chapter 4 follows on from chapter 3 by relating deposition rates to sputtering yields from targets of Al, Ti and Ni. Relationships between film thicknesses and beam voltage and current will be established. For Ti and Ni, deposition rates were investigated separately. In this deposition set-up (with 2 cm separation from target to substrate), the deposition rates of Ti and Ni were identical within the experimental error. Targets consisting of eight 45 ° sectors, alternating between Ti and Ni, were consequently prepared for thin film deposition.

TiNi thin films were deposited on unheated substrates at typical deposition rates of $\sim 0.5 \mu\text{m/h}$. In chapter 5 the TiNi thin films were characterised by electrical resistivity and resistance measurements and compared with values

quoted in the literature. The resistivity of the TiNi SMA thin films was $1 \mu\Omega.m$. Phase transformation temperatures, namely A_s , A_p , M_s and R-phase, are $60^\circ C$, $85^\circ C$, $50^\circ C$ and $62^\circ C$, respectively. Good agreement was found with values quoted for equi-atomic TiNi in the literature. The compositions of TiNi thin films were also consistent with equi-atomic TiNi, which was shown by X-ray reflectometry.

In chapter 6, the TiNi shape memory thin films were characterised by measurements of temperature – time profiles in order to evaluate thermal parameters influencing microactuator operation and behaviour and to measure phase changes indicative of the shape memory effect. Here an alternative strategy to that of differential scanning calorimetry (DSC) is adopted by maintaining constant heating power and measuring the rate of change of temperature corresponding to the specific heat capacity change. Non -contact measurement was made, by infrared focal plane array camera thermal imaging. Thermal imaging could readily identify the phase transitions characterising the shape memory effect.

Chapter 7 begins by describing the effects of dimensional scaling of TiNi shape memory alloy structures for microactuator devices. Speed of response for such shape memory alloy structures will then be calculated. Production of micro-parts by focused ion beam (FIB) trepanning techniques is then introduced and implications for SMA microdevices explored. This chapter ends with some suggestions for future work and the overall conclusions of the thesis.

**2 APPARATUS AND PRINCIPLES OF ION BEAM DEPOSITION
TECHNIQUES**

2 Apparatus and principles of ion beam deposition techniques

2.1 Showered ion beams and the Kaufman ion source

Fig 2.1 shows a schematic diagram of the showered ion beam sputter apparatus. This consisted of a Kaufman type ion source (Fig. 2.2 (a)) contained within a discharge chamber (Fig 2.2(b)) evacuated by the vacuum system illustrated in Fig. 2.2 (c). The ion source contains a refractory metal cathode made from tungsten wire, behind a set of grids to focus the ion beam. The diameter of these grids was three centimetres. The source could produce beam currents ranging from a few milli-amperes to several amperes.

Fig. 2.2 (c) shows the diffusion pump. This was backed by a rotary pump which reduced the pressure to 2×10^{-2} Torr (2.7 Pa) in about 5 minutes. The diffusion pump then lowered the pressure to 8×10^{-5} Torr (0.01 Pa) in a further 10 minutes. The working gas (usually argon) was then introduced into the discharge chamber and the ion source was operated at pressures of typically 5×10^{-4} Torr (0.07 Pa). Penning and Pirani gauges were used to monitor the conditions inside the apparatus. The ion beam energy ranged from 500 to 2000 eV. This energy, the working pressure and the beam flux were all easily controlled and quantified by a computer (shown in Fig. 2.2 (b)). With reference to Fig.2.1 (b), energetic electrons from the cathode struck the argon atoms within the ion source. These ions were formed into small beamlets when they

passed through the holes in the screen grid. The ions in these beamlets were attracted to the negative acceleration grid. They passed through this negative grid without striking it, due to the alignment of the holes in the two grids, and they were directed toward the target. Beam divergence was prevented by "neutralising" the positively charged argon ion beam with electrons from the neutraliser filament. The number density of these electrons was equal to the number density of the Ar^+ ions. Energetic electrons were constrained by the magnetic field whilst low energy background electrons could reach the anode.

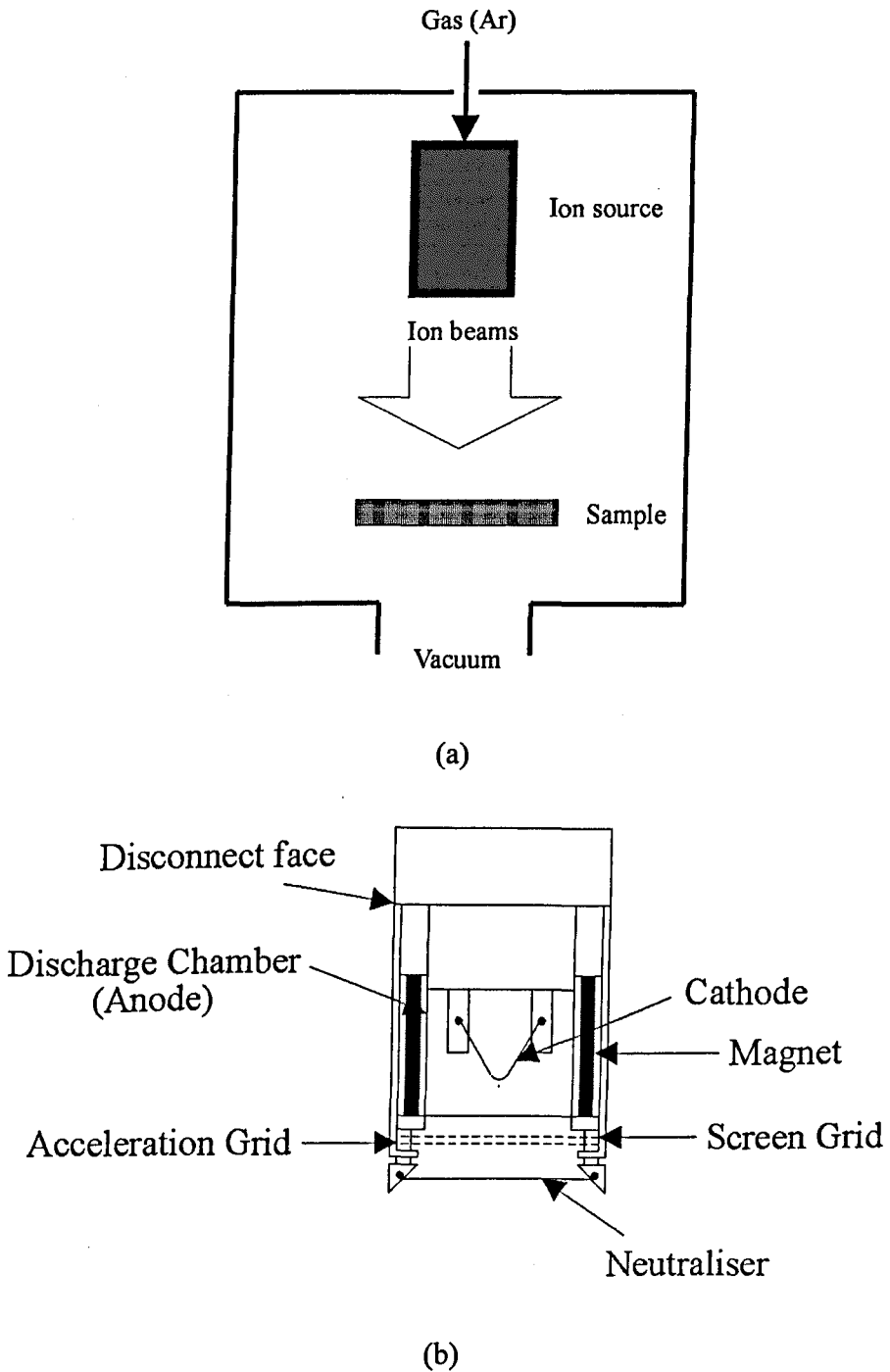
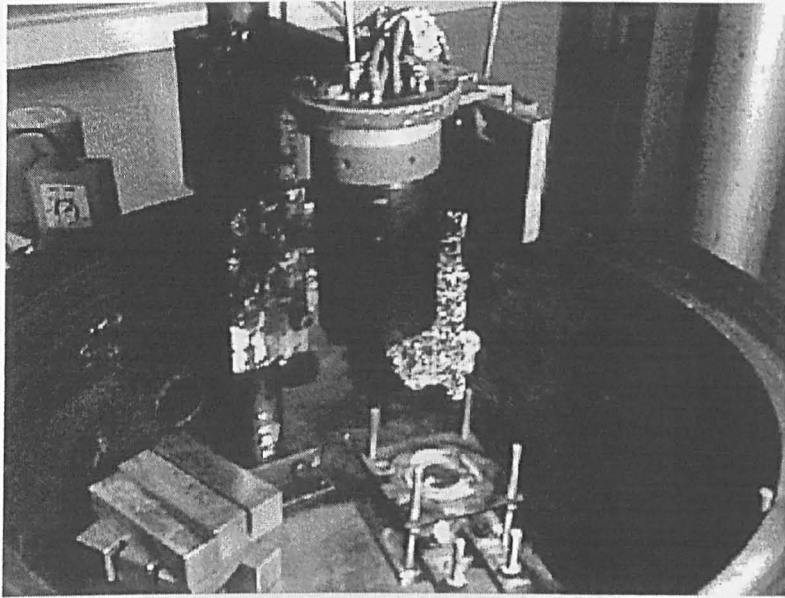
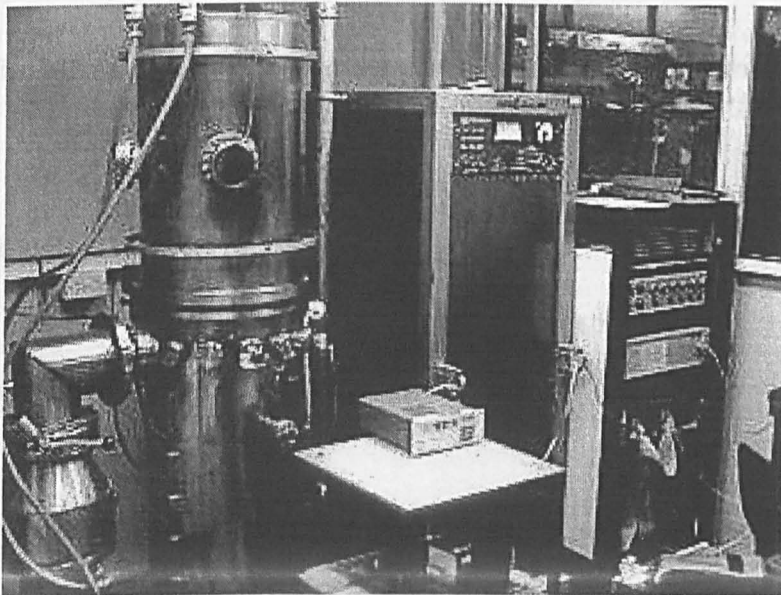


Fig.2.1 Schematic diagram of showered ion beam equipment
(a) showered ion beam system, (b) showered ion beam source



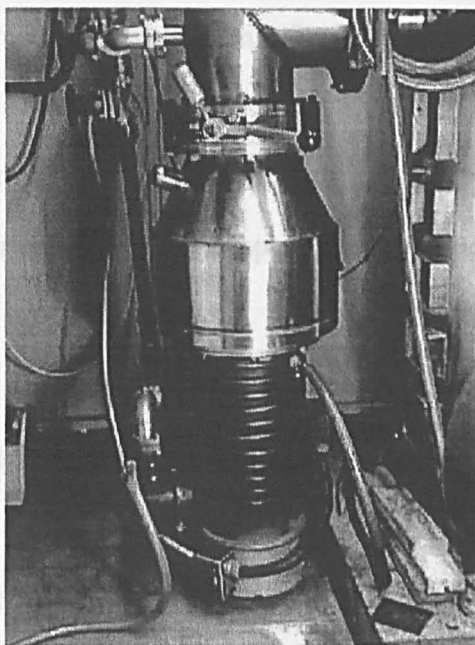
(a)



(b)

Fig. 2.2 : Showered ion beam apparatus (University of Warwick)

(a) Kaufman type ion source, (b) Showered ion beam unit



(c)

Fig. 2.2 : Showered ion beam apparatus (University of Warwick)

(c) Diffusion pump

2.2 Principles of ion beam sputtering

2.2.1 General overview of ion beam sputtering

Grove first observed the phenomenon of sputtering in a DC gas charge tube in 1852[16]. He found that the cathode surface within the discharge tube was sputtered by energetic ions in the gas discharge, and that cathode materials were deposited on the inner wall of the tube.

Five years after Grove's work, vacuum evaporation methods were developed. These techniques were popularised by Faraday and, until the 1960s, they

remained the main methods by which thin films were fabricated[17].

The first descriptions of sputtering on the atomic scale were made early in this century. These workers observed evaporation from hot objects such as a cathode filaments. In the past three decades, sputtering techniques have developed rapidly. In addition, the theory of collision cascade has been developed, which can treat problems both analytically and numerically[18,19].

By 1960, the configured broad beam ion source had been developed from work on electric propulsion in the US space program. These experiments had led to the Kaufman ion source, which contains a hot filament cathode and neutraliser. Alternatively, the electron emission from either the cathode or neutraliser can be supplied from a hollow cathode[20] with a separate gas flow. The working gases used for hollow cathodes in industrial applications have been either argon or xenon.

In the early 1970's, early applications for industrial uses were published in the USA. Several papers emphasised the simple removal of material (etching) and deposition using an ion beam[21]. In the 1980's, ion beam processing became concerned with etching and deposition using reactive ion beams. Reactive gases such as nitrogen and oxygen were frequently used. In another particularly interesting application[22], a composite beam of 1200 eV hydrogen and argon ions bombarded a graphite target. Films of diamond-like carbon were thus deposited on silicon substrates, produced by ion beam sputter deposition. These

films could be used for making novel electronic devices. Sputtering methods are now becoming the norm for a wide range of applications where thin films are required.

At the present time, sputtering has found broad usage not only in surface analytical techniques, where it can be used as a tool for depth profiling[23], but also in the fabrication of thin films and semiconductors.

2.2.2 Mechanism of sputtering

In early 1900's, two theoretical models were proposed to explain the sputtering process. The thermal vaporisation theory, where the target surface is heated enough to be vaporised due to the bombardment of energetic ions, was proposed by Hippel and Blechschmidt[24] in 1926. They based their work on experimental observations of the Kundsén cosine emission distribution (see Fig.2.3). The alternative momentum transfer theory, where the momentum of the incident particles are transferred to and release the target surface atoms, was first proposed by Stark in 1908 and Compton in 1934. Detailed studies by Wehner in 1956[25], including the observation of spot patterns in single crystal sputtering, suggested that the most important mechanism is the momentum transfer process. At present sputtering is believed to be caused by a collision cascade in the surface layers of a solid.

The mechanism of the sputtering process is shown in Fig.2.4. Electrically accelerated ions such as Ar^+ , with kinetic energies between tens of eV and 10

keV, are uni-directionally orientated and projected onto the workpiece surface under high vacuum (1.3×10^{-4} Pa). Furthermore, as shown in Fig.2.4, when sputtered atoms have kinetic energies several tens of electron volts more than those of ordinary evaporated atoms, atoms on the surface can be knocked out from the target.

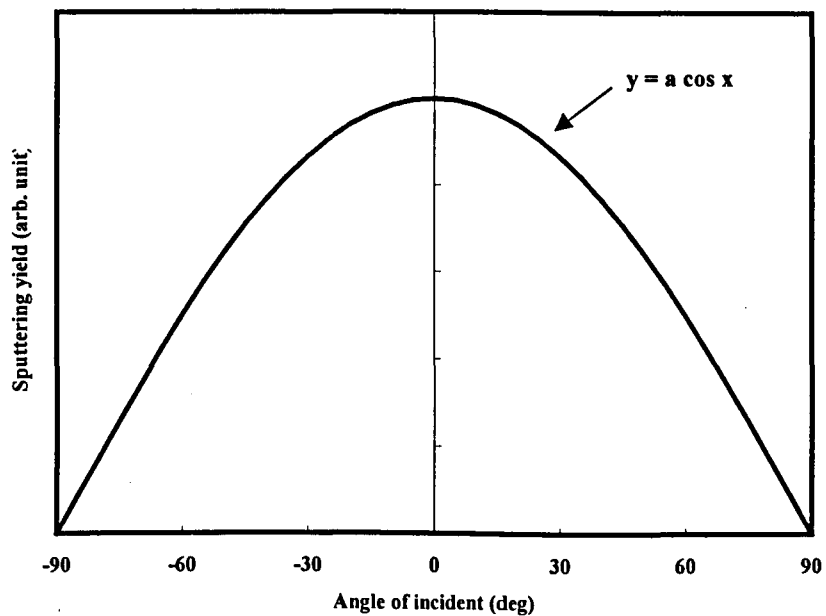


Fig. 2.3 : Angle of incidence and sputtering yield

Ar^+ ions collide with the nuclei of atoms of the workpiece and knock out or sputter, the surface atoms. This processing is therefore called ion sputter etching or ion sputter machining. The penetration depth of an impinging 10 keV argon ion is estimated to be several nanometers, or about ten atomic layers. Ions with higher energies, e.g. 100 keV, can penetrate further through the atomic lattice and become interstitial or substitutional atoms in the surface layer. This kind of deep penetration process is widely used for ion implantation,

in which impurities of atomic size are injected in semiconductor wafer processing.

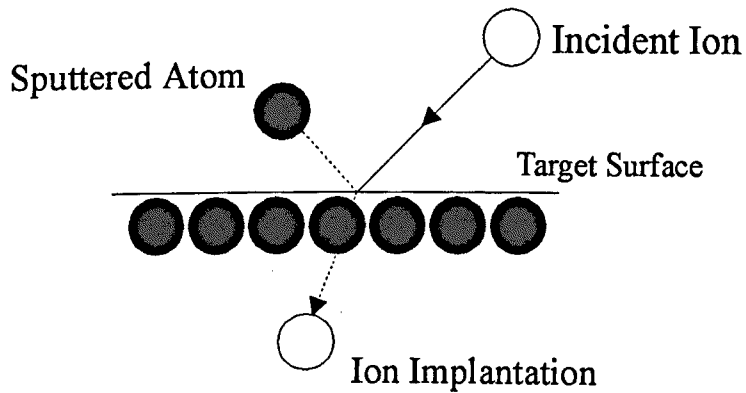


Fig. 2.4 : Mechanism of sputter machining

2.3 Sputtering phenomena

Sputtering is described as the removal of atoms from a solid target surface due to energetic particle bombardment. For quantitative sputtering, the sputtering yield, ion energy and angle of incidence effects all need to be measured.

2.3.1 Sputtering yield

The sputtering yield (S) is the most important quantitative value for sputtering. This is defined as the mean number of atoms that are removed from the surface of a solid target by each incident ion. It is given by

$$S = \frac{\text{Atoms removed}}{\text{Incident ions}}$$

The sputtering yield depends upon both the incident ion and the target surface. It is influenced by the energy and incident angle of the particles, and also by the crystal structure and orientation of the target.

Several methods exist to measure the sputtering yield. Usually the total sputtering yield is determined by monitoring the decrease in the mass, or the thickness of the target. This is often measured by weight loss experiments using a quartz crystal oscillator micro-balance (QCOM)[26]. This QCOM technique is highly sensitive and can be operated under vacuum.

2.3.2 Ion energy

The ion energy is defined by the difference in electric potential between two parallel electrodes in the ion source. Moreover, that energy is the amount of energy which accelerates the ions causing them to impinge on a target in processing.

Typical sputtering yields from low energy ions were measured by Stuart and Wehner[27]. In this low energy region (tens of eV), a threshold energy exists for sputtering. The threshold energy was first observed by Hull (1923)[28]. He found that the thorium-tungsten (Th-W) thermionic cathode in gas rectifier tubes was damaged by bombardment with ions when the bombarding ion energy exceeded a critical value, in the order of 20 - 30 eV[29]. At higher ion

energies of 10 - 100 keV, the incident ions embed themselves below the surface. The sputtering yields are not then governed by scattering from the surface, but by scattering within the target. Above 10 keV, the sputter yields decrease due to energy dissipation of the incident ions deep in the target. This is called channelling. Sputtering yields reach maximum values in the ion energy region around 10 keV[30].

2.3.3 Angle of incidence effects

In 1942, Fetz studied the variation of the sputter yields with the angle of the incident ions. Wehner then considered this topic in detail[31,32]. Metals such as gold (Au), silver (Ag), copper (Cu) and platinum (Pt) which have high sputtering yields show a very slight angle effect. However, iron (Fe), tantalum (Ta) and molybdenum (Mo) having low sputtering yields show a very pronounced angle effect. The yield increases with the incident angle and reaches a maximum at angles between 60 ° and 80 °. It then decreases rapidly for larger angles. An angular distribution has also been reported by T. Hoffmann *et al*[33].

Typical angular distributions are shown in Fig.2.5. At lower energies much more material was ejected at large angles to the surface normal than in the direction normal to the target surface. The angular distributions of sputtered atoms, released by incident ions normal to the surface, were investigated by Seeliger and Sommermeyer[34]. Their ion beam was in the high energy region around 10 keV. Their experiments suggested that the angular distribution was

described by Knudsen's cosine law, which supported the thermal evaporation model. However, Wehner and Rosenberg[35] measured the angular distribution of sputtered atoms released by lower energy (100 eV to 1000 eV) Hg^+ (mercury) ions in a low pressure environment as shown Fig.2.5. At higher ion energies, the distribution approached a cosine distribution. Molybdenum (Mo) and iron (Fe) shown a greater tendency to eject to the sides than nickel (Ni) or platinum (Pt). At energies above 10 keV the distribution became greater than cosine function.

The angular distribution is affected principally by the sputtering mechanism and it is important in several applications including secondary ion mass spectrometry (SIMS), sputter deposition, and sputter etching. Angular distributions are studied in detail by using ion beam sputtering systems[36].

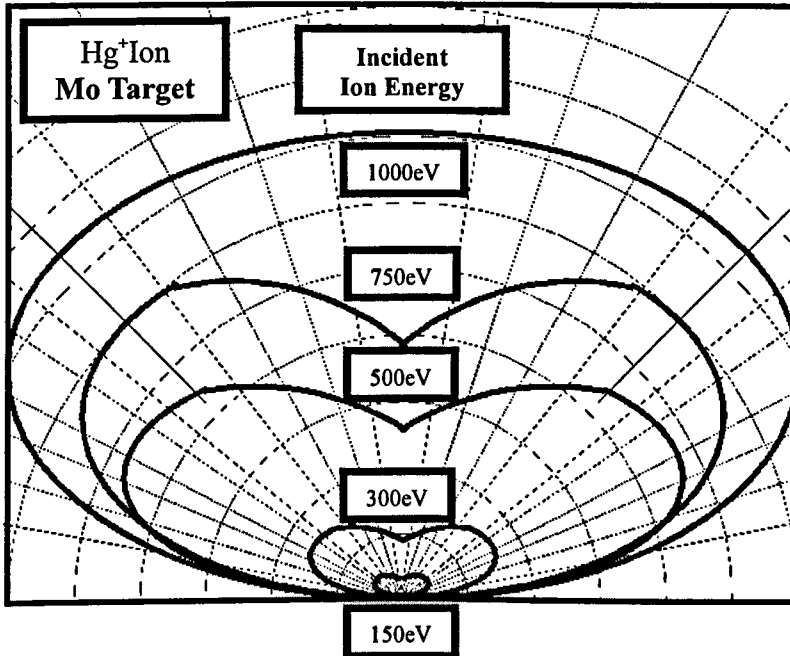


Fig. 2.5 Angular distributions of sputtered particles from polycrystalline targets[35]

2.4 Principle of ion beam deposition

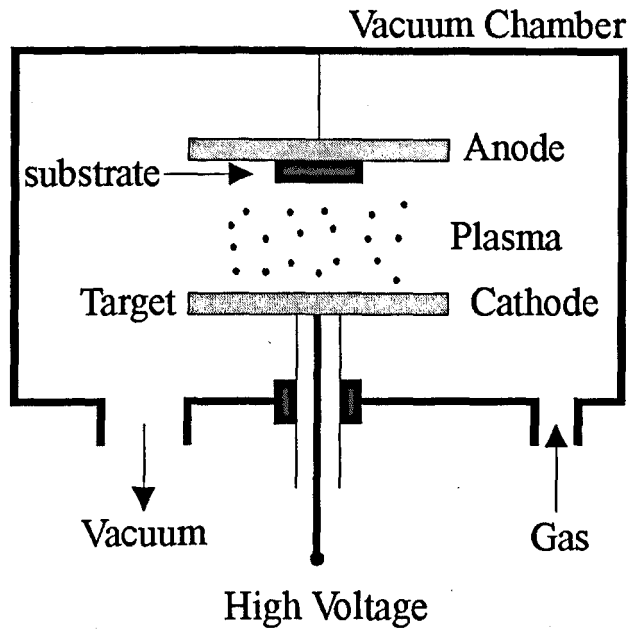
As described above, sputtering is the phenomenon where atoms are ejected from the target by a beam of irradiating ions. These sputtered ions are then deposited onto a nearby substrate. Three techniques have been developed : RF and DC sputtering, Magnetron sputtering, and ion beam sputtering.

2.4.1 RF and DC sputter deposition

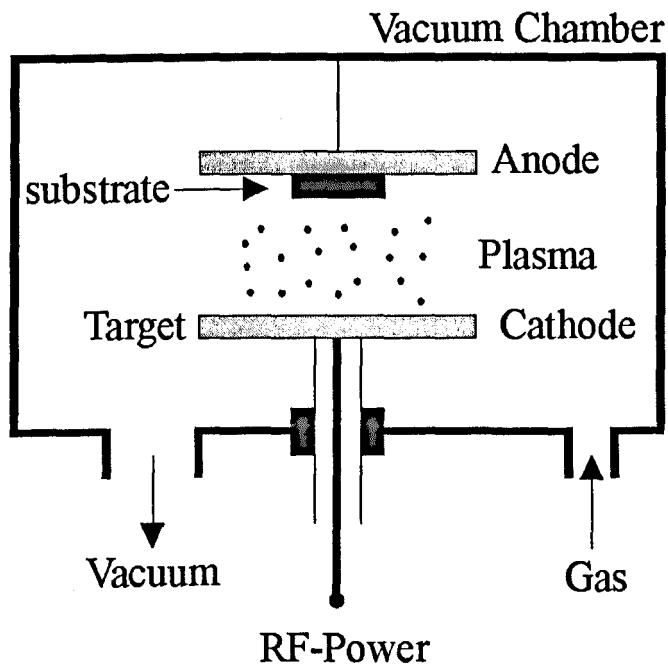
In 1933, Robertson and Clapp[37] observed that the glass surface of a RF discharge tube was sputtered during discharge. Maissel and Davidse later identified the thin film deposition technique of insulating targets by RF sputtering[38,39].

RF and DC sputtering are plasma-based sputter vapour deposition techniques. The electrodes in these systems consist of a cold cathode and anode. The front surface of the cathode is covered by the target material which will be deposited, and the substrate is located over the anode. Generally, the chamber is filled with argon gas to a pressure of 0.1 Torr (13.3 Pa). In the DC sputtering system as shown in Fig.2.6 (a), the argon ions, which were produced by glow discharge, are accelerated to the cathode, and the target is sputtered, and a thin film is consequentially deposited onto the substrate. In DC sputtering systems, sputtering of insulating targets is impossible, because the surface of the target becomes charged positively. However, it is possible to maintain the glow discharge for an insulating target, when the target is supplied with a voltage at radio frequency (RF). This is the RF sputtering system as shown in Fig.2.6 (b).

In modern industries, the RF sputtering system is an important technique in the deposition of thin films. Applications of thin films are widespread, and this technique has successfully brought about the development of new materials. Unfortunately, however, the deposition speed of thin films by this method is rather slow. It cannot be quantitatively compared because of equipment dependence. The deposition rates of thin films by RF sputtering methods are typically an order of magnitude less than comparable vacuum deposition techniques. This disparity led to the widespread use of the latter technique. At this point it was a large problem to utilize sputtering on an industrial scale.



(a)



(b)

Fig. 2.6 : DC and RF sputtering systems, (a) DC sputtering, (b) RF sputtering

2.4.2 Magnetron sputter deposition

Penning[40] (1935) first studied low pressure sputtering in a system where a transverse magnetic field was superimposed on a DC glow discharge. This low pressure sputtering was a promising technique for the production of thin film devices. A wide variety of thin films can be made with little film contamination and a high deposition rate.

At the beginning of the 1960's, Gill and Kay proposed an inverted magnetron sputtering system[41]. The pressure of the sputtering gas was demonstrated to be as low as 10^{-5} Torr (1.3 mPa), two orders of magnitude below conventional sputtering systems. From the 1970's, magnetron sputtering was also widely utilised for various thin films coating processes in functional materials for silicon integrated circuits[42]. The magnetron sputtering method was then further developed by three groups such as Kirov *et al*[43], Hosokawa *et al*[44] and Thornton *et al*[45]. They solved the problem of slow deposition speed and they improved the technique. They recognised that the sputtering method was the most suitable method for the fabrication of thin films.

Two types of magnetron sputtering systems for thin film deposition, are widely used, the cylindrical type and the planar type. Since a permanent magnet is embedded in the cathode target, the magnetic field can be several hundred Gauss.

Thornton[46] defined magnetron sputtering as a system where the region around the cathode is filled with electrons; these electrons being constrained by an electric field and a magnetic field. As a result, many ions are made in the vicinity of the cathode. These ions then collide with the cathode and sputter material from it.

Usually, some of the ions that are produced beyond the magnetic field collide with a wall of the chamber. This reduces the efficiency of the sputtering process. If the gas pressure is low, more of the electrons reach the anode without colliding with gas particles. Fewer ions are therefore produced. In order to raise the efficiency of the ionisation, when the gas pressure is high, the sputtered atoms collide with gas molecules in the chamber. Then sputtered atoms would not reach the substrate and the efficiency of the process would decrease. However, the magnetic field mitigates this effect. High efficiency is achieved by constraining the primary electrons to paths close to the cathode surface with applied magnetic fields. Ionisation efficiency is improved and higher sputtering rates results[47].

Magnetron sputtering equipment (as shown in Fig.2.7) generally comprises a flat target and substrate. The magnetron sputtering apparatus is similar to the equipment used for RF and DC sputtering. However, a permanent magnet is situated behind the cathode so that approximately parallel magnetic field lines are produced. Generally, the temperature rise of the substrate on which thin

films are deposited is similar to that found in RF and DC sputtering. The lowest temperatures found for magnetron sputtering has been about 80 °C. The temperature rise is mainly due to the impact of secondary electrons. Generally, the magnetron system can operate at a pressure of a few millitorr with plasma densities of 10^{11} ions cm^{-3} . The electromagnetic wave, which is right-hand circularly polarised wave relative to the magnetic field direction, can transfer energy to electrons. Electrons describe curved paths in the electric and magnetic fields.

Magnetron sputtering is a powerful technique for optical thin film coatings over large areas. Examples include the coating of architectural glass, or roll coating of temperature sensitive material. High-quality optical layers of most materials can be deposited by this method[48]. Magnetron sputtering can be done at high vacuum. A clean environment is essential where semiconductor devices are fabricated.

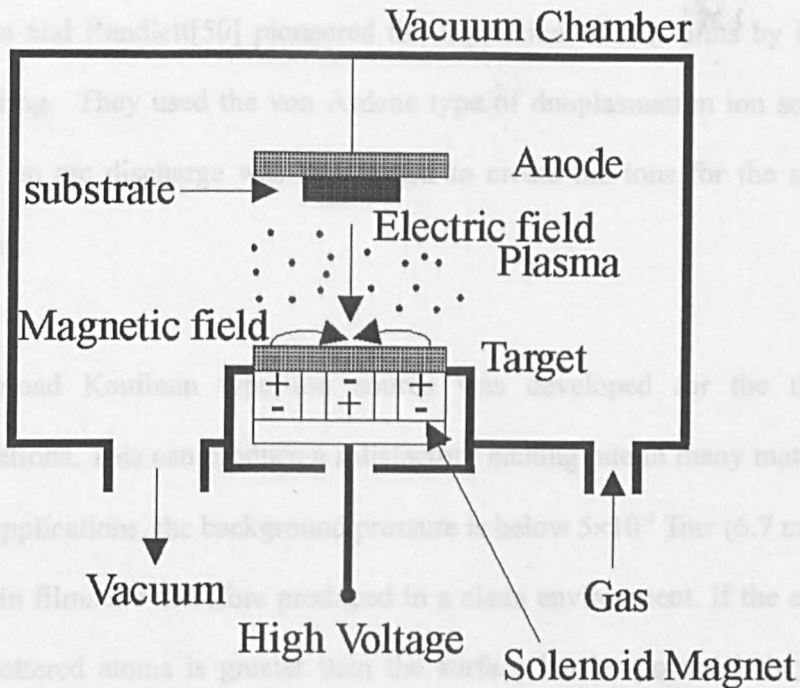


Fig. 2.7 : Planar magnetron sputtering system[49]

2.4.3 Ion beam sputter deposition

All the previous methods relied on vapour deposition from the gas phase. This led to problems such as scattering of the sputtering atoms and contamination of the film by gas molecules. To prevent this, IBSD techniques were developed. Ions were produced in an ion source and accelerated onto a target.

It is possible to evacuate the region around the target and substrate to below 10^{-4} Torr (0.01 Pa) if the vacuum pump has a large displacement. Few sputtering atoms are then scattered by residual gas and there is little contamination of the thin film by gas molecules.

Chopra and Randlett[50] pioneered the deposition of thin films by ion beam sputtering. They used the von Ardenne type of duoplasmatron ion sources, in which an arc discharge was maintained to create the ions for the sputtering process.

The broad Kaufman type ion source was developed for the thin film applications. This can produce a satisfactory etching rate in many materials. In most applications, the background pressure is below 5×10^{-5} Torr (6.7 mPa) [51], and thin films are therefore produced in a clean environment. If the energy of the sputtered atoms is greater than the surface barrier potential they collide with a target located opposite and adhere more firmly than in the usual vapour deposition. It is possible to simply adjust the alloy composition by adding material to the target or removing it. The ion beam technique also features independent control of incident ion energy and flux.

2.5 Summary

In this chapter, three types of techniques namely RF and DC sputtering, magnetron sputtering and ion beam sputtering are compared. Reference has been made to key factors, including the sputtering yield, ion energy and the incident angle of the ion beam. The next chapter describes how the Kaufman source was characterised, and optimised for fabrication of thin films by IBSD.

3 SIB SOURCE CHARACTERISATION

3 SIB source characterisation

3.1 Introduction

Ion beam sputtering techniques need to deposit atoms homogeneously to grow thin films of uniform depth. It is important that the grain size is uniform throughout the area and thickness of the film. Difficulties are caused by, for example, residual gas or beam current instability. The SIB source operated at a pressure of 0.05 Pa in this experiment. The beam profile and current density were carefully examined. Both these characteristics are critical in the deposition of thin films.

The investigation considered the effects of various SIB operational parameters, as well as the geometry of the extraction grids, on the current density. Careful note was also made of the beam profiles, and how they varied with the total extraction current.

Current measurement was made using a cylindrical detector aligned as a Faraday cup. Fig. 3.1 indicates how the X-Z movement of the Faraday cup allowed measurements to be made at various distances from the source.

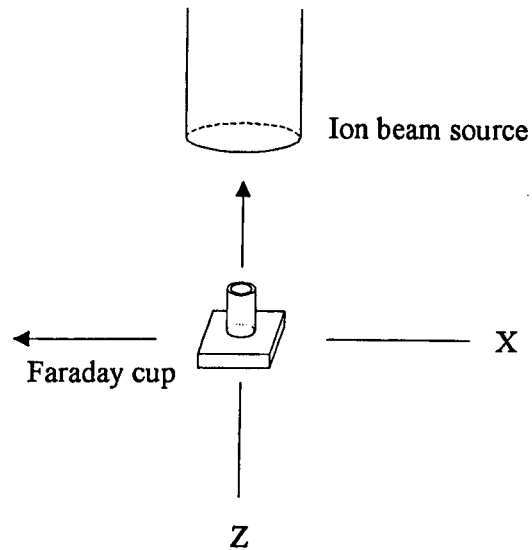


Fig. 3.1 : Movable directions of Faraday cup

3.2 Current density

A Faraday cup of aperture 1.0 cm was mounted on a linear translator vertically beneath the ion source, and on its axis of symmetry. Measurements of the current density were made by varying the following :

1. beam voltages in the range 500 - 1500 V,
2. beam current from 5 - 25 mA,
3. accelerator grid voltages of 100, 300 and 500 V,
4. and extractor grid to Faraday cup separation (z) of 5 - 20 cm.

3.2.1 Current density as a function of distance from the ion source

The source was operated in both automatic mode (ion source parameters preset for Ar⁺ by the manufacturer) and manual mode (where the ion source parameters were independently controllable). The measurements indicated in Table.3.1 were produced as follows :

1. auto mode (accelerators grid 300 V);
2. auto mode with neutraliser (accelerators grid 300 V);
3. manual mode (accelerators grid 100 V);
4. manual mode (accelerators grid 300 V);
5. manual mode (accelerators grid 500 V).

As expected, the measured beam current drifted with time. This was attributed mainly to filament aging. The drift was as much as 0.5 % min⁻¹ when uncompensated. The source conditions were constant. However, it could be easily corrected for by adjusting the filament current. This resulted in a negligible variation over a processing run.

A typical set of data, taken for 20 mA beam of 1000 eV ions, is given in Table.3.1. For given operating conditions, an increase of around 50 % in current density was obtained with beam neutralisation on as compared with beam neutralisation off, at a given source-sample separation.

Mode	Current Density (mA/cm ²)				
	Auto		Manual		
Z (cm)	300 eV	300 eV*	100 eV	300 eV	500 eV
5.0	1.77	1.92	2.89	1.88	1.50
7.5	0.82	1.19	1.78	1.01	0.74
10.0	0.55	0.74	1.21	0.61	0.45
12.5	0.30	0.44	0.70	0.38	0.29
15.0	0.20	0.29	0.39	0.25	0.20
17.5	0.12	0.21	0.31	0.20	0.16
20.0	0.12	0.16	0.25	0.17	0.15

Table.3.1 : Measured current density from 3 cm Kaufman-type SIB source under various operating conditions (* with neutraliser)

3.2.2 Effect of accelerator voltage on current density

Fig.3.2 shows the variation of current density as a function of accelerator voltage for various source-to-detector separations between 5 and 20 cm. The beam voltage and current were 1000 V and 20 mA respectively, and the source was controlled manually. The current density was affected by the accelerator voltage ; variations in the region 0.1 % - 0.5 % per volt were noted. However, the use of a stabilised PSU ensured that any drift was negligible.

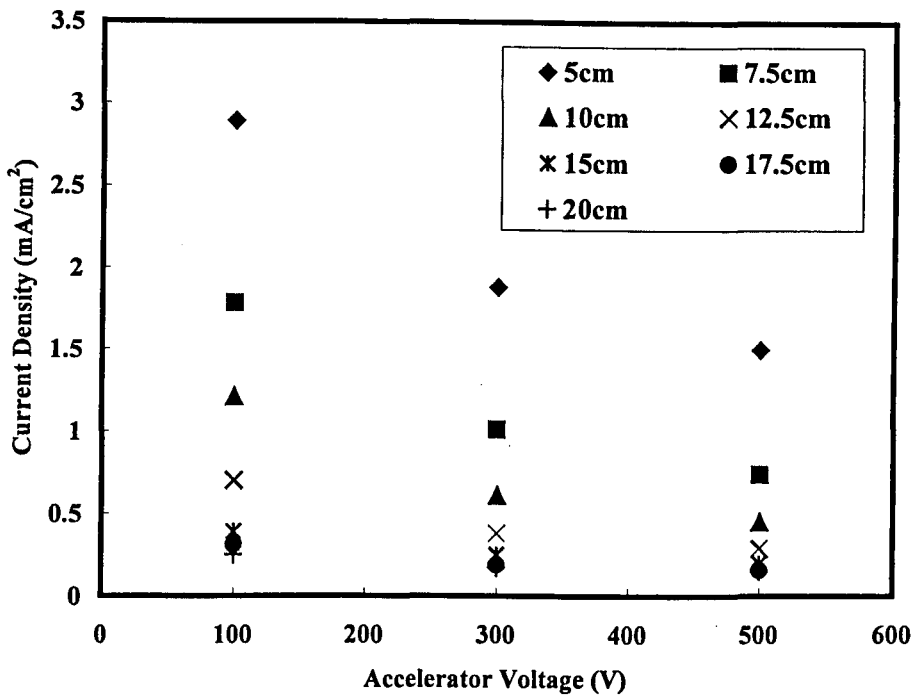


Fig. 3.2: Relationship between the current density and accelerator voltage at various distances below ion source with 1000 eV, 20 mA Ar^+ ions (manual mode control)

Fig.3.3 shows the relationship between the current density and total current of a 1000 eV, Ar^+ ion beam, at various distances below the ion source. The source was in automatic mode with the accelerator grid at a potential of 300 eV. The current density decreases with distance from the source. Clearly, it increases with the beam current, although this increase is not linear.

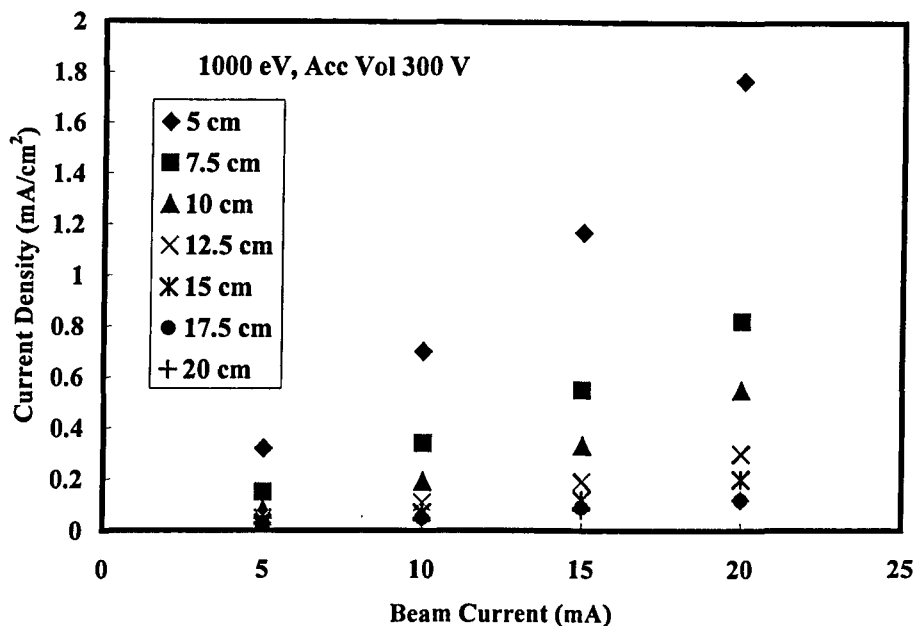


Fig. 3.3 : Relationship between the current density and total current of a beam of 1000 eV Ar⁺ ions at various distances below the ion source, (automatic mode accelerator grid potential of 300 V)

3.3 Beam profile

3.3.1 Beam profile variations with various grid types

One dimensional profiles of the SIB beam were made when a 5 mm diameter Faraday cup was moved perpendicular to the beam direction. The source was operated under identical conditions to those used for sample production. Three different types of extraction grid were used :

Type 1 grid : "uniform coverage"

Type 2 grid : "focused"

Type 3 grid : "collimated"

and the effect of extraction optics on both the ion current density and the beam profile was investigated. Typical beam profile data are shown in Fig.3.4 for total extraction currents in the range 10 - 25 mA at a source-sample separation of 5 cm when a type 3 grid is installed. The data from Fig.3.4 indicate that the axis of symmetry of the beam can shift when the extracted current is changed and that it need not necessarily remain precisely aligned with the geometrical axis of the source. For thin film deposition, it is important to align the geometrical axis of the source precisely for maximum current density on the target. Clearly the area of approximately uniform beam density decreases significantly when the current density is itself increased. The beam spreads decrease with increase of beam current as shown in Fig.3.5. Table.3.2 gives the measured beam diameter for 90 % and 80 % uniformity at typical distances below the source for Type 1 and Type 2 grids. Source operating conditions were 1000 V and 20 mA total current in both cases.

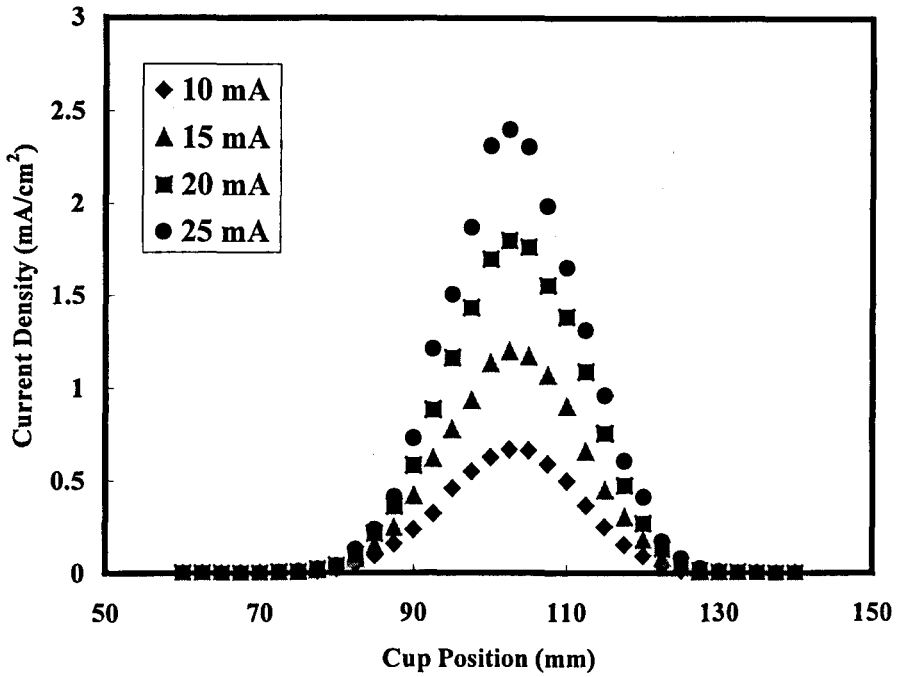


Fig.3.4 : Beam profile of 3 cm SIB source

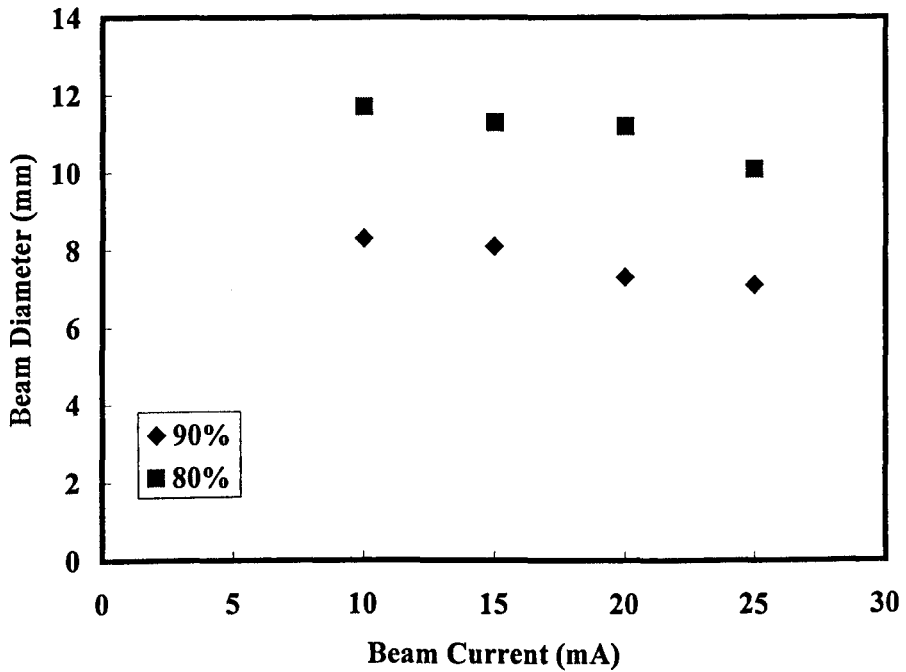


Fig.3.5 : Relationship between beam diameter for 90 % and 80 % uniformity and beam current

Distance below ion source (cm)	Type 1 grids diameter (cm)		Type 2 grids diameter (cm)	
	90 %	80 %	90 %	80 %
5.0	0.85	1.15	0.70	1.10
7.5	1.05	1.40	0.80	1.15
10.0	1.40	2.00	0.85	1.20
12.5	1.85	2.95	0.80	1.25

Table.3.2 : Relationship between beam diameter for 90 % and 80% uniformity and vertical distance below sources for Type 1 and type 2 grids

3.3.2 Effect of grid type on current density

The effect of grid optics on current density as a function of source-sample distance is shown in Fig.3.6. The "focused" Type 2 optics delivers significantly greater current densities (by up to a factor of 2) at short and intermediate distances. However, this performance is lost at greater distances as the beam diverges. The "uniform coverage" Type 1 arrangement produce slightly higher values compared with the "collimated" Type 3 grid at short distances on account of the steeper "top-hat" beam profile of the former. The data of Table.3.2 also indicate that the former arrangement is to be preferred in terms of beam profile.

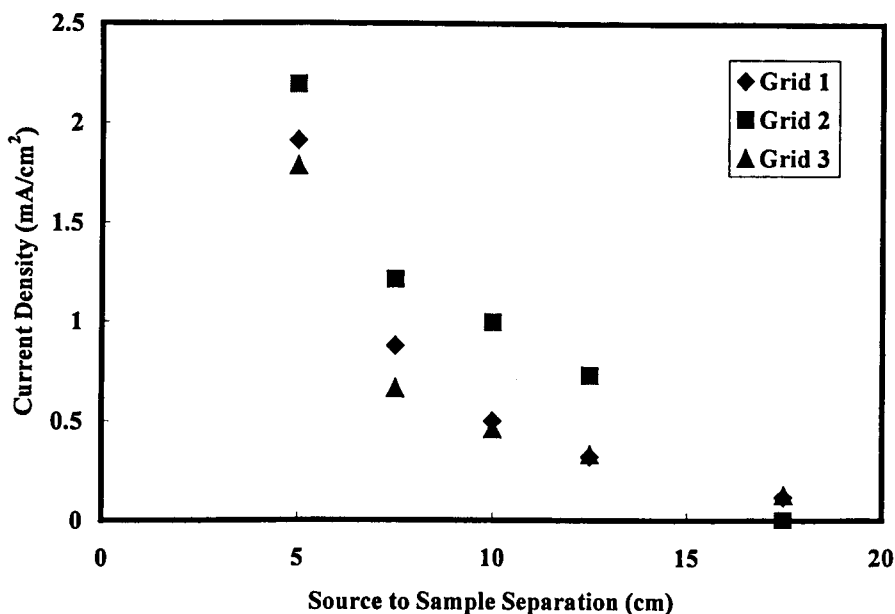


Fig.3.6 : Effect of grid type on current density

3.4 Summary

Ion beam technology is in widespread use in both materials processing and analysis. For such applications it is desirable to know the extent of beam non-uniformities because ion beams are rarely spatially uniform[52]. Ion beam spread, caused by charge repulsion, is a common problem in all area of low-energy ion beam work[53]. In IBSD experiments, beam divergence results in reduced current density on the target[54].

In this work the beam divergence was increased by a decrease of beam current, which half-angle from the beam perpendicular axis was 5°. This value found a good agreement with the minimum half-angle of 5 - 8° typically with 90 –

95 % of the beam within the divergence angle from the beam centre line[20]. Consequently, the beam profile and current density characteristics of the SIB source used in this work needed to be thoroughly evaluated. The neutraliser inhibited beam spread and increased the current densities by typically 50 %. Decrease of accelerator voltage was also effective to increase current densities, and separation of target and ion source should be minimised in order to increase current density.

These experiments clearly identified stable SIB operating conditions that were later required for IBSD.

4 ION BEAM SPUTTER DEPOSITION

4 Ion beam sputter deposition

4.1 Introduction

When TiNi alloy films are used for actuation purposes, it is important that the temperature hysteresis of the B2-R transformation is small and that thermal response is good. Generally, in order to grow TiNi alloy thin films, a pre-alloyed target has been used[55]. However, it is very difficult to control the TiNi composition, because films deposited by sputtering with such a Ti/Ni pre-alloyed target show Ti depletion and Ni enrichment. The difference in composition can cause a change of transformation temperature or structure of the TiNi films causing a change in film properties.

Generally, as-deposited TiNi alloy thin films grown by conventional sputtering methods such as RF and DC sputtering, and magnetron sputtering are amorphous. Typically the TiNi alloy films need annealing at 500 °C for 1 hour to crystallise. Alternatively, if the substrate temperature is kept over 200 °C, shape memory effect can be exhibited[55]. Smy *et al*[56] have calculated energy distributions of sputtered species at the substrate in magnetron discharge processes using Monte Carlo simulations, which suggest that < 1 % of the flux of Ti atoms sputtered at 10 mTorr (1.33 Pa) have energies exceeding 1 eV. In contrast, average energy of Ti and Ni neutrals in IBSD is likely to be around 15 – 20 eV[57]. Kinetic energies could be dependant on working gas

pressure, however the values for IBSD are possibly more than 10 times bigger than the calculated values for magnetron sputtering. However, Turner *et al* [58] obtained average kinetic energies of approximately ~ 10 eV at chamber pressures of 10 mTorr (1.33 Pa). Differences in energy distribution of depositing atoms would be assumed to play a significant role in accounting for the differences observed in the nature of TiNi films deposited by conventional sputter deposition and by IBSD.

Chapter 2 introduced IBSD as a method of producing thin films. In this study, the Kaufman type source was operated under high vacuum ($< 1.3 \times 10^{-3}$ Pa). Sputtered atoms were deposited onto substrates of silicon and glass. Thin films of, for example, aluminium, titanium and nickel, less than 5 μm thick, were produced by IBSD. These films were estimated by the deposition rate and sputtering yield. Non-alloyed, segmented, targets are proposed in order to readily control the composition of the TiNi alloy by adjusting the relative areas of Ti and Ni.

4.2 Arrangement of apparatus for IBSD

The schematic diagram of the geometrical set-up is shown in Fig.4.1. 125 mA of 1500 eV argon ions were drawn from the Kaufman source and used to sputter-deposit thin films ($< 2 \mu\text{m}$) onto substrates of glass and silicon. A 0.5 cm aperture was located 5 cm vertically below the Kaufman type source. The target was inclined at 45° to the vertical to maximise the sputtering yields and

mounted 2 cm away from the substrate. Targets of aluminium, titanium and nickel 50 μm thick were used.

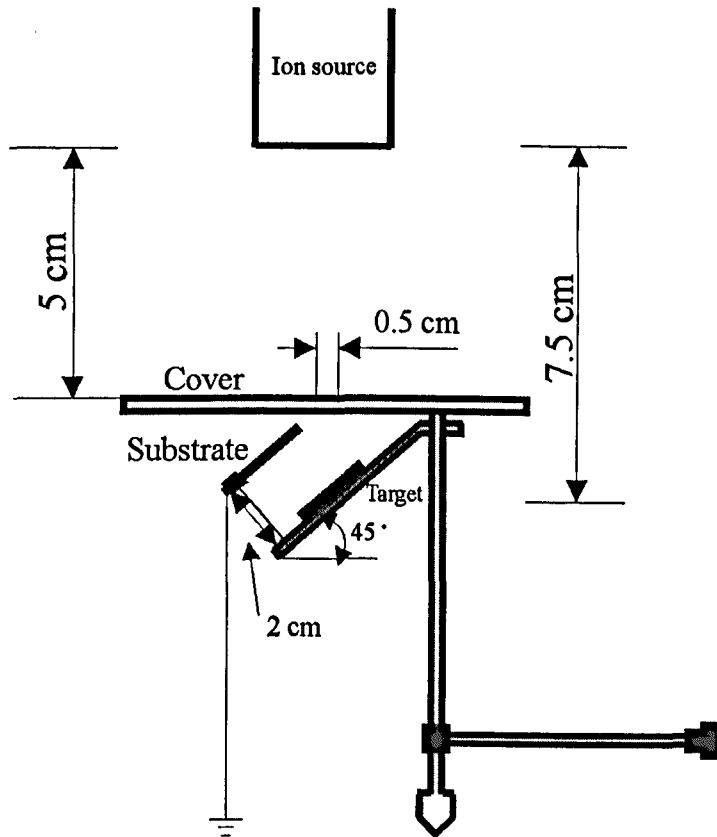


Fig.4.1 : Geometrical set-up for deposition

4.3 Target and substrate temperature as a function of sputtering

The equilibrium temperature during film deposition was measured at the target and substrate positions with a K-type thermocouple and shown as a function of time in Fig.4.2. The beam voltage and beam current are 1250 eV and 25 mA, respectively. Under the operating conditions used, the target and substrate reached equilibrium temperature of 220 °C and 170 °C respectively after 30 -

40 min. As described in Chapter 2, by the magnetron sputtering deposition method, temperatures at the substrate of 80 °C are reached in a high vacuum of 10^{-5} Torr (1.3×10^{-3} Pa). Substrate temperatures by ion beam sputter deposition are thus much higher than by magnetron sputtering. The temperature rise is mainly caused by the impact of secondary electrons. In magnetron sputter deposition, the temperature rise of the substrate is small because many electrons collide with residual gas molecules and lose energy before they reach the substrate.

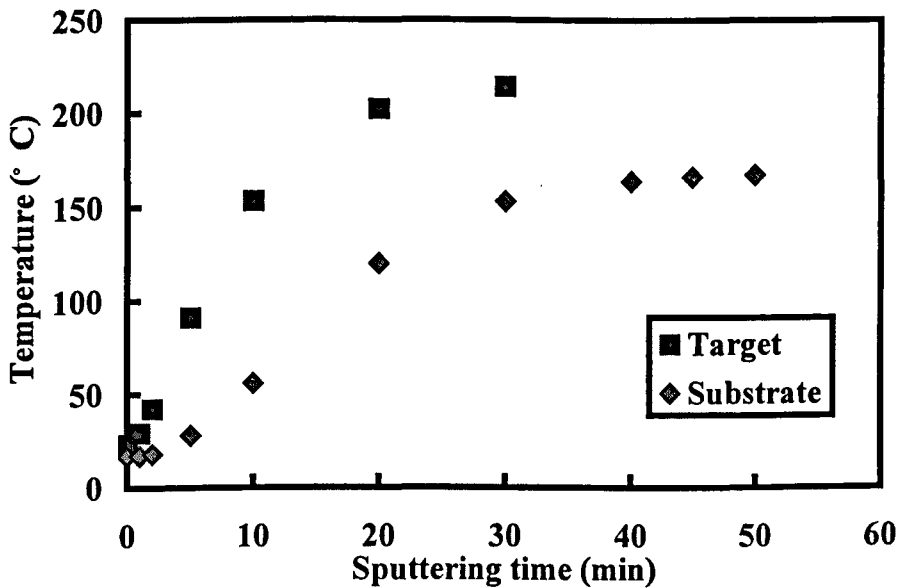


Fig 4.2: Target and substrate temperature as a function of sputtering time

4.4 Operating conditions for thin film deposition by ion beam sputtering

4.4.1 Sputtering yield from targets of Al, Ti and Ni

In thin film deposition, the sputtering yield is the most important quantitative value for sputtering. Table. 4.1 shows the relationship between the sputtering yields of various materials and various beam energies by irradiated Ar^+ ion[59,60]. The sputtering yields increase with the beam voltage and the values depend on the material. Fig.4.3 shows the relationship found by other workers between the sputtering yield[59,60] and atomic number for 600 eV Ar^+ ions. The sputtering yield gives the removal rate of surface atoms by ion bombardment. The atomic numbers of aluminium, titanium and nickel are 13, 22 and 28, respectively. However, the sputtering yields do not increase with the mass of materials. In the low energy region, the sputtering rate increases periodically in order of atomic number up to a maximum for univalent metals of the Ib group such as copper (Cu), silver (Ag) and gold (Au). The sputtering yields vary periodically with atomic number ; yields increase consistantly as the d-shells are filled. The deposition rate, however, is not only dependent on the sputtering yield. The deposition rates of different materials, sputtered under identical conditions, are related to the sputtering rates. However calculations of the deposition rates directly from the yield values are extremely difficult. The effects of secondary electrons are one of several complications. The values, shown in Table. 4.1, should be regarded only as a general guide.

	300 eV	600 eV	1000 eV	2000 eV
Al	0.65	1.24	2.0	2.0
Ti	0.33	0.58	-	1.7
Ni	0.95	1.52	2.1	-

Table. 4.1 : Sputtering yields of various materials for Ar⁺ ions[59,60]

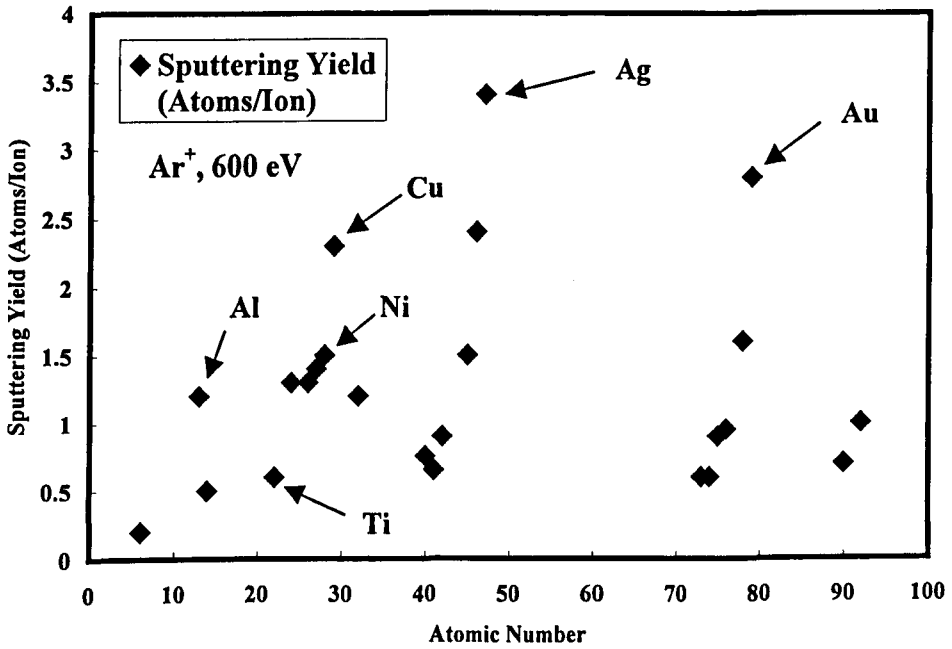


Fig.4.3 : Relationship between sputtering yield and atomic number for Ar⁺

(Selected elements are labelled) [59,60]

4.4.2 Relationship between film thicknesses, beam voltages and beam current

Optimum sputtering conditions were determined by varying the source operating voltage from 1000 to 1500 V and total ion current from 5 to 35 mA. Deposition rates were obtained by measuring film thicknesses with a stylus profilometer for total sputtering times up to 180 minutes. The film thickness for aluminium deposited onto silicon, is plotted in Fig.4.4 as a function of source operating voltage and relative position on the substrate. Aluminium targets were selected for these trials as they were inexpensive and furthermore, the sputter yield lies intermediate between that of Ni and Ti. Results for Al are therefore expected to be indicative of deposition rates for Ti and Ni. Silicon substrate are convenient because they are easy to polish. The total source current was 25 mA. This corresponded to a current density of $\sim 1 \text{ mA cm}^{-2}$ at the target. Position along the length of the substrate was defined relative to the foot of the perpendicular to the target plane from the centre of the ion beam bombarded area. Fig.4.5 illustrates the maximum aluminium film thickness on substrate as a function of beam voltage. At an incident ion energy of 1250 eV, the film thickness on the substrate is maximum. At greater energy, the film thickness falls with beam voltage. Fig.4.6 shows the maximum titanium film thickness on silicon substrate as a function of total beam current at a beam voltage of 1300 V. The rate of deposition increases with beam current at a given operating voltage. As the beam voltage increases, there is a steady increase in deposition rate up to around 1250 V. Beyond this operating voltage of 1250 V, there is a progressive decrease in the rate of deposition. Furthermore,

the uniformity of coverage of the substrate is best at around 1250 V. Clearly, above 1250 V, the deposition rate actually decreases even though the total power to the system increases. This operating voltage was therefore used for subsequent film deposition. The deposition rate was also shown to increase steadily with total beam current ; however, in order to maintain relatively low substrate temperatures, a maximum beam current of 25 mA was used throughout this investigation.

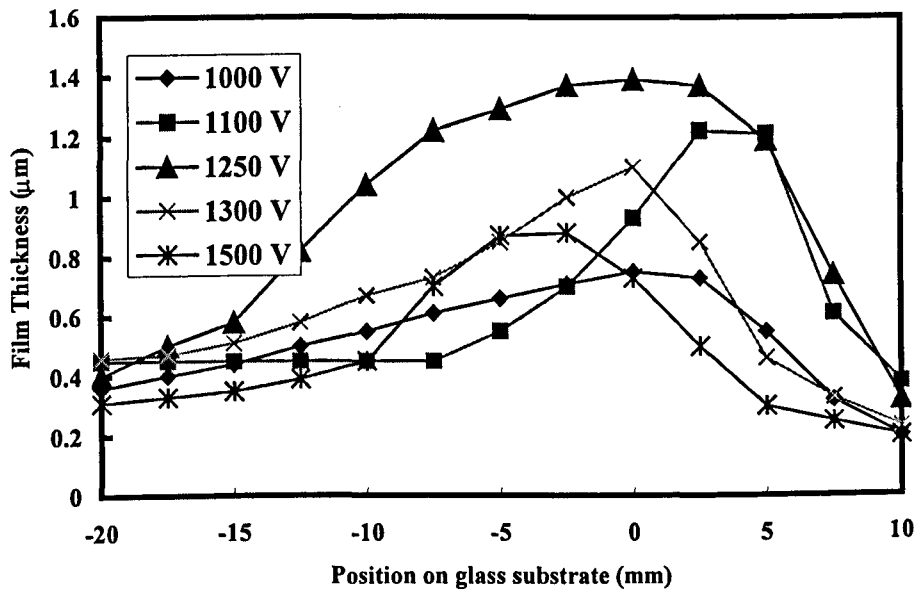


Fig.4.4 : Film thickness as a function of source operating voltage and position on the substrate

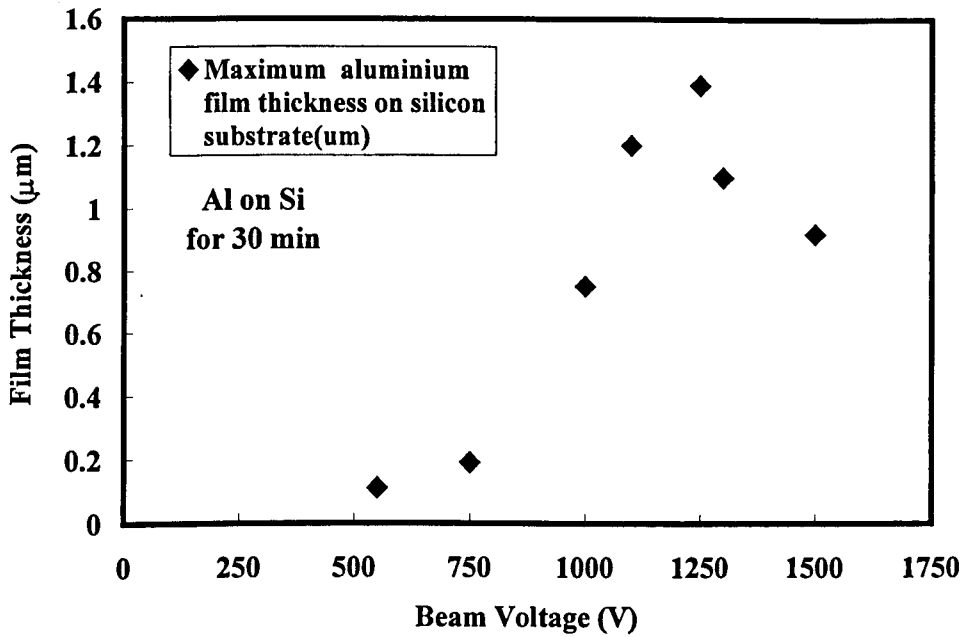


Fig.4.5 : Relationship between maximum aluminium film thickness on silicon substrate and source operating voltage

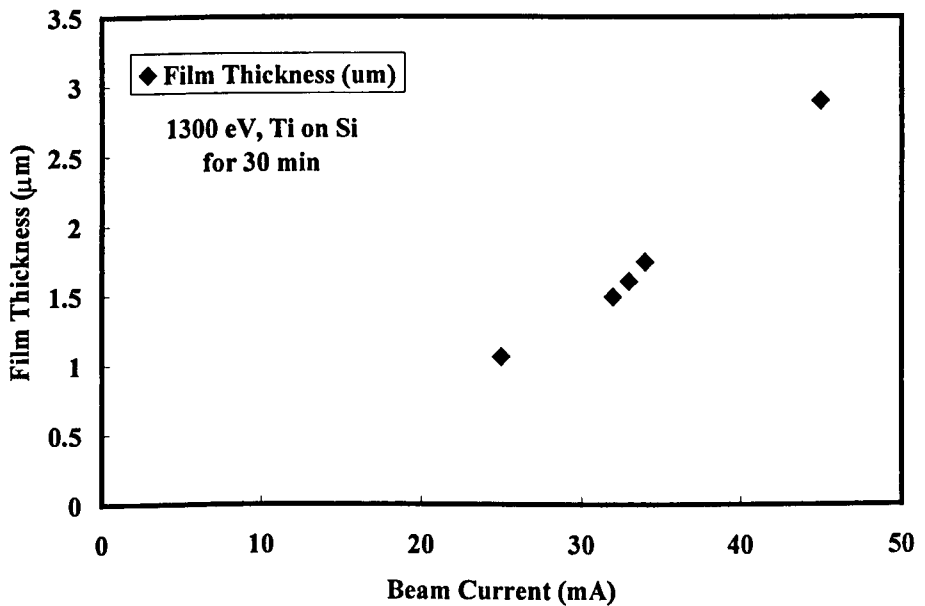


Fig.4.6 : Relationship between maximum titanium film thickness on silicon substrate and total beam current

4.5 Titanium-Nickel (TiNi) Alloys

4.5.1 TiNi thin film

TiNi alloy thin films have been investigated for possible use in many applications such as micro pump[61], micro arm[62] and micro robot gripper[63,64], etc. Generally, a low vacuum of around 0.8 Pa is used in order to deposit TiNi alloy films by magnetron sputtering. The transformation temperature of a TiNi thin film changes by 100 °C per percent change of the composition. In short, control of composition within 0.1 % in the range of 50.0 – 50.5 at % Ni[65] is required in order to maintain the accuracy of the transformation temperature. The technology, which produces the alloy, must be capable of this degree of control. In this study, it is demonstrated that ion beam sputtering, under high vacuum, has the necessary levels of control.

4.5.2 Target of Ti/Ni

Deposition rates for nickel and titanium were measured separately and under identical conditions in order to determine the relative areas required in a composite target for deposition of TiNi. Glass microscope slides (30 mm × 15 mm), washed with acetone and cleaned in an ultrasonic bath in methanol solution, were used as substrate. The long edges were oriented parallel to the plane of the diagram in Fig.4.1. The position along the length of the substrate was defined relative to the foot of the perpendicular to the target plane from the

centre of the ion beam bombarded area.

Fig.4.7 compares the measured film thickness following deposition onto glass substrates for a sputtering time of 30 minutes. The beam voltage and the total beam current were 1250 eV and 25 mA, respectively. The thicknesses of deposited Ti and Ni films were then measured by stylus profilometer. Within the experimental errors, the deposition rates were uniform over $\sim 70\%$ of the substrate area, for the geometry and source operating conditions used.

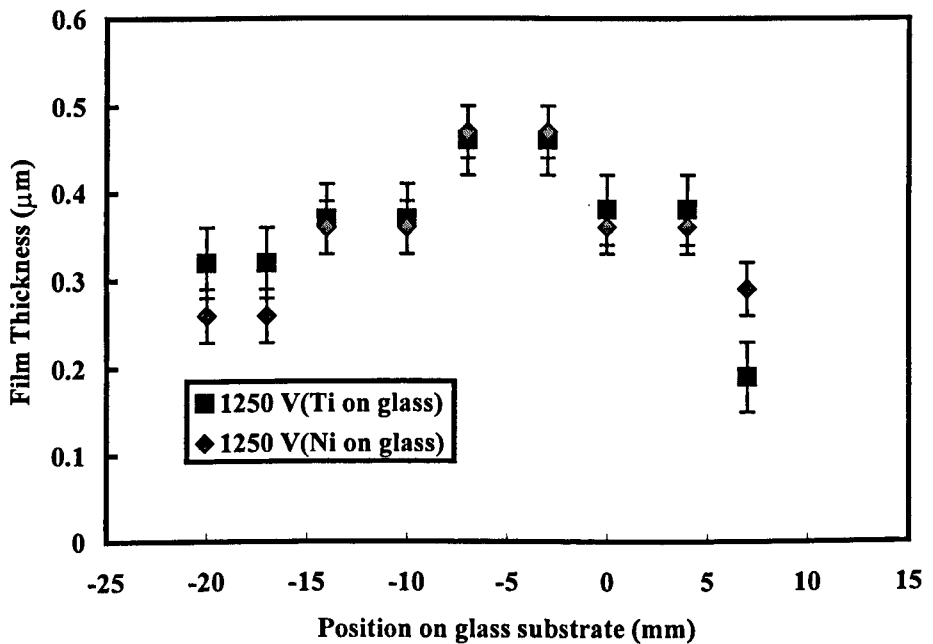


Fig.4.7 : Film thickness for Ti and Ni as a function of position

Consequently, to deposit stoichiometric TiNi, Ti/Ni targets in the form of sectorized disks of diameter 4 cm were fabricated, as shown in Fig.4.8. They

have eight 45 ° sectors alternating between Ti and Ni. The target used was a composite of 99.9 % nickel foil segments (50 μm thick), mounted on a 4 cm diameter 99.6+ % titanium foil disc (50 μm thick)[66].

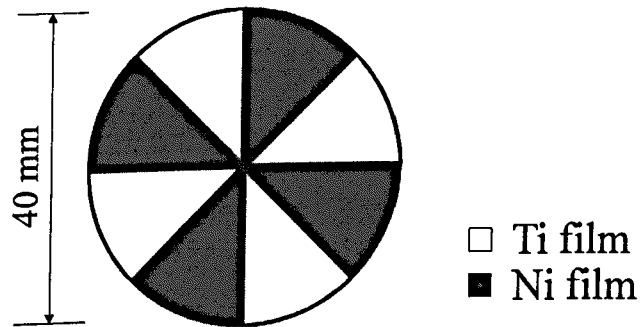


Fig.4.8 : Schematic of 8-sector Ti/Ni target
(Equal areas of Ti and Ni were used)

4.5.3 TiNi thin films produced by SIB

Fig.4.9 shows the relationship between thickness of the deposition and the relative position for TiNi film deposited onto an unheated glass substrate for a total deposition time of 180 min and a target/substrate separation of 2 cm. The deposition rate was about $\sim 0.5 \mu\text{m hr}^{-1}$, for incident ions of energy of 1250 eV and current 25 mA. The deposited films were observed to have a mirror finish, excellent adhesion to the substrate and appeared featureless when examined under an optical microscope.

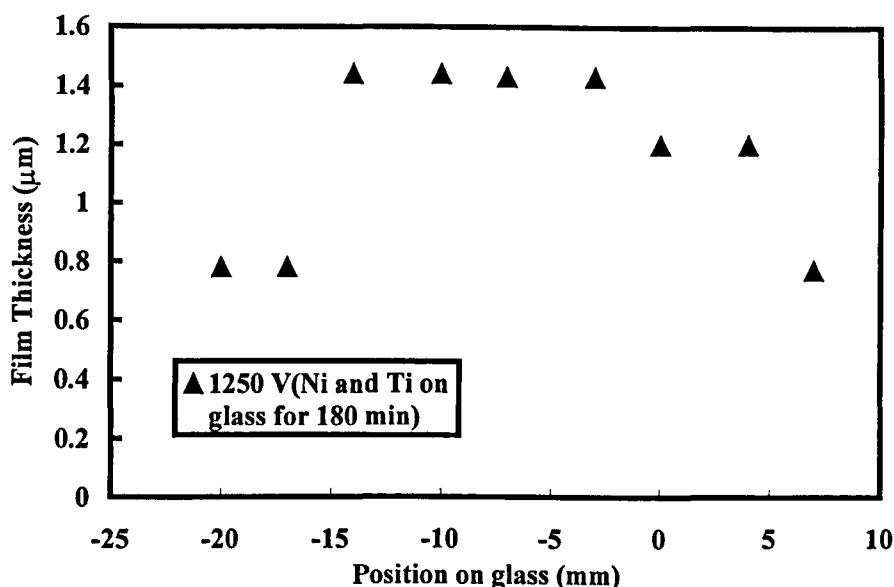


Fig.4.9 : TiNi film thickness as a function of position

4.6 Summary

Thin films of TiNi were produced by IBSD from a composite target. The operating conditions were optimised to produce uniform coverage and a low rise in the substrate temperature.

The measured deposition rates ($0.5 \mu\text{m hr}^{-1}$) were sufficiently high for typical applications. Within the experimental error, the rates measured for Ti and Ni separately were identical as shown in Fig.4.7. This information was used to develop segmented Ti/Ni targets. However the associated temperature rise of 170°C was significant.

Above a critical pressure of 25 mTorr (2.3 Pa), Smy *et al*[56] commented that

pure diffusion conditions apply for titanium with consequent thermalization of kinetic energy. The thermal equivalent of the average kinetic energies involved in the IBSD process is of the order 10^5 K so such large differences can be expected to have considerable effect on film growth conditions[67].

In the next chapter, the TiNi thin films deposited by IBSD will be characterised by electrical resistivity measurement, resistance measurement and x-ray reflectometry.

5 CHARACTERISATION OF TINI SHAPE MEMORY ALLOY THIN FILM

5 Characterisation of TiNi shape memory alloy thin films

5.1 Introduction

This chapter reports on the growth of TiNi shape memory alloy thin films by ion beam sputter deposition (IBSD) using the Kaufman-type source, for microactuator applications. TiNi thin films are deposited on unheated glass substrates by IBSD. The films were characterised by electrical resistivity measurements and x-ray reflectometry. R-phase and martensitic transformations were seen without high temperature annealing. The production of TiNi thin films having shape memory properties has been of particular interest. They are usually prepared by DC or RF magnetron sputtering[68,69,70]. The shape memory properties are compared with those of films prepared by DC and RF magnetron sputtering.

5.2 Properties of TiNi shape memory alloys

5.2.1 Crystal structure of martensitic phase

Fig.5.1 shows a simplified model of the shape memory effect mechanism. The martensite type transformation can be accurately defined as "lattice transformation by shearing deformation based on the cooperation motion of atoms"[71]. Fig.5.2 shows the relationship between the resistance curve and

transformation temperatures for TiNi. Single crystal parent phase TiNi is cooled to a temperature below M_f ($T < M_f$). The martensite phase then appears and the TiNi is then deformed. The original shape is recovered by reverse transformation upon heating to a temperature above A_f . On heating, the transformation phase for TiNi at $T > A_s$ is B19' martensite transformation to the parent phase (B2). This has a monoclinic structure (M-phase). At $A_s < T < A_f$, the transformation phase is M-phase and B2, then heating up above A_f , the transformation phase becomes B2. On cooling, at $T > M_s$, the transformation phase is B2, then, the transformation phase is M-phase and B2 at $M_f < T < M_s$. Below M_f , the transformation phase becomes M-phase.

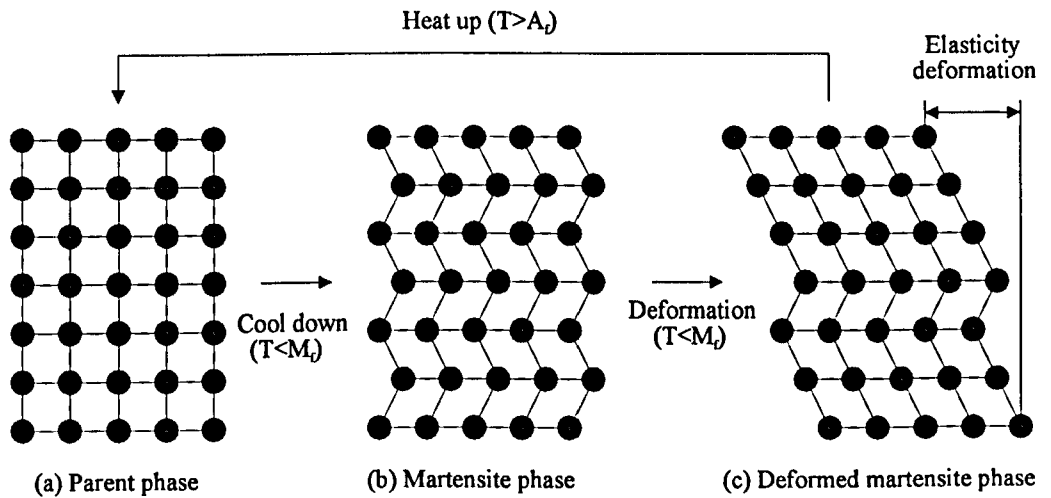


Fig.5.1 : Mechanism of shape memory effect[72]

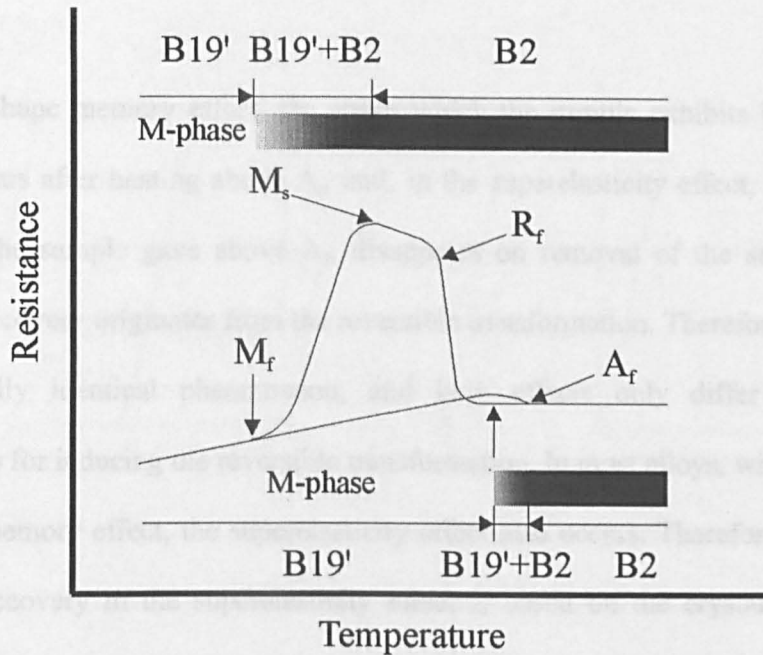


Fig. 5.2 : Diagram of resistance curve and transformation temperature for TiNi

5.2.2 Shape memory effect

Shape memory alloy is unique material, which recovers its original shape from the deformation when it is heated above the martensite temperature. Fig.5.3 shows three stress-strain curves. Diagram (a) shows normal metallic material. When the elastic region is permanently exceeded, it is deformed when unloaded. The original shape can be recovered in the shape memory alloy of (b), when it is heated up. At low temperatures below the martensite temperature, large strains remain. These strains disappear when it is heated above the austenite start temperature (A_s). Diagram (c) indicates super elasticity materials ; the original shape is recovered after unloading, when it is deformed. This phenomenon is observed in the high-temperature range above the austenite temperature.

In the shape memory effect, the strain which the sample exhibits below A_s , disappears after heating above A_f , and, in the superelasticity effect, the strain which the sample gave above A_f , disappears on removal of the stress. The shape recovery originates from the reversible transformation. Therefore, it is an essentially identical phenomenon, and both effects only differ between methods for inducing the reversible transformation. In most alloys, which show shape memory effect, the superelasticity effect also occurs. Therefore, perfect shape recovery in the superelasticity effect is based on the crystallographic reversibility of the transformation, as is transformation in the shape memory effect. Fig.5.4 shows the relationship between the critical stress for slip and temperature in regions where shape memory effect and superelasticity are observed. If the stress for slip is above line (A), slip never recovers upon heating or unloading. If the stress is below line (B), the superelasticity effect should not appear. In Fig.5.4, shape memory and superelasticity effects can occur in the region between lines (A) and (B).

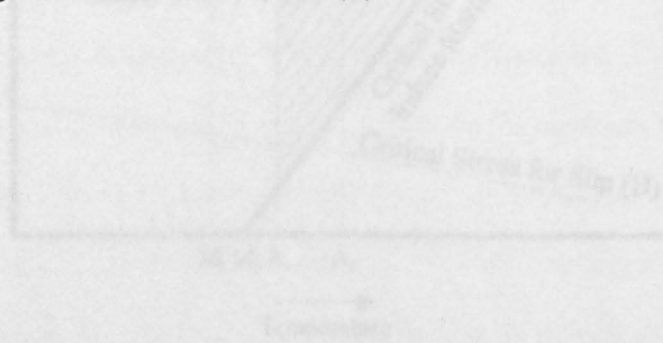
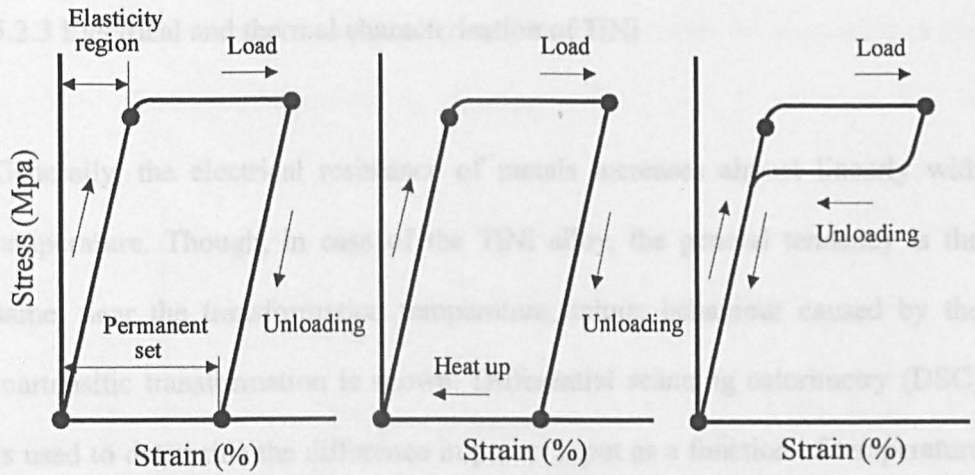


Fig 5.4: Schematic diagram showing the region of shape memory effect and superelasticity in temperature-stress space. (A) represents the critical stress for the case of a high critical stress and (B) representing the critical stress for a low critical stress.



(a) Normal metal (b) Shape memory alloy (c) Super elastic alloy

Fig.5.3 : The stress-strain curve of shape memory alloy

and super-elastic alloy[73]

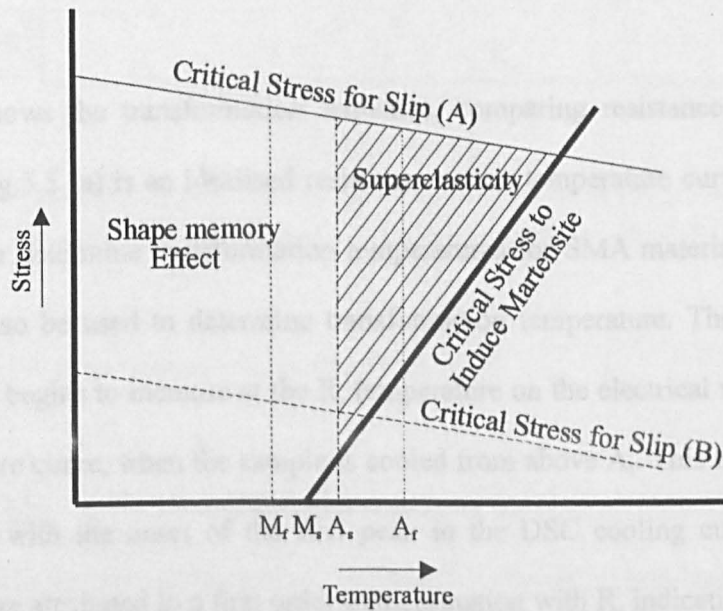


Fig.5.4 : Schematic diagram representing the region of shape memory effect and superelasticity in temperature-stress coordinates; (A) represents the critical stress for the case of a high critical stress and (B) represents the critical stress for a low critical stress[55]

5.2.3 Electrical and thermal characterisation of TiNi

Generally, the electrical resistance of metals increases almost linearly with temperature. Though, in case of the TiNi alloy, the general tendency is the same, near the transformation temperature unique behaviour caused by the martensitic transformation is shown. Differential scanning calorimetry (DSC) is used to determine the difference in power input as a function of temperature to both sample and a standard. In order to equalise the temperature of sample and standard, the DSC adjusts the power input for a given heating or cooling rate. A convenient rate for heating or cooling is 10 ± 0.5 °C/min. In the case of the shape memory alloy, it is possible to obtain transformation temperatures from the DSC data.

Fig.5.5 shows the transformation sequence, comparing resistance and DSC curves. Fig.5.5 (a) is an idealised resistance versus temperature curve that can be used to determine transformation temperatures for SMA materials. Fig.5.5 (b) can also be used to determine transformation temperature. The electrical resistance begins to increase at the R_s temperature on the electrical resistance - temperature curve, when the sample is cooled from above A_f . This temperature coincides with the onset of the first peak in the DSC cooling curve. These changes are attributed to a first order transformation with R_s indicating the start temperature of the R- phase change, ie onset of the transformation to the rhombohedral phase. The second peak in the DSC curve shows the change from the R- phase to the B19' phase. This corresponds to a decrease in

electrical resistance, which is the M_s temperature, namely, the beginning of the $R \rightarrow B19'$ phase transformation.

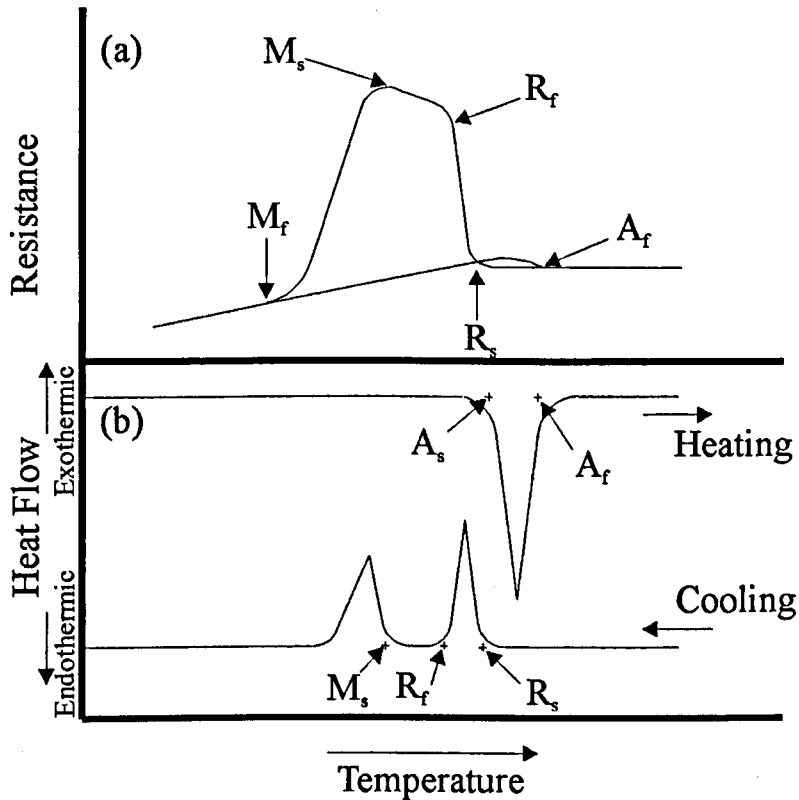


Fig.5.5 : Schematic diagram of electrical resistivity versus temperature curve (a) and DSC curve (b) of a TiNi shape memory alloy[55]

5.3 Deposition of TiNi shape memory alloy thin films

TiNi thin films have previously been deposited by several techniques. These include vacuum vapour deposition, DC and RF sputtering and laser ablation. According to Ikuta *et al*[74], TiNi thin film deposition presents several problems such as control of composition of the target and contamination during processing.

The phase transformation temperature of TiNi shape memory alloy is extremely sensitive to the composition of the alloy. As the proportion of nickel rises from 50 % to 50.5 %, the rate of transformation temperature rises by 100 °C / % [65]. During deposition of TiNi thin film, the sample can become contaminated due to wall-bombardment in the chamber. Contamination could also occur due to the pressure of the working gas.

It is likely that in thin film deposition, DC and RF magnetron sputtering techniques will be applied more for commercial use. The deposition rate by DC and RF magnetron sputtering is greater than other deposition techniques. However, after thin film deposition, high temperature annealing is needed. Generally an annealing temperature of 500 - 550 °C must be maintained for 20 - 30 minutes in order for the alloy to exhibit the shape memory effect.

5.3.1 Annealing temperature of TiNi shape memory alloy deposited by magnetron sputtering

Various authors have investigated the use of conventional DC magnetron and RF magnetron sputtering to deposit TiNi thin films. In order to exhibit SMA properties it is found that films grown by magnetron sputtering must be deposited on substrates at elevated temperature or subjected to post-deposition annealing. Amorphous TiNi is formed in the as-deposited state and typically annealing must be carried out at 500 - 550 °C for 10 - 60 minutes in order to

exhibit the shape memory effect. A major drawback for microsystems applications is that these processes are largely incompatible with directly integrating SMA thin film growth with other MEMS fabrication technologies.

Annealing temperatures and annealing times, as quoted by various authors, are shown below in Table.5.1. From Table.5.1, annealing temperatures of 450 – 500 °C and annealing times around 1 hour have been commonly used. According to K. R. C. Gisser[75], the shape memory effect was observed after deposition by magnetron sputtering on substrates heated to ~ 460 °C.

Magnetron sputtering		
	Annealing Temperature	Annealing Time
K.R.C.Gisser	540 °C	20-30 min
S.Miyazaki	450 °C	1 h
E.Quandt	700 °C	1 h
Y.Nakata	450-500 °C	10 min

Table.5.1 : Annealing temperatures and times using magnetron sputtering quoted by various authors[75,77,76,78]

5.3.2 Conditions for IBSD, compared with magnetron sputtering

Control of the film quality is compromised because the magnetron sputtering takes place at relatively high chamber pressures of typically 10 - 200 mTorr (1.3 - 26 Pa), and it is limited because the current density and voltage cannot be independently controlled except by varying the working gas pressure. In contrast, IBSD using a Kaufman type source operates with much lower chamber pressures in the 0.05 - 0.5 mTorr (6.5 - 65 mPa) range. This allows

independent control of energy and current density of the bombarding ions with consequent improvement in film quality.

Conditions such as working pressures used by various authors, are introduced below. In Table.5.2, deposition rates by magnetron sputtering are 2 – 10 $\mu\text{m/h}$. These rates are 4 – 20 times bigger than those for ion beam sputter deposition. The deposition rate, however, is dependent on the pressure of the working gas. Under the condition of same current and voltage, the deposition rate could be increased with a working pressure below 17 Pa[79]. In ion beam sputtering, the working pressure is lower than that for magnetron sputtering, but the sputtering rate is much smaller than that of magnetron sputtering. However, under high vacuum as used for ion beam sputtering deposition, sputtered atoms suffer much less scattering by the residual gas atoms. For example, T.Smy *et al*[56] investigated the change of kinetic energy of titanium atoms with change of pressure of gas during magnetron sputtering. The power and range of gas pressures of the gas are 100 W and 5 - 25 mTorr (0.65 – 3.15 Pa), respectively. With increase in gas pressures where average number of scattering events rises, and the distribution of kinetic energy of sputtered atom enlarges toward the limiting form, the fraction of kinetic energy of particles for titanium decreases dramatically. Additionally, increase of gas pressure causes a decrease in kinetic energy of sputtered atoms, which could influence thin film grown characteristics.

Magnetron sputtering			
	Argon Pressure	Deposition rate	Cathode Power
D.S.Grummon	0.73 (Pa)	2.34-3.31 ($\mu\text{m/h}$)	619-644 (W)
K.R.C.Gisser	0.27 (Pa)	2 ($\mu\text{m/h}$)	
P.Krulevitch	1.1 (Pa)	2 ($\mu\text{m/h}$)	
H.Holleck	0.4 (Pa)	6.7 ($\mu\text{m/h}$)	300 (W)
E.Quandt	0.4 (Pa)	10 ($\mu\text{m/h}$)	300 (W)
Ion beam sputtering			
K.Tsuchiya	0.05 (Pa)	0.5 ($\mu\text{m/h}$)	

Table.5.2 : Argon pressure, deposition rate and cathode power using magnetron sputtering by various authors, compared with ion beam sputtering deposition[80,75,81,82,76]

5.4 TiNi thin film characterisation by X-ray reflectometry

The SMA films were characterised by x-ray reflectometry using grazing incidence x-ray analysis (GIXA). Effects observable in GIXA include fluorescence, diffraction, evanescent wave propagation, specular reflection and diffuse scatter[83,84], all of which yield information on surface and sub-surface properties (as shown in Fig.5.6). The GIXA software program, which was produced by Bede Science Instruments Ltd. in the UK, has worked on the principles of calculating the electric field inside the materials then multiplying the appropriate cross-section for scattering or fluorescence.

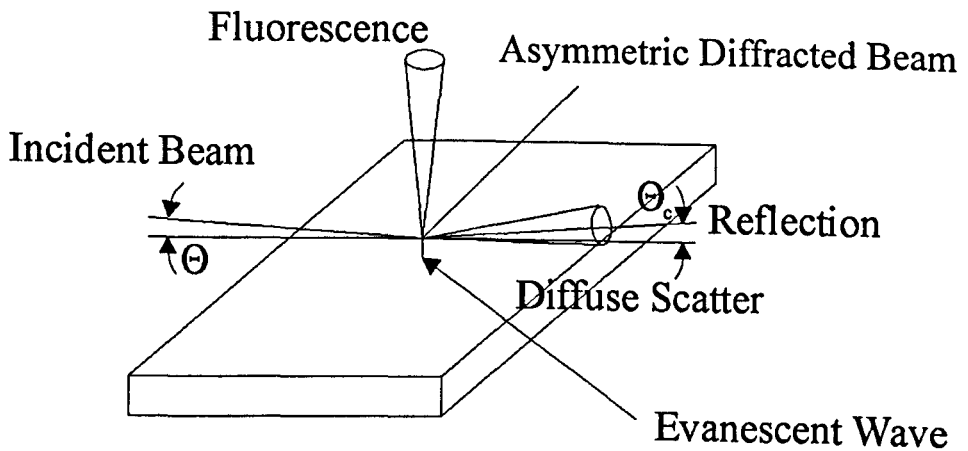


Fig.5.6 : Effect observable from grazing-incident X-ray scattering

5.4.1 Physical principles of X-ray reflectometry

The intensity as a function of angle in grazing incidence X-ray scattering measurements offers statistical information about the surface. Refractive index n of materials for X-rays is given by :

$$n = 1 - \delta - i\beta$$

where δ and β are the real and imaginary parts of the refractive index n of the material. δ and β are dependant on the X-ray wavelength and the composition of the material being examined. However, the values of δ and β are both small, ranging from approximately 10^{-8} for hard X-rays ($\lambda \approx 0.01$ nm) to approximately 10^{-2} for very soft X-rays ($\lambda \approx 10$ nm)[84]. The index of complex refraction takes the effect of absorption into consideration. Total external reflection will occur below a certain critical angle θ_c . In this region, the X-ray beam penetrate a

small distance into the scattering material. Typically, the critical angle for total reflection of X-rays is a fraction of a degree. When the observed intensities agree with the theoretically calculated spectrum, the value of thickness, density and roughness of each layer in the film are obtained. Reflection-factor R defined as the ratio of the intensities of the reflected and incident X-rays, and is calculable from the reflection-coefficient r as :

$$R = |r|^2.$$

The reflection coefficient is given by the Fresnel expression :

$$r = \frac{k_{j-1} - k_j}{k_{j-1} + k_j}$$

where k_j (perpendicular wave vector in data j) is given by :

$$k_j = \left(\frac{2\pi}{\lambda} \right) (n_j^2 - \cos^2 \theta)^{1/2}$$

where n_j is the index of refraction of component j . Layered materials can be also analyzed using the above formalism. X-rays are reflected and transmitted at each interface. For interference between X-rays reflected at the various interfaces, frequently called Kiessing fringes, the fringes are seen in a reflection factor[85]. Extraction of layer densities and thicknesses are optimised by fitting a model from the reflectivity measurements. The parameters of the simulation model included the order of the layer and approximate composition, thickness, etc. Then, the reflection factors are calculated, and are compared with the experimental measurements. This

calculation is repeated until the calculated values approximate closely enough to the measured reflectivity values.

5.4.2 Characterisation of TiNi thin films

Measurements of specular reflectivity curves for TiNi films deposited on silicon substrates were made using copper $K\alpha$ radiation. The experimental data was fitted to the distorted wave Born approximation theory by varying the simulation parameters. The film was modelled as a homogenous layer of thickness 1500 nm with a 30 nm surface contamination layer having reduced normalised density. Table.5.3 gives the composition and density parameters required to give best fit at the critical angle to the data of Fig.5.7 (a), using a two layer model. The vertical axis shows the x-ray intensity in counts sec^{-1} and the horizontal axis shows the angle of reflection in seconds of arc. The data is consistent with near equi-atomic composition of the TiNi film. The extreme sensitivity of the technique to changes in composition is also indicated in Fig.5.7 (a), where the simulation has been run for situations when the nickel comprises 25 % and 75 % of the surface (30 nm) layer. Effects of changes in film density are illustrated in Fig.5.7 (b). Normalised to the theoretical density of TiNi, the simulation has been run for densities of 0.5, 0.75 and 1.0 of the theoretical value. Best fit to the experimental data, according to Fig.5.7 (b), is obtained for a normalised density of 1.0.

Layer	Composition (x)	Normalised Density	Thickness (nm)
Substrate Si	1.0	1.0	substrate
SMA film Ti(x)Ni(1-x)	0.5	1.0	1500
Surface layer Ti(x)Ni(1-x)	0.5	0.98	30

Table.5.3 : Parameters used to fit the x-ray reflectometry data in Fig.5.7

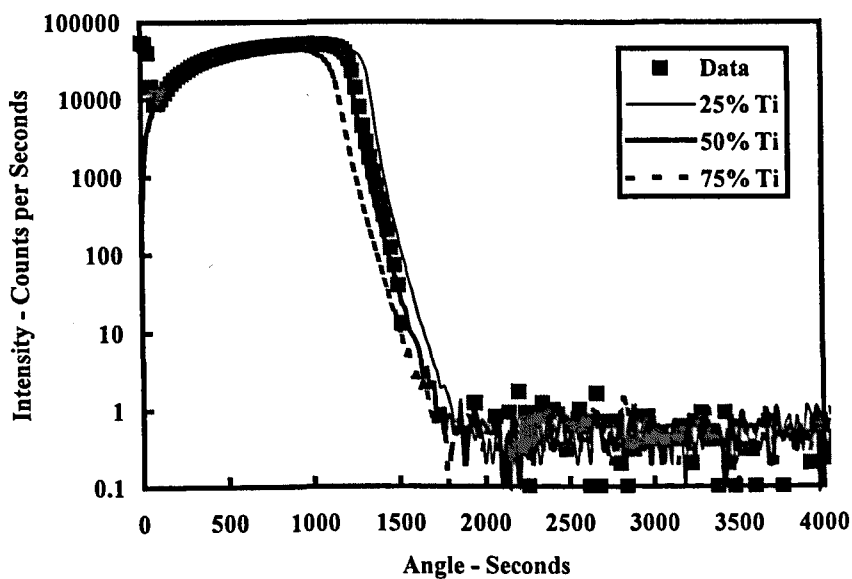


Fig. 5.7 (a): X-ray intensity versus angle of reflection for grazing angle reflection from TiNi film, where the best fit to the experimental data was obtained by varying the composition for a fixed normalised density of 1.0

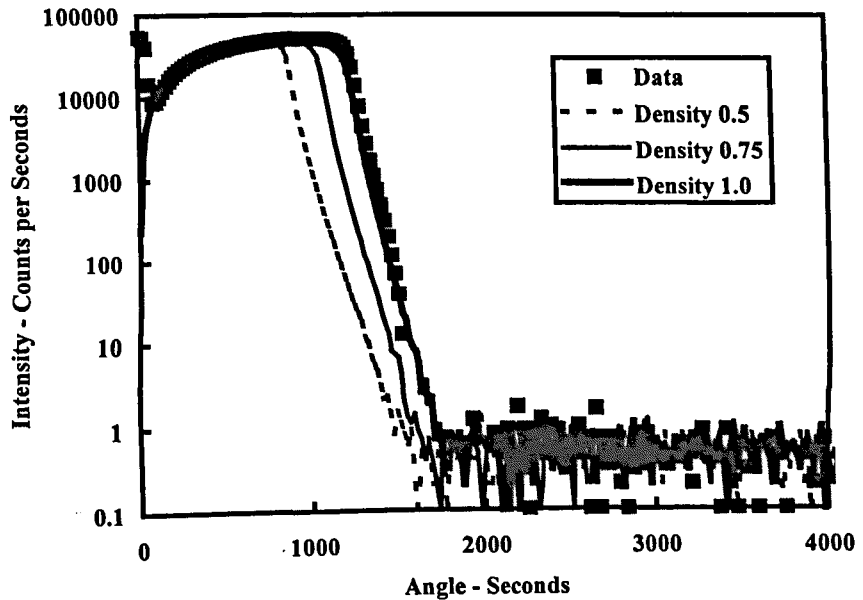


Fig.5.7 (b) : X-ray intensity versus angle of reflection for grazing angle reflection from TiNi film. Best fit to the experimental data is obtained by varying the normalised density for a fixed equi-atomic composition

5.5 Electrical Characterisation of TiNi thin films

5.5.1 Resistivity of TiNi thin films

Room temperature resistivities for TiNi thin films were measured at various points on glass substrates using the four-point probe method and average values were obtained. The data plotted in Fig.5.8 correspond to the film thickness measurements of Fig.4.9 and show resistivity values of around $1 \mu\Omega\cdot\text{m}$ over areas of uniform thickness of deposition. Average film thicknesses were $\sim 1.5 \mu\text{m}$ over 20 mm regions of the substrate. Table.5.4 shows resistivity, composition and film thickness for TiNi shape memory alloy, which were

measured by various authors. Resistivities were measured by K.Ikuta[86] and M.Kohl[87] at room temperature of 20 °C. According to Table.5.4, those resistivities for TiNi shape memory alloy are around 1 $\mu\Omega.m$, dependant on composition.

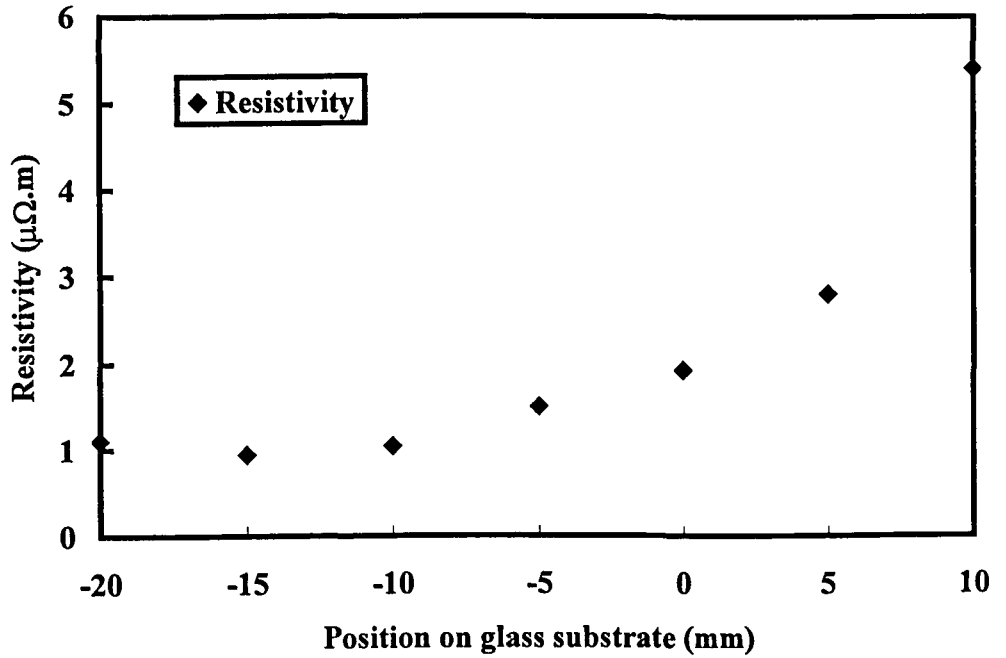


Fig.5.8 : Resistivity of TiNi film versus relative position

	Resistivity ($\mu\Omega .m$)	Composition (at.%Ni)	Film Thichness (μm)
H.Holleck	0.84	54	10
K.Ikuta	1.2	51.7	-
A.D.Johnson	0.06-0.1	-	20
M.Kohl	1.24	49.6	8

Table.5.4 : Resistivity, composition and film thickness for TiNi shape memory alloy by various authors[82,86,69,87]

5.5.2 Resistance of TiNi thin films

The behaviour of film resistance as a function of temperature during thermal cycling from room temperature to 165 °C is shown in Fig.5.9. On heating, the line of best fit to the data points gives a temperature coefficient of resistance for the TiNi film of $4.7 \times 10^{-3} / ^\circ\text{C}$, compared with tabulated values of $3.8 \times 10^{-3} / ^\circ\text{C}$ for pure titanium and $6.0 \times 10^{-3} / ^\circ\text{C}$ for pure nickel. A change in slope of the resistance- temperature characteristic from $9.8 \times 10^{-3} \Omega / ^\circ\text{C}$ below 50 °C to $3.2 \times 10^{-3} \Omega / ^\circ\text{C}$ above 100 °C is indicative of the austenitic transition with the austenite start (A_s) and austenite finish (A_f) temperatures estimated as 60 °C and 85 °C respectively. Upon cooling, the onset of the rhombohedral (R-phase) transformation and martensitic transformation (M_s) occur at 62 °C and 50 °C, respectively.

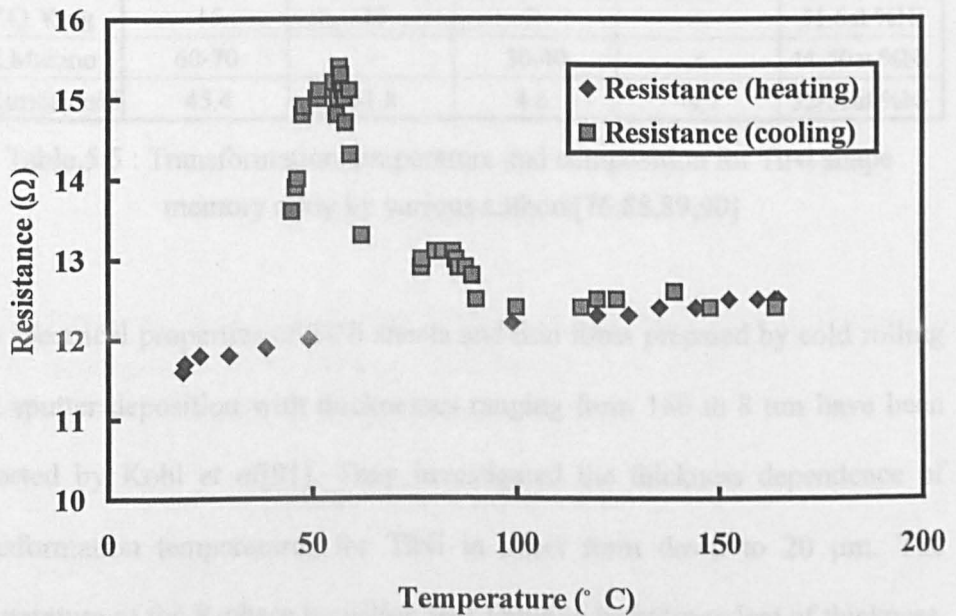


Fig.5.9 : Resistance of TiNi film during thermal cycling

Table.5.5 shows transformation temperatures and composition for TiNi shape memory alloy measured by various authors. E.Quandt, Y.Q.Yang and K.Kuribayashi used magnetron sputtering to deposit those TiNi thin films, and E.Makino used vacuum evaporation to produce TiNi thin film. The transformation temperatures are significantly different with considerable dispersion. Differences in the transformation temperatures could be due to annealing temperature and age-treatment in Ni-rich thin films as suggested by S.Miyazaki *et al*[77]. They investigated transformation temperatures in sputter deposited TiNi thin films and concluded they are strongly influenced by age-treatment in Ni-rich thin films.

	A_s (° C)	A_f (° C)	M_s (° C)	M_f (° C)	Composition
E.Quandt	24	32	7	-38	46at.%Ni
Y.Q.Yang	16	28	2	-	51.6at.%Ni
E.Makino	60-70	-	30-40	-	44-50at.%Ni
K.Kuribayashi	45.4	51.8	4.6	-4.7	52-56at.%Ni

Table.5.5 : Transformation temperature and composition for TiNi shape memory alloy by various authors[76,88,89,90]

The electrical properties of TiNi sheets and thin films prepared by cold rolling and sputter deposition with thicknesses ranging from 160 to 8 μm have been reported by Kohl *et al*[91]. They investigated the thickness dependence of transformation temperatures for TiNi in sheet form down to 20 μm . The temperature of the R-phase transition was found to be independent of thickness, however M_s showed a significant reduction at a thickness below 45 μm which

was attributed to a grain size effect. A plot of transformation temperature versus Ni content, which is shown in Fig.5.10, for film thicknesses of 1 – 2 μm , shows agreement with the R-phase transitions observed in the present work for 50 at.%Ni. Agreement is also found with values quoted by Gyobu *et al*[65], relating to 10 μm sputter deposited TiNi films, for both R-phase and M_s temperatures at equi-atomic composition.

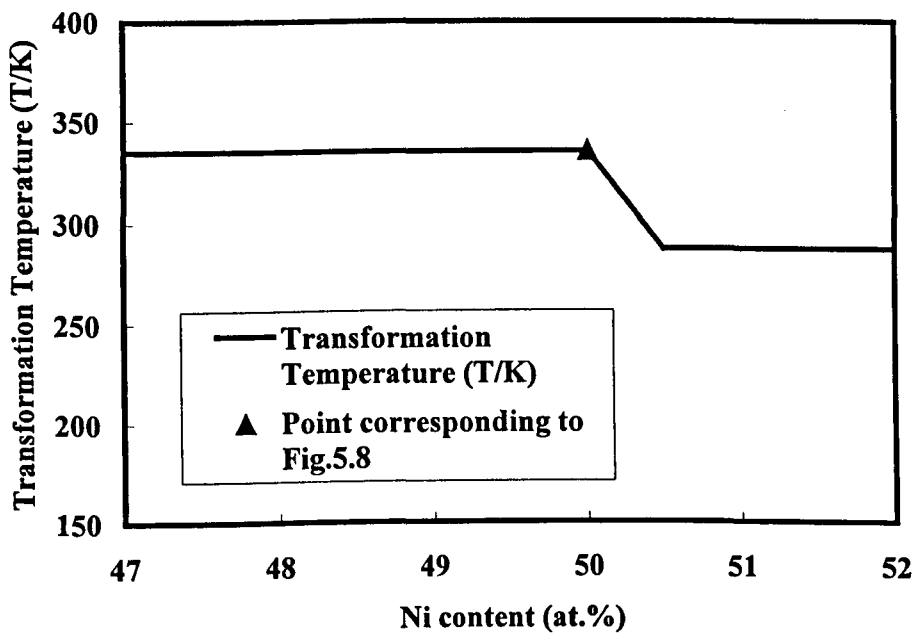


Fig.5.10 : Start temperatures of $B2 \leftrightarrow R$ transformation of TiNi alloy films crystallised by holding at 773 K for 3.6 ks, plotted against Ni content[65] (The point is corresponding to Fig.5.8)

5.6 Summary

Thin films of TiNi shape memory alloy were produced by the IBSD method. The deposited TiNi films were characterised by measuring film resistance as a function of temperature and electrical resistivity of the films. The resistance-temperature curves indicated Martensitic, Austenitic and Rhombohedral phase changes associated with the shape memory effect. In contrast with films grown by magnetron sputtering, these films exhibit shape memory properties without high temperature annealing and can be deposited onto unheated substrates. The electrical resistivities showed excellent agreement with published data. The films were also characterised by GIXA and the experimental data were compared with theoretical simulation. The results indicated that the SMA films were of near equi-atomic composition and of density close to the theoretical value for TiNi.

6 THERMAL CHARACTERISATION OF TINI SMA THIN FILMS

6 Thermal characterisation of TiNi SMA Thin films

6.1 Introduction

In this investigation, TiNi SMA samples, which had been grown by ion beam sputter deposition, were characterised by temperature-time profile measurements. This was done in order to obtain values of thermal parameters influencing microactuator operation and behaviour and to measure phase changes indicative of the shape memory effect. For the derivation of thermal parameters, large samples of area of 1 - 5 cm² were prepared. Thermal equilibrium and non-equilibrium temperature measurements were made on these samples by both direct thermocouple contact and by thermal imaging. Generally, phase transformation temperatures have been measured in TiNi shape memory alloys by using Differential Scanning Calorimetry (DSC). Measurement of transformation temperatures by DSC is highly reliable and repeatable. TiNi shape memory alloy thin films with lateral dimensions of less than a millimetre will be required for numerous applications. Transformation temperatures for such micro components cannot be easily measured. As an alternative method, samples were also prepared using simple lithographic techniques for characterisation of response times by the non-contact measurement technique of thermal imaging.

6.2 Thermal modelling

Observations of phase changes in TiNi SMA thin films using Differential Scanning Calorimetry (DSC) have been reported in the literature by several authors including, for example, Busch *et al*[68]. In the bulk material, changes in specific heat capacity of approximately a factor of five occur[92] as the material undergoes a phase transition. This change is readily observable as the power increase or decrease required to maintain constant rate of change of temperature in DSC measurements. Here an alternative strategy is adopted. The heating power is kept constant and the rate of change of temperature is measured. Direct electrical Joule (I^2R) heating is used to heat the sample by passing current from a constant current source through the film and the thermal behaviour described by a simple model as shown schematically in Fig.6.1.

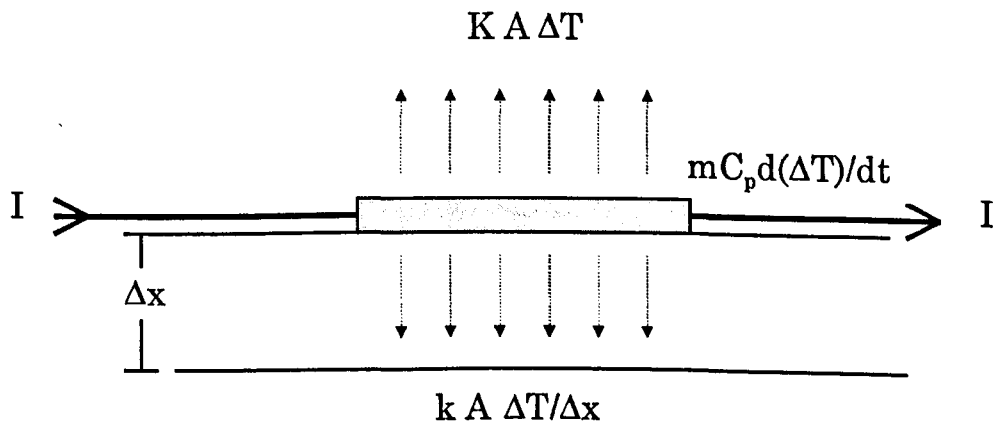


Fig.6.1 : Heat flow during heating of SMA thin film by electrical current

The balance of input power with radiated heat, heat loss by conduction and useful heat in raising the temperature of the sample is expressed by :

$$P = mC_p \frac{d(\Delta T)}{dt} + KA\Delta T + kA\left(\frac{\Delta T}{\Delta x}\right) \quad \text{Equation 6.1}$$

where

- P is the total electrical power dissipated in the sample;
- m is the sample mass;
- C_p is the sample specific heat;
- ΔT is the temperature rise above ambient temperature;
- K is the radiative heat transfer coefficient;
- A is the sample surface area;
- k is the thermal conductivity of the substrate;

and

- Δx is the substrate thickness.

From Eq.6.1 an approximate five-fold increase/decrease in $d(\Delta T)/dt$ is implied for a five-fold decrease/increase in C_p . Phase changes in the TiNi SMA films should thus be measurable by observing the rate of increase or decrease of film temperature as a function of time for constant power input provided that the thermal mass of the film is not swamped by the thermal mass of the sensor. Maximum rates of heating can also be calculated from Eq.6.1 and, under steady-state conditions, $d(\Delta T)/dt = 0$ and the radiative heat transfer coefficient can be obtained as $K = P/(A\Delta T)$ if negligible heat is lost by conduction. Measurements of the radiative heat transfer coefficient enable rates of cooling to be predicted and hence realistic maximum cycling times for TiNi SMA microactuators estimated.

Idealised temperature and temperature gradient versus time relationships for the endothermic and exothermic phase transitions to be expected during thermal cycling of SMA materials are shown in Fig.6.2 (a) and 6.2 (b). For constant input power, an endothermic reaction will produce an arrest in temperature rise of the sample due to the heat required to drive the reaction. Conversely, an exothermic reaction will produce an arrest in temperature fall due to heat liberated during the phase change. For example, modelling the temperature rise as an exponential increase, Fig.6.2 (a) shows the effect to be expected on the temperature profile and on the gradient due to an endothermic phase transition. Fig.6.2 (b) models the temperature fall as an exponential decrease and shows the effect of an exothermic phase transition on the temperature profile and gradient.

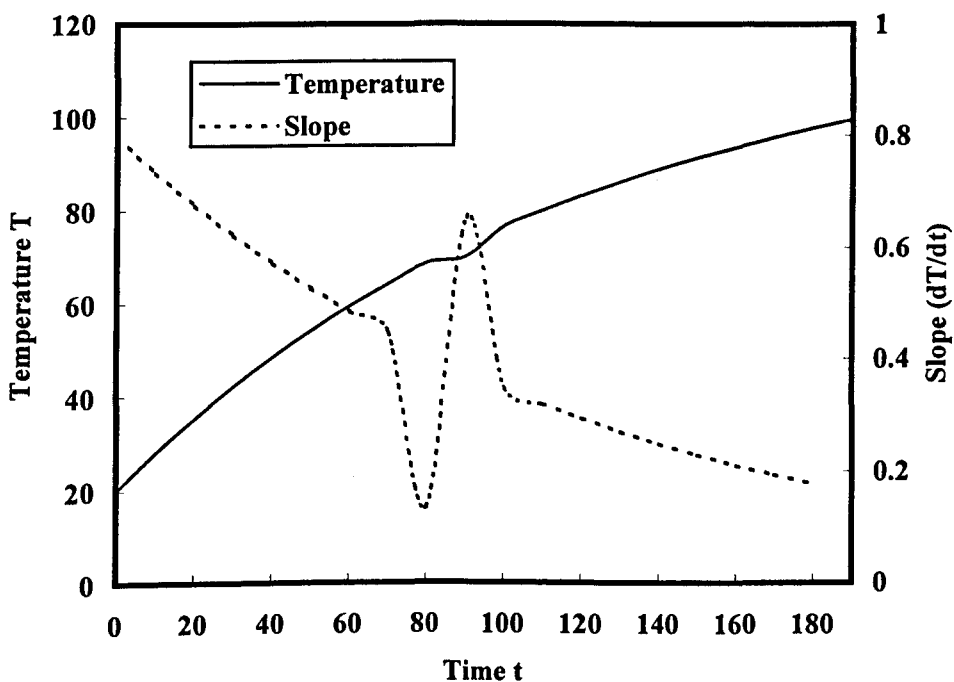


Fig.6.2 (a) : Effect of endothermic phase change during sample heating

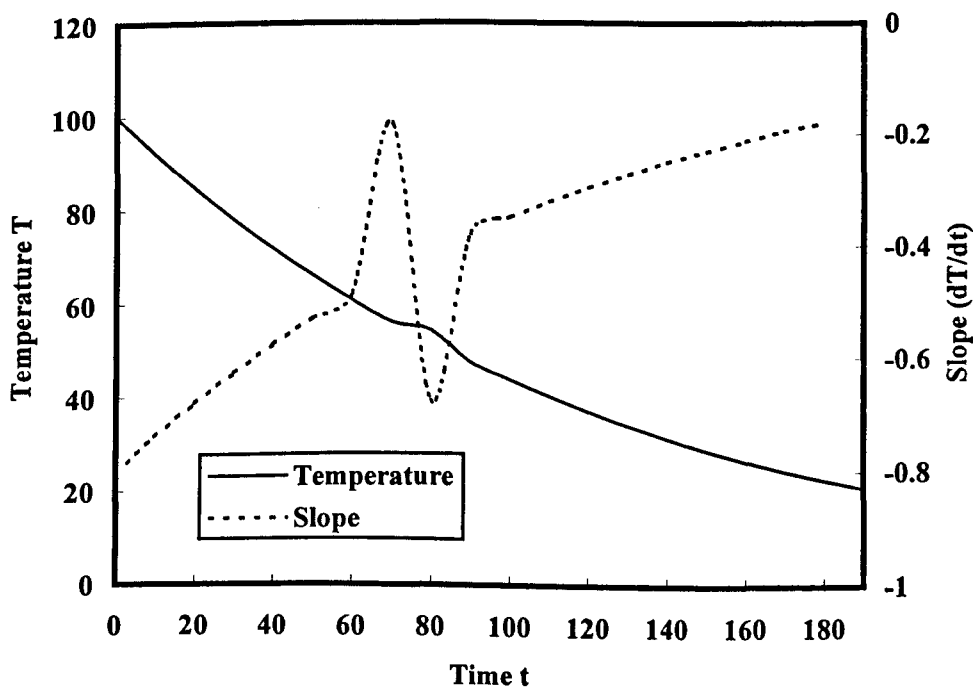


Fig.6.2 (b) : Effect of exothermic phase change during sample cooling

To determine the optimum spectral window for measuring temperature profiles by thermal imaging, the black-body radiation spectrum was calculated for the temperature region of interest and shown in Fig.6.3. Equi-atomic TiNi SMA exhibits a martensitic to austenitic phase change on heating at around 60°C, which is endothermic, and on cooling exhibits an austenitic to martensitic transformation, often with a rhombohedral phase also being observed, which is exothermic and occurs over a temperature range of approximately 70°C - 50°C. At 60°C the black-body spectrum peaks at around 8 μm and predicts a radiated power of approximately 0.5 $\text{W cm}^{-2} \mu\text{m}^{-1}$.

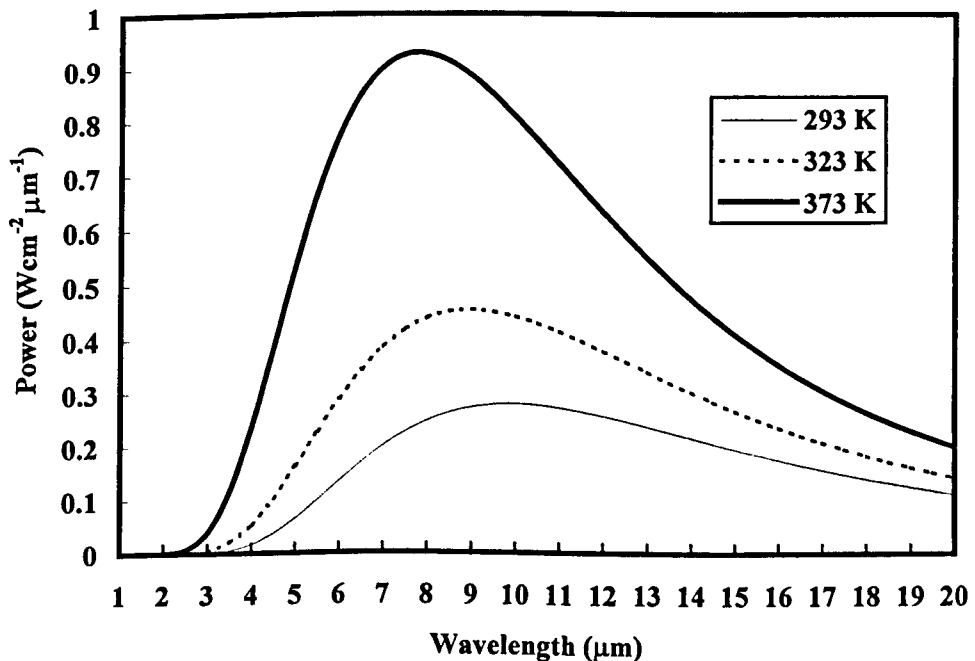


Fig.6.3 : Black-body radiation spectrum for λ from 1 - 20 μm

6.3 Thermal characterisation of TiNi shape memory alloys

6.3.1 Radiative heat transfer coefficient

TiNi samples of area 1.3 cm² and 3.9 cm² deposited on glass substrates were heated using input power ranging from 6 mW to 2.2 W and the maximum temperature rise above ambient determined for each power setting. Under steady-state conditions, and assuming no heat lost by conduction, the radiative heat transfer coefficient for TiNi can be obtained as :

$$K = \frac{P}{A\Delta T} \quad \text{W m}^{-2} \text{ } ^\circ\text{C}^{-1} \quad \text{Equation.6.2}$$

Values of K are plotted versus heating current I in Fig.6.4 (a) and 6.4 (b). The solid lines show the least-squares fit to the data points and are extrapolated to zero heating current. The data is consistent with a value of K of 30 W m⁻² °C⁻¹ for small temperature rises; i.e. where the effect of heat loss by conduction can be assumed to be negligible. A steady increase with temperature in the value of K calculated from Eq.6.2 is to be expected and can be attributed to (a) increasing heat losses by conduction as the temperature rise above ambient increases, and (b) increasing heat losses by radiation as predicted by the black-body spectrum. An apparent increase in K of around 20 W m⁻² °C⁻¹ over the temperature range observed agrees well with calculated heat losses by conduction through the glass substrate assuming a temperature differential of 100 °C and the thermal conductivity of glass to be 1 W m⁻¹ °C⁻¹. Consequently,

for the device scaling calculations presented in section 7.2 of Chapter 7, $K = 30 \text{ W m}^{-2} \text{ }^\circ\text{C}^{-1}$ is taken to be a realistic assumption in evaluating radiative heat losses.

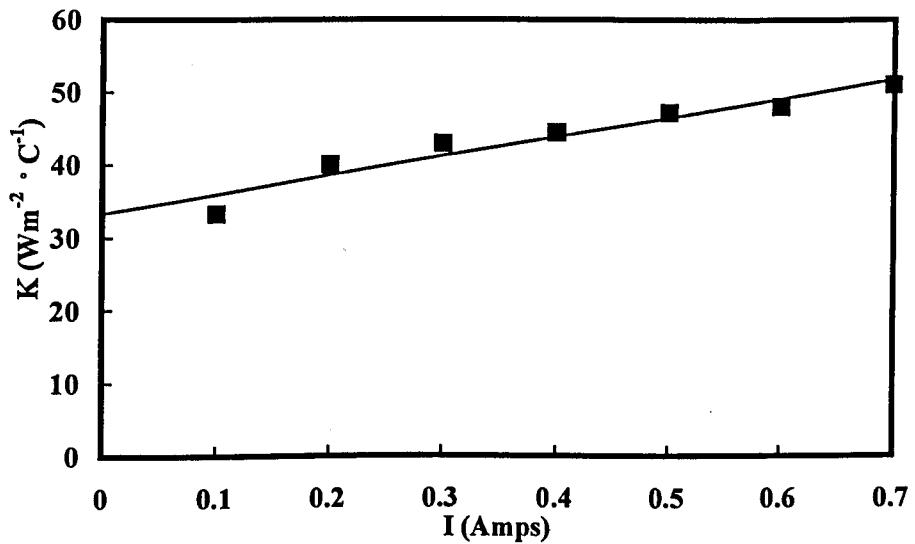


Fig.6.4 (a) : Radiative heat transfer coefficient as a function of heating current for 3.9 cm^2 sample

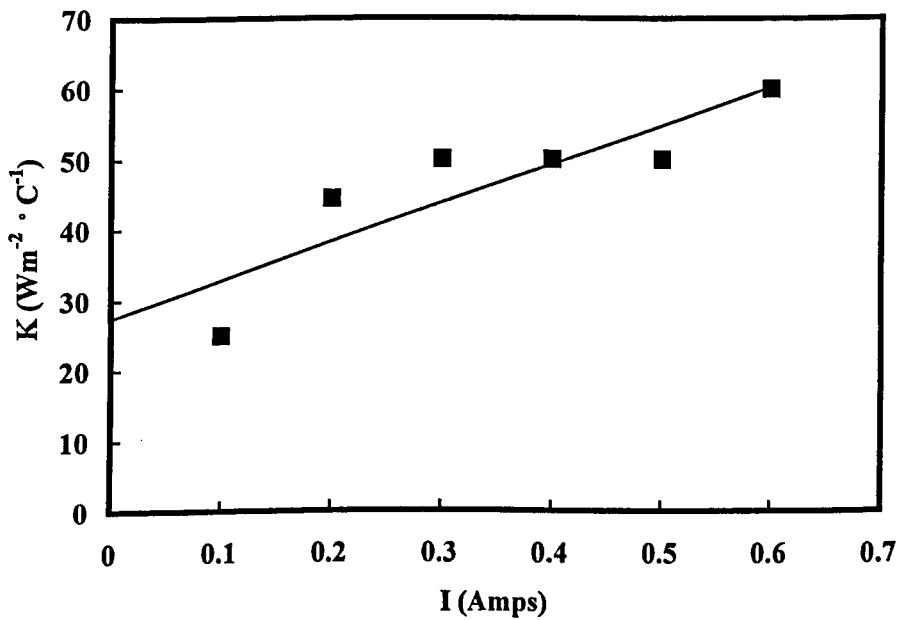


Fig.6.4 (b) : Radiative heat transfer coefficient as a function of heating current for 1.3 cm^2 sample

6.3.2 Temperature - time profiles measurements

A typical temperature versus time profile for the large area samples is shown in Fig.6.5, measured by miniature K-type thermocouple with a resolution of ± 0.1 °C. The expected profile of an endothermic phase transition is seen at approximately 60 °C signalling the austenite start (A_s) temperature. This is consistent with best estimates obtained from resistance versus temperature measurements of thin-film samples prepared under identical conditions². Correction of the observed temperature for radiative heat loss effects as calculated in section 6.3.1 was attempted, but had the effect of increasing the noise level of the data due mainly to the limited resolution of the temperature measurements. In Fig.6.5, error bars associated with the temperature gradient data are calculated from the standard deviation of the points about the baseline gradient and, for clarity, temperature gradients below 40 °C have been scaled by $\times 0.1$.

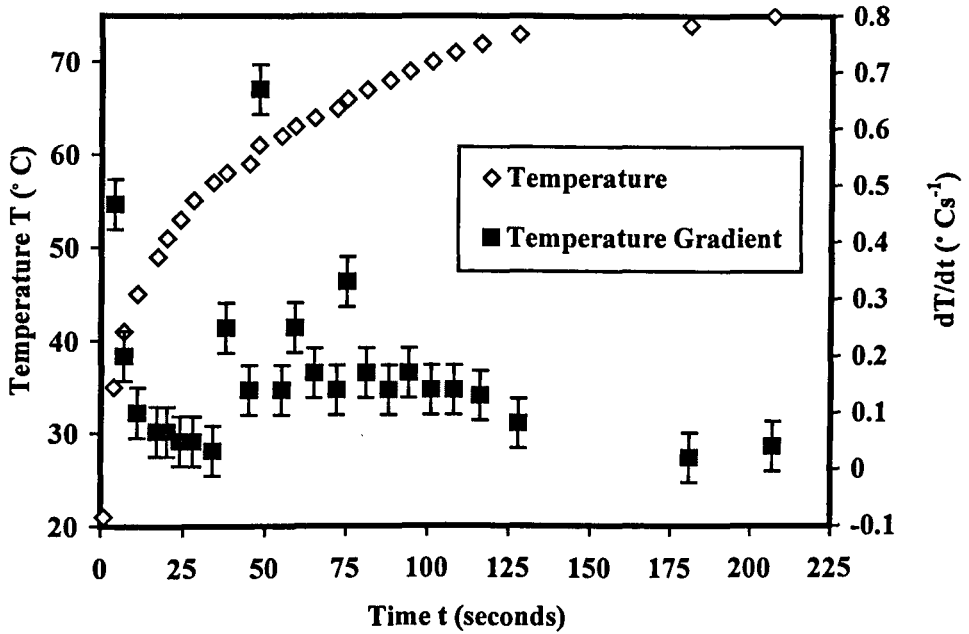


Fig.6.5 : Endothermic phase change during sample heating

6.3.3 Thermal Imaging

Temperature measurements have been made by thermal imaging with an infrared focal plane array camera having a mercury-cadmium-telluride (MCT) imaging array manufactured by Cedip[93]. The MCT array was equipped with a split Stirling cooler which maintained the temperature to within 0.1 °C and operated in the 3 - 5 μm spectral band. Although not precisely matched to the peak of the black-body spectrum at 60 °C, estimates of integrated power radiated at this temperature confirmed that the detector would have ample sensitivity. Image data digitised at 12 bits and 128 × 128 pixels was captured at 1 frame/second during sample heating and cooling. The maximum detector

frame rate for the system is 300 frames/second. The infrared field-of-view of 0.84 mrad corresponded to a spatial resolution of 390 μm with the image forming lens used. Temperature profiles across regions of interest were then derived from the thermal images and displayed as mean or peak temperatures as a function of time.

Fig.6.6 (a) shows a typical temperature versus time plot during sample heating with the gradient of the temperature profile. The profile shows the onset of the endothermic B19' \rightarrow B2 phase transition at approximately 54 $^{\circ}\text{C}$ with completion at approximately 59 $^{\circ}\text{C}$. A typical temperature versus time plot during sample cooling is shown in Fig. 6.6 (b), together with the gradient of the temperature profile. The profile shows the onset of the exothermic B2 \rightarrow B19' phase transition at approximately 67 $^{\circ}\text{C}$ with completion at approximately 54 $^{\circ}\text{C}$.

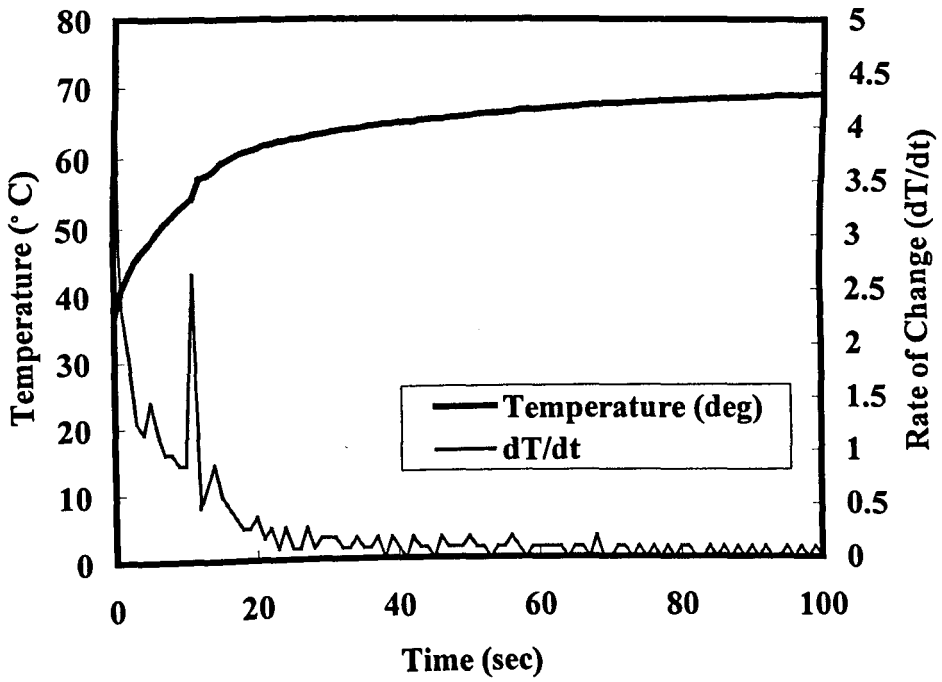


Fig.6.6 (a) : Endothermic phase change during sample heating

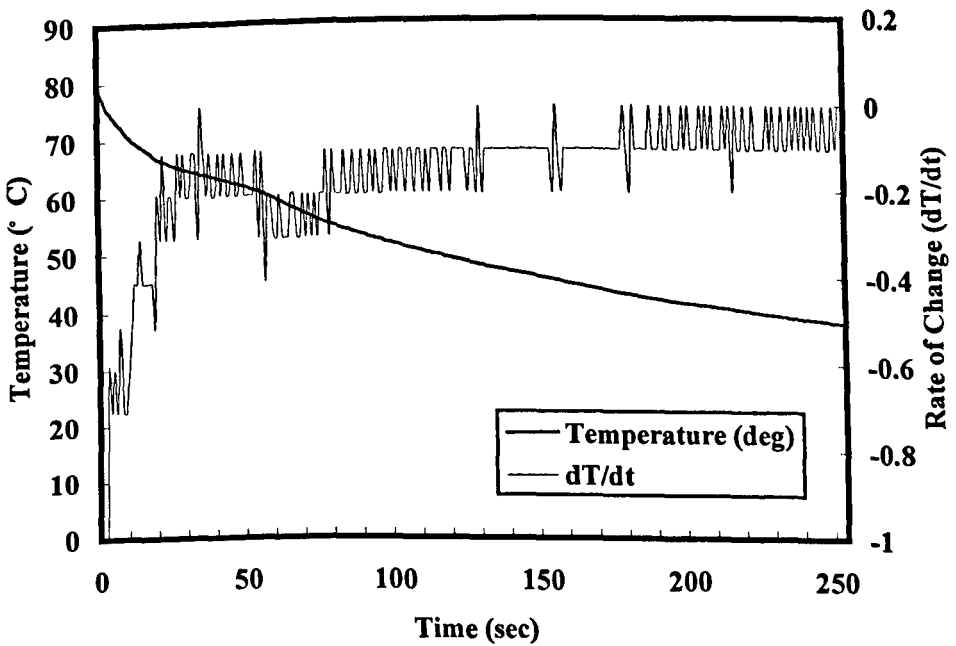
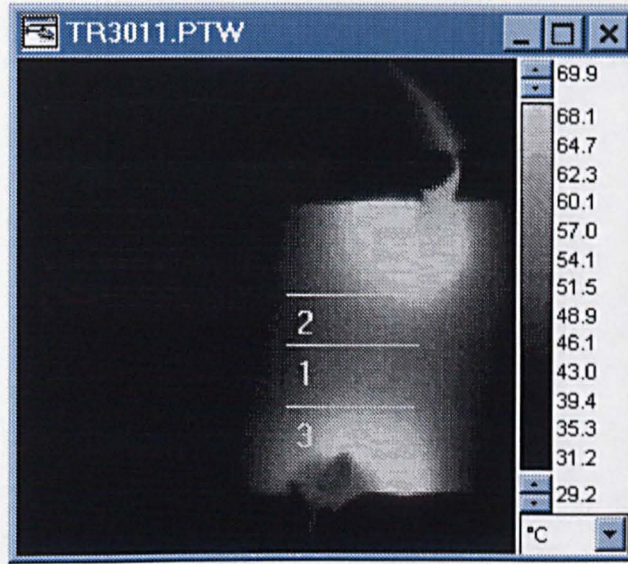


Fig.6.6 (b) : Exothermic phase change during sample cooling

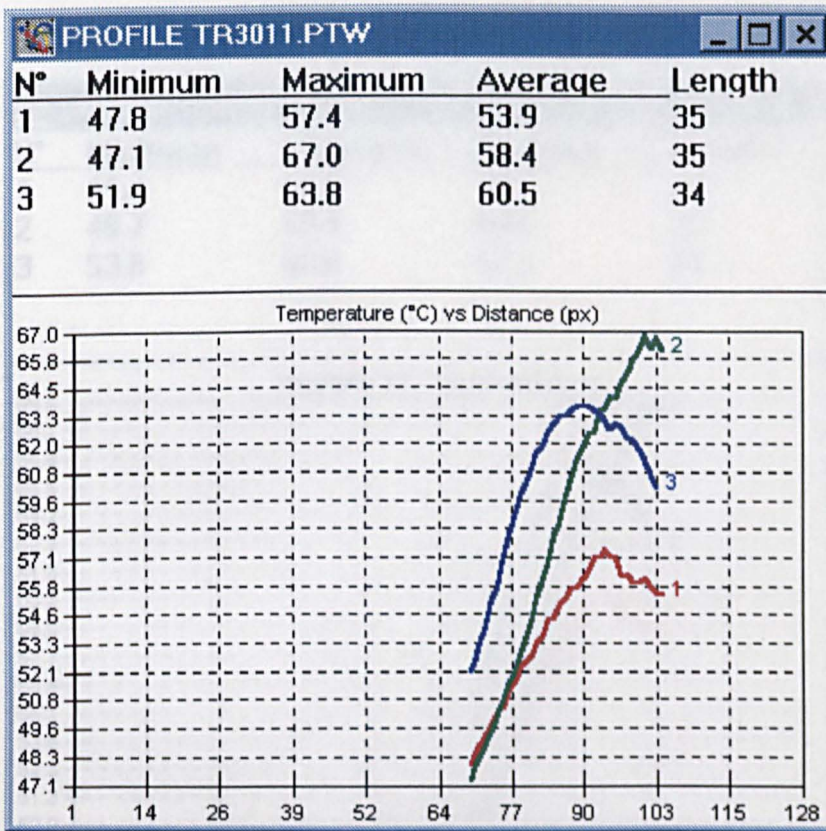
Fig. 6.7, Fig. 6.8 and Fig. 6.9 show thermal images obtained between 11 and 13 sec during heating. Fig.6.7 (a) shows the thermal image and Fig.6.7 (b) shows temperature profiles across user-specified lines in the image. Average, maximum and minimum temperatures are shown across lines 1, 2 and 3 appearing on the image in Fig. 6.7. Average temperatures differ by a few degrees between the locations selected, with higher temperatures recorded near the points of electrical contact.

In the plot of average temperature versus time, which is shown in Fig.6.10, rate of change of temperature dT/dt increases significantly between 58 °C and 60 °C and is plotted in the lower curves for each of the selected lines in the image. The temperature at which dT/dt increases shows excellent agreement with the austenite start temperature (A_s) as determined by the resistance measurements described in section 5.5.2. Also, for the corresponding minimum and maximum temperatures, which are shown in Fig.6.11 and Fig.6.12, very similar rates of change of temperature were also observed in the 10 – 12 second time interval.

With reference to Fig.6.10, Fig.6.11 and Fig.6.12 the rates of change of temperature dT/dt increase by around a factor of 5 at temperatures that are in broad agreement with A_s . According to Dautovich *et al*[94], the specific heat for bulk TiNi decreases by approximately a factor of 5 on heating through A_s . The data in Fig.6.10, Fig.6.11 and Fig.6.12, therefore shows the expected agreement with changes in specific heat.

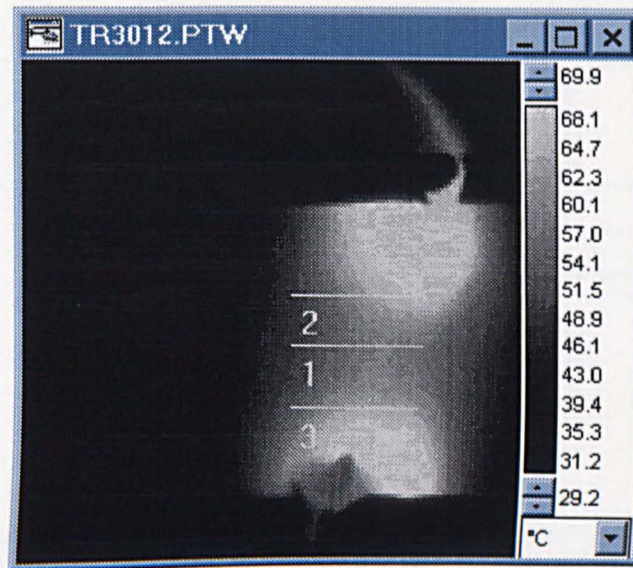


(a)

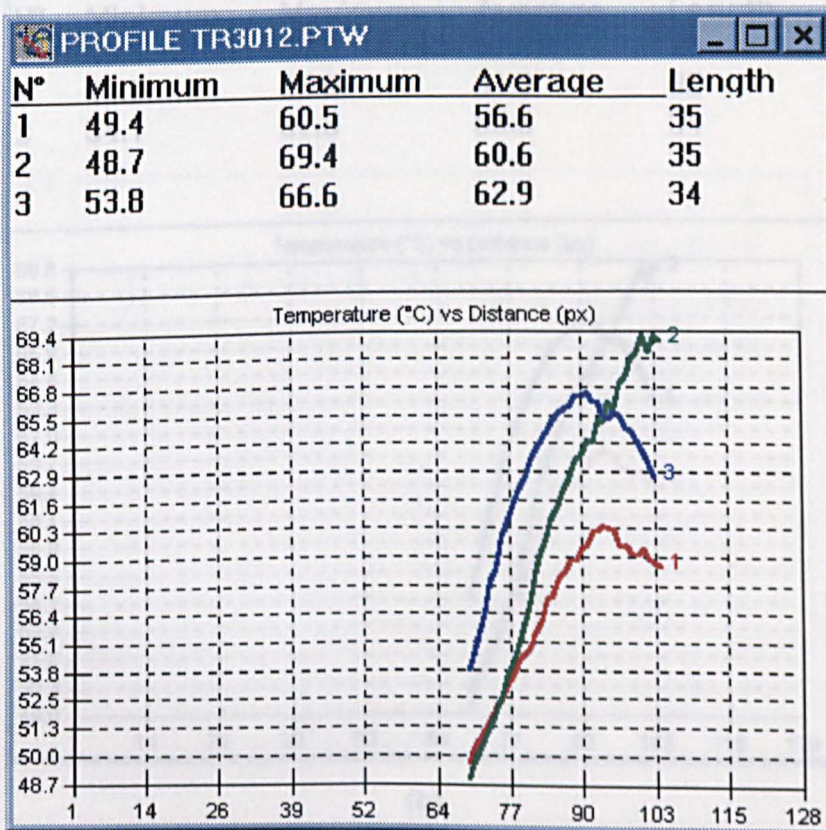


(b)

Fig. 6.7 : Thermal image by non contact at 11 sec for heating
((a) thermal image (b) temperature at lines)

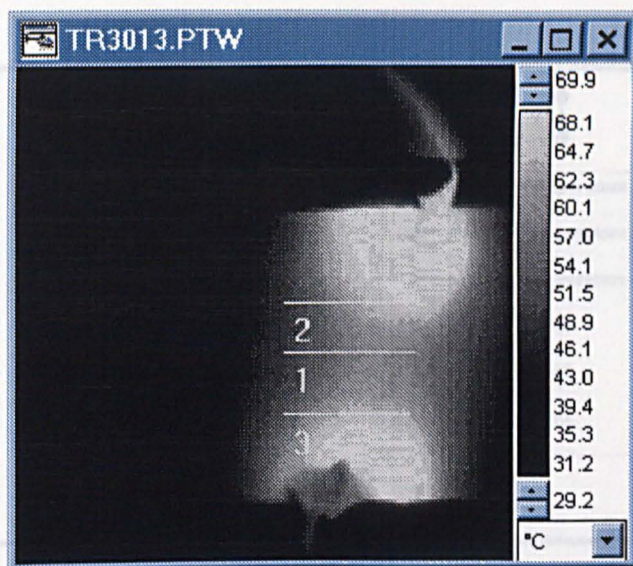


(a)

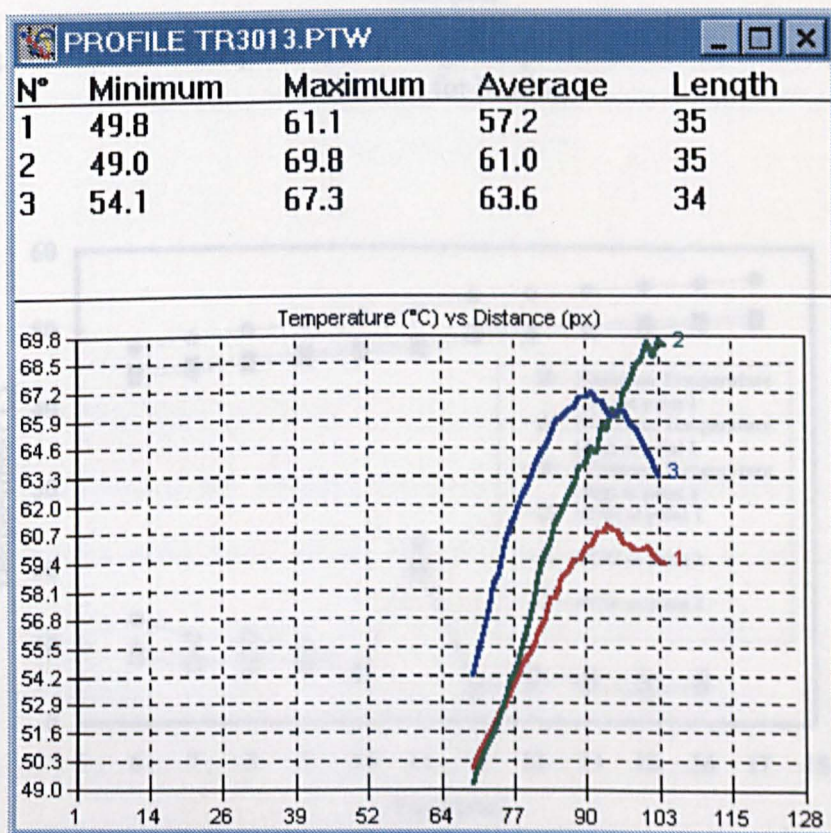


(b)

Fig. 6.8 : Thermal image by non contact at 12 sec for heating
((a) thermal image (b) temperature at lines)



(a)



(b)

Fig. 6.9 : Thermal image by non contact at 13 sec for heating ((a) thermal image (b) temperature at lines)

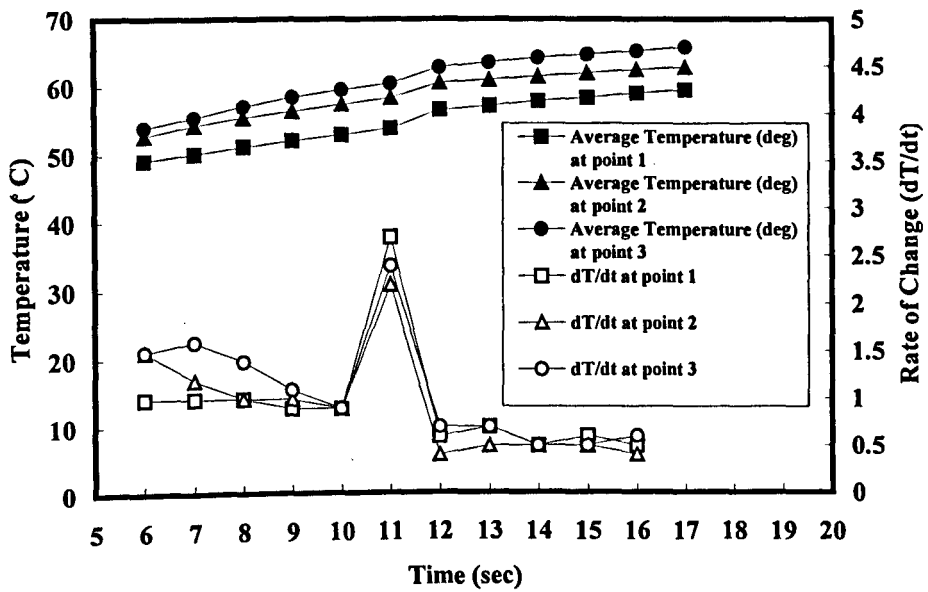


Fig. 6.10 : Relationship between average temperature and rate of change, with the time for heating

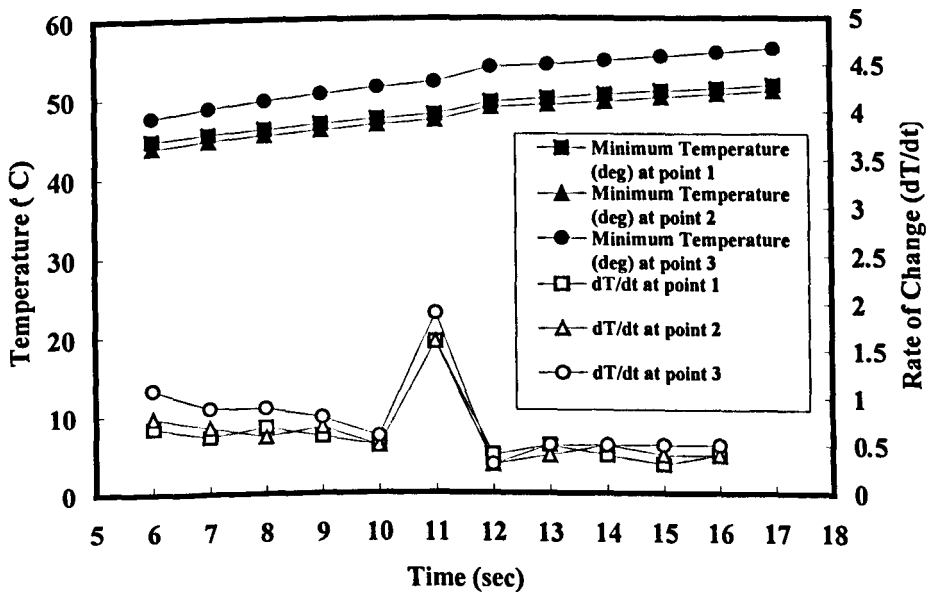


Fig. 6.11 : Relationship between minimum temperature and rate of change, with the time for heating

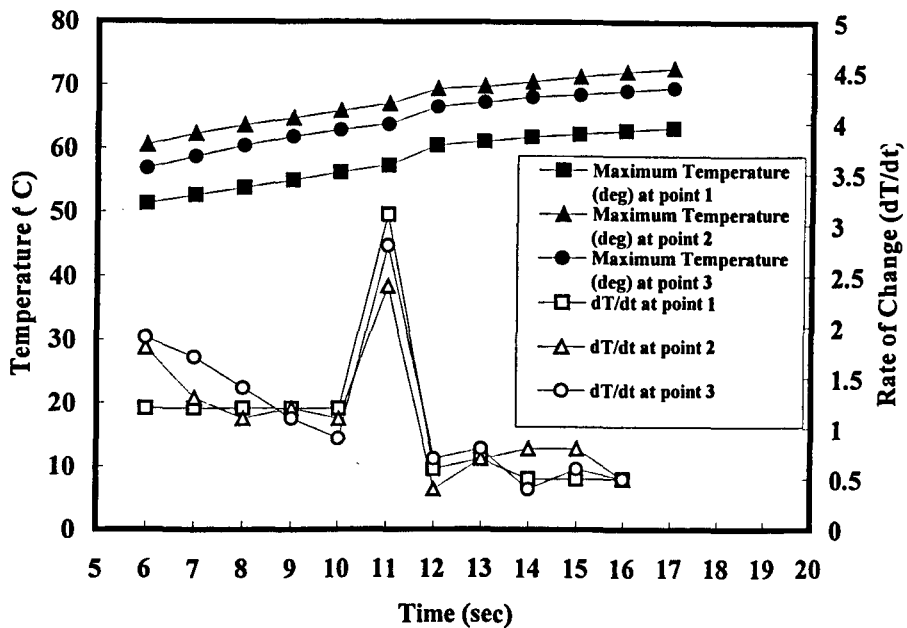


Fig. 6.12 : Relationship between maximum temperature and rate of change, with the time for heating

6.5 Summary

TiNi SMA thin films grown by an ion beam sputter deposition process have been characterised by thermal measurement. Thermal imaging using an infrared focal plane array camera has also been described. A simple model describing electrical heating of thin film structures is used to interpret temperature-time profiles and identify the material phase transitions characterising the shape memory effect. The austenite transformation temperature of TiNi SMA films was observed by non-contact measurements.

An analysis of thermal parameters allows effects of dimensional scaling to be predicted. The analysis indicates that SMA thin films appear to offer distinct

advantages over alternative mechanisms for implementing integrated micropositioning and microactuator devices. In the next chapter, heating and cooling speed for microactuators will be discussed, and a FIB (focused ion beam) trepanning technique having potential for fabrication of microactuator devices will also be described.

7 TINI MICROACTUATORS : TECHNOLOGY, FURTHER WORK AND CONCLUSIONS

7 TiNi microactuators : technology, further work and conclusions

7.1 Introduction

In this chapter, dimensional scaling implications for achievable heating and cooling rates of TiNi microactuators will be considered. Also in this chapter, recommendations for future work will be described ; namely for the fabrication and assembly of complex actuator, micro parts, which require dimensional tolerances, alignment and placement on the nanometer scale, will be described. For this purpose, a focused ion beam trepanning technique will be evaluated. In addition, future further work and the conclusions of this thesis will be presented in the final section.

7.2 Device scaling

7.2.1 Introduction

A prime concern in considering the integration of SMA microactuators in MEMS and micro optical electro mechanical systems (MOEMS) devices is the area, time and power trade-offs in scaling structures utilising the shape memory effect to micrometre dimensions. For example, area considerations will affect radiative heat loss (and heat loss by conduction if the structure is bonded to a substrate as opposed to free-standing) which in turn will affect speed of response. Speed of response will be dictated by cooling time, which will be dependent on the surface area to volume ratio and for a given area will determine the maximum thickness of the structure. Furthermore, maximum

permissible power dissipation will determine heating rate and so on.

7.2.2 Effect of scaling

Fig.7.1 illustrates the effect of scaling the lateral dimensions (with equal length and width) of the structure and has been calculated for uniform thickness of 5 μm , with power input P as parameter. As described in chapter 6, for the device scaling calculations, the radiative heat loss coefficient is estimated for the purpose of evaluating radiative heat losses. The vertical axis shows maximum rate of temperature increase assuming only radiative heat losses and with $K = 30 \text{ W m}^{-2} \text{ }^\circ\text{C}^{-1}$. For instance, a 100 μm structure powered by drive circuitry delivering 10 mW would experience an initial temperature rise of $\sim 10^5 \text{ }^\circ\text{C s}^{-1}$ and a 10 μm structure powered by drive circuitry delivering 1 mW would experience an initial temperature rise of $\sim 10^6 \text{ }^\circ\text{C s}^{-1}$.

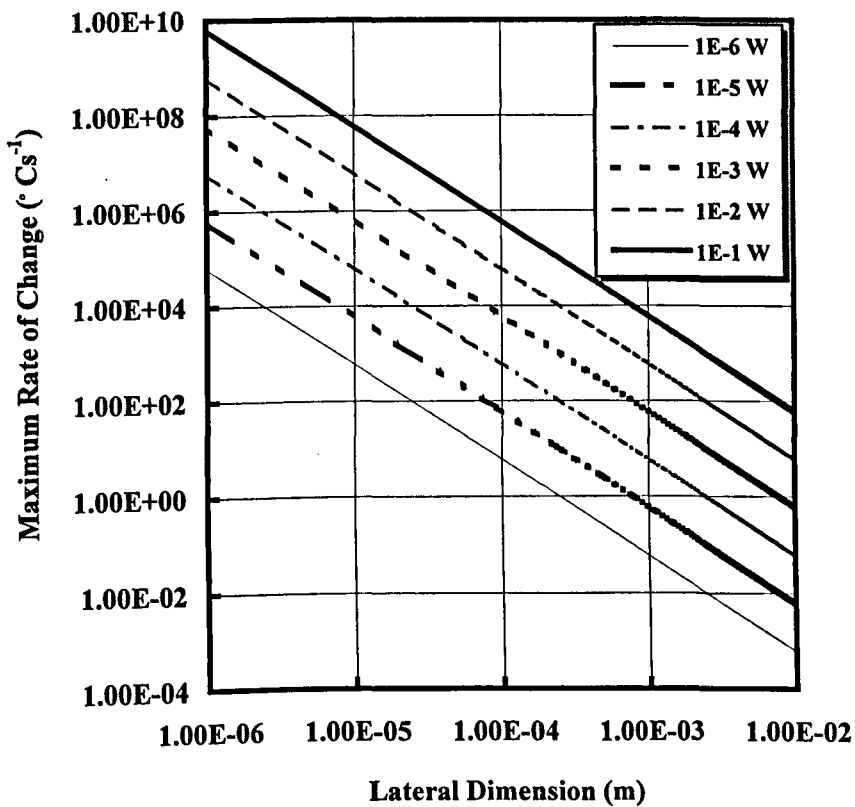


Fig.7.1 : Relationship between device lateral dimension, heating power and maximum heating rate[95]

The limitations on high-speed operation of SMA microactuators, however, are determined by the rate of cooling which is a function of the surface area to volume ratio (i.e. scales with device thickness) and is calculated, assuming no heat loss by conduction, according to :

$$\frac{d(\Delta T)}{dt} = -\frac{KA\Delta T}{mC_p} \quad \text{°C s}^{-1} \quad \text{Equation. 7.1}$$

The value C_p for TiNi[92] is assumed to be $490 \text{ J kg}^{-1} \text{ °C}^{-1}$. The parameters appearing on the plot of Fig.7.2 relate to a structure having lateral dimension

(with length equal to width) of $100\ \mu\text{m}$ at a temperature ΔT above ambient of $50\ ^\circ\text{C}$ and shows the effect of varying the thickness of the structure on cooling rate. The magnitude of the maximum cooling rate is shown in $^\circ\text{C s}^{-1}$ on the right-hand scale. In addition the left vertical axis shows values for $M \times C_p$ and $K A \Delta T$ in units of $\text{J } ^\circ\text{C}^{-1}$ and Watts respectively. Over a fixed area, heat loss by radiation is constant and heat capacity is inversely proportion to thickness. For instance, cooling rates for structures of thickness $10\ \mu\text{m}$ are approximately $50\ ^\circ\text{C s}^{-1}$ while those for $1\ \mu\text{m}$ thickness are approximately $500\ ^\circ\text{C s}^{-1}$.

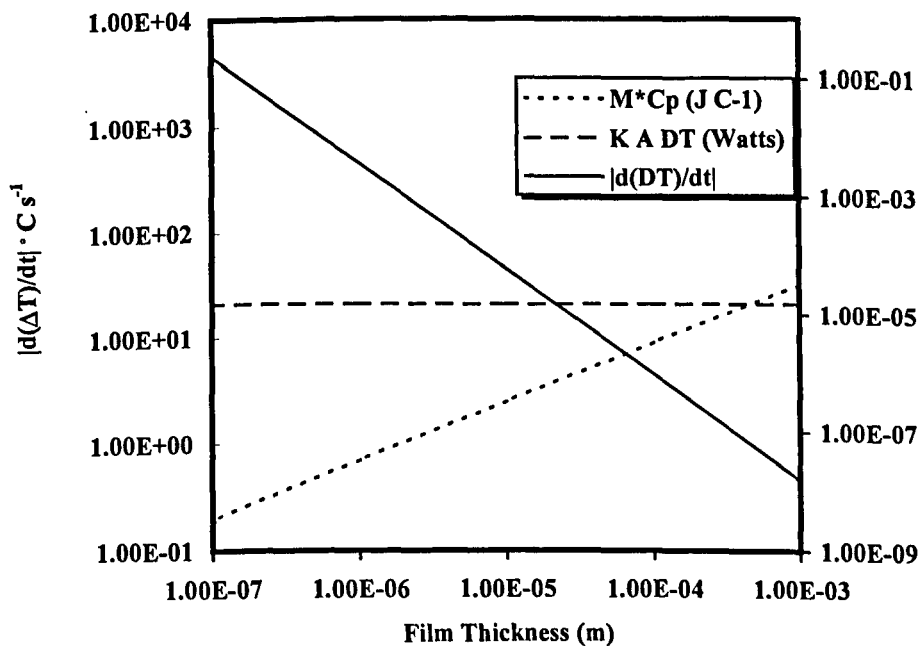


Fig.7.2 : Relationship between film thickness and maximum cooling rate[95]

7.2.3 Summary

The effects of scaling characteristic dimensions for TiNi SMA thin films, with input power as a parameter, on the heating and cooling rates of those films have been investigated. The cooling rates of TiNi SMA films are dependent only on the film thickness. In the simple model adopted, for a decrease in film thickness of a factor of 10, the cooling rate increases approximately a factor of 10. Cooling rate is independent of the area of the structure and depends only on thickness, which imposes an upper frequency limit on the operation of microactuators employing SMA devices in the absence of assisted or forced cooling.

7.3 Focused ion beam trepanning

7.3.1 Introduction

SMA thin films for microdevices and microactuators can call for very complicated geometries[3]. In the fabrication of microactuators, micromachining techniques ranging from chemical etching to cold rolling have been investigated to produce structures with dimensions down to a few hundred of micrometres[91]. However, these sizes may have to be reduced still further for applications in the field of MEMS. Micro-components with typical dimensions in the 1 - 100 μm range and having dimensional tolerances of order 0.1 μm have been called for. Examples include ultra-thin plates, beams, shafts and cantilevers. In this section, a novel combination of micromachining operations to produce self supporting nickel, stainless steel and mu-metal

plates with thicknesses down to 1 μm has been used for fabricating more complex micro-parts such as disks, gears and cogs by direct writing using focused ion beam (FIB) trepanning with a resolution of 50 nm, as shown schematically in Fig.7.3.

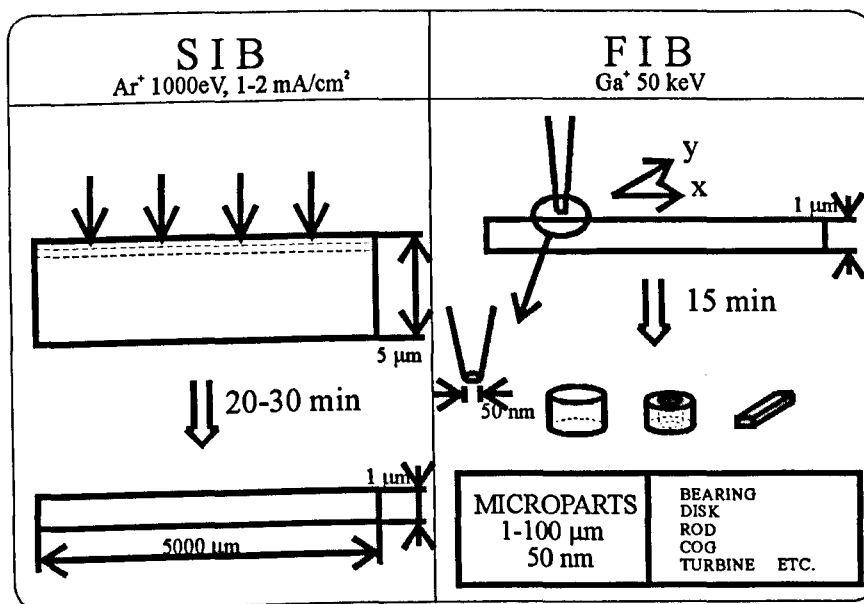


Fig.7.3 : Micromachining strategy

The samples were inspected in situ during microfabrication by using the inherent scanning ion microscope (SIM) capabilities, using secondary electrons or ions. This can also be used for inspection during micro-part assembly. The FIB system allows imaging at a resolution comparable with the beam diameter. Off-line inspection at higher resolution was achieved with a conventional scanning electron microscope (SEM). A further objective of the investigation was to explore methods of forming rudimentary 3-D structures.

7.3.2 Focused ion beams

Fig.7.4 shows a schematic diagram of a focused ion beam column utilising a LMIS (liquid metal ion source). Focused ion beams have been drawn from liquid metal ion sources, such as Ga, In and Au-Si. The apparatus can generate ion beams of diameter 50 nm – 50 μm with current densities of 1 - 10 A cm^{-2} and beam energies of < 40 keV. The pressure in the ground target chamber should be maintained below 10^{-8} mbar.

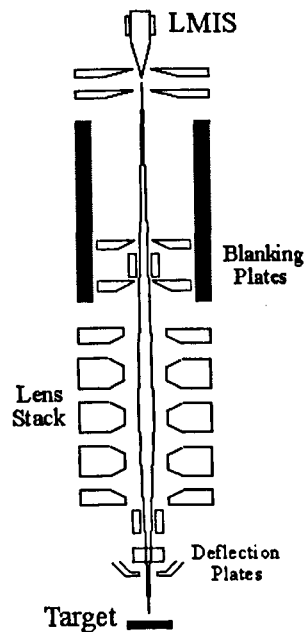


Fig.7.4 : Schematic of FIB column

7.3.3 Production of micro-parts by FIB

High aspect ratio micro-parts have been fabricated by process such as *Lithographie Galvanoformung Abformung* (LIGA). However, LIGA required an injection moulding step which is problematical for numerous materials of interest in MEMS, specifically SMA materials.

An alternative “direct-write” technique is therefore investigated here. Initial attempts to fabricate ultra-thin ($<1 \mu\text{m}$) self-supporting metallic plates by showered ion beam milling met with only limited success due to difficulties in controlling the process. Fig.7.5 shows the geometrical setup for the production of micropart blanks. The currents I_1 and I_2 were measured with $I_1 \sim 1\text{mA}$ and current I_2 detected on mill-through with $0.01 \mu\text{A}$ resolution. Mill-through times were found to vary widely under nominally identical processing condition. Consequently, it was essential to thoroughly investigate how the current incident on the sample varied with the source and vacuum chamber operating conditions. As discussed in Chapter 3, the effect of a variation in current density, the dependency of the beam profile on the total extraction current and the effect of extraction grid geometry on the current density in the milling process were studied. These factors are very important for ultra precision control in milling of thin foils in general, and will be applied in future work for preparation of SMA ultra thin foils. For instance, in SMA ultra thin foils, the dependence of phase transformation temperatures on composition and grain size are of considerable interest.

Foils of aluminium, nickel, stainless steel, and mu-metal with nominal thicknesses in the range $5 - 25 \mu\text{m}$ (\pm approx 10 %) were obtained from Goodfellow, Cambridge[66]. They were used as the starting point in the preparation of micro-part blanks in the form of ultra-thin, self-supporting plates with thicknesses of $\sim 1 \mu\text{m}$. The samples were generally of good surface finish, as observed by optical microscopy prior to SIB micromachining. Trials using

aluminium produced a mill-through time of 33 ± 6 mins for $5 \mu\text{m}$ samples and 40 ± 6 mins for $6 \mu\text{m}$ samples when bombarded with of 1000 eV Ar^+ ions in a 25 mA beam with a source to sample separation of 5 cm . Both sets of data were consistent with a milling rate of $0.15 \mu\text{m min}^{-1}$. Similar results were obtained for $9 \mu\text{m}$ and $12.5 \mu\text{m}$ thickness of aluminium and various thicknesses of nickel, stainless steel and mu-metal. In all cases, end-point detection of mill-through was by registering an increase of $0.01 \mu\text{A}$ in the Faraday cup current I_2 above the background noise level of $0.01 \mu\text{A}$.

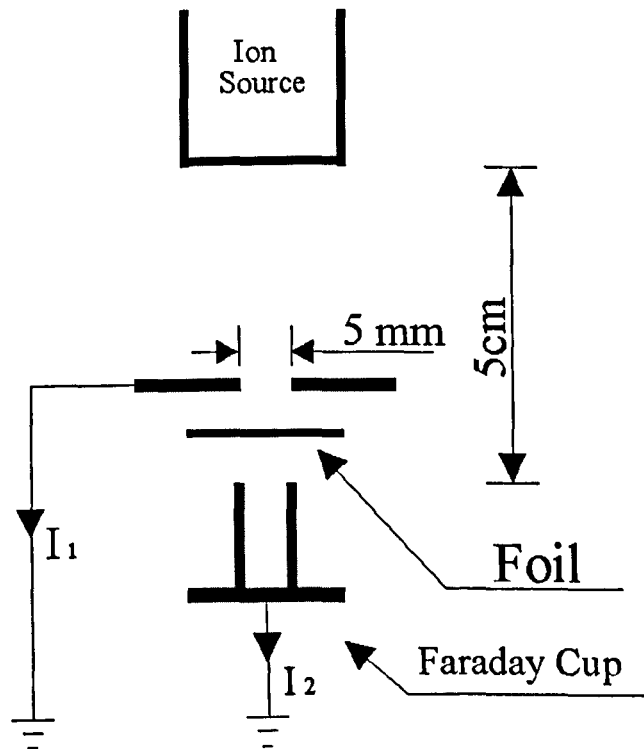


Fig.7.5 : Geometrical setup for milling of micro-parts blank

As described above, SIB micromachining or sputter deposition offers material removal rates or deposition rates of order $0.1 \mu\text{m mA}^{-1} \text{ cm}^2 \text{ min}^{-1}$. In comparison, FIB micromachining gives selective area material removal over

areas comparable with the probe size at rates of order $1 \mu\text{m}^3 \text{ nA}^{-1} \text{ sec}^{-1}$. (Selective area deposition by FIB is also possible, generally by decomposition of a gas phase precursor material, with similar deposition rates). Control of material removal and deposition with nanometer precision in both lateral direction and depth can thus be achieved.

FIB micromachining was carried out both at the University of Warwick and at the Central Microstructure Facility of the Rutherford Appleton Laboratory. Designs were produced by commercially available CAD software. An example is the gearwheel shown in Fig.7.6. Designs could be scaled prior to FIB micromachining provided that all pixels to be written by FIB were defined in the bit-map image file. The boundaries of the dark regions were trepanned repetitively under computer control until the sample was penetrated. Support struts were left at the 0° , 135° and 225° positions in order to hold the microstructure until it was ready for release. On locating the structure relative to an assembly directly below, controlled FIB milling of the support struts allows the micro-part to drop into position. A nickel component produced from the gearwheel design is shown at a different orientation and just prior to release in the SEM micrograph (Fig.7.7). The scale bar is $10 \mu\text{m}$ and the gearwheel diameter is approximately $8 \mu\text{m}$.

7.4 Future work

7.4.1 Out-of-plane 3-D microactuators

3-D microfabrication techniques such as the lock-and-key process in ultra-thin plates [7] and the "reprogramming" technique [8] for remembering shape for microactuators are limited relative to the technique described above involving the use of a support stress in cyclic fashion to ensure that the structure is always in the desired shape between a single point of attachment, the microactuator is capable of being in an orientation and shape that is different from the original design.

Fig.7.6 : CAD schematic of gearwheel

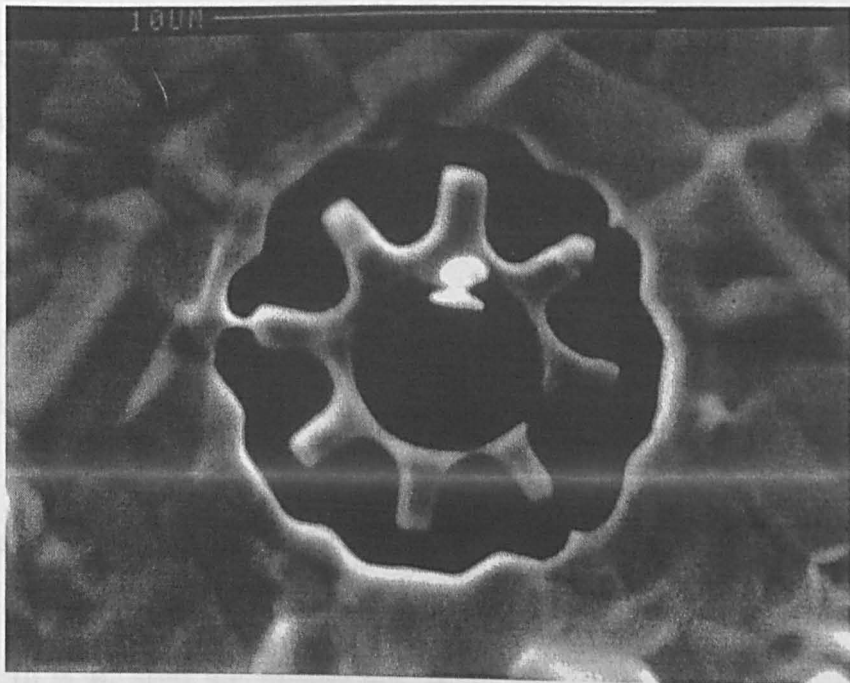


Fig.7.7 : FIB micromachined gearwheel

7.4 Future work

7.4.1 Out-of-plane 3-D microstructures

3-D microfabrication was investigated by exploiting the locked-in stress in ultra-thin plates. The technique holds promise for “programming” the remembered shape for SMA microdevices. The controlled release technique described above involves gradually milling through the support struts in cyclic fashion to ensure that the structure drops free. If the milling sequence leaves a *single* point of attachment, the structure can “pop-up” out of plane at an orientation and angle determined by the geometry of the support strut.

The sequence is illustrated schematically in Fig.7.8. Uniform milling around the periphery of the disk occurs in steps 1 and 2. In step 3 there is less than the full 360 ° trepanning and this leads to the disk tilting out of plane in step 4 when the right hand support strut is removed. Fig.7.9 shows how the angle of tilt can be controlled by the aspect ratio of a notch along one side of a rectangular flap. An aspect ratio < 1 constrains the angle of tilt to $< 90^\circ$, an aspect ratio equal to 1 gives a tilt of 90° and an aspect ratio > 1 allows a tilt $> 90^\circ$. It is proposed that such structures could be *microwelded* in position by sputter deposition and this is the subject of further investigation.

Fig.7.10 is an SEM micrograph that shows an example of the phenomenon. The scale bar is 50 μm and the disk diameter is approximately 10 μm . Two disks have been cut through and allowed to drop; two have been “hinged” at

different orientations and allowed to pop out of plane at specific angles, in this instance, of around 70 °. An artifact strategically placed in the vicinity of these structures aids rapid detection by the SEM!

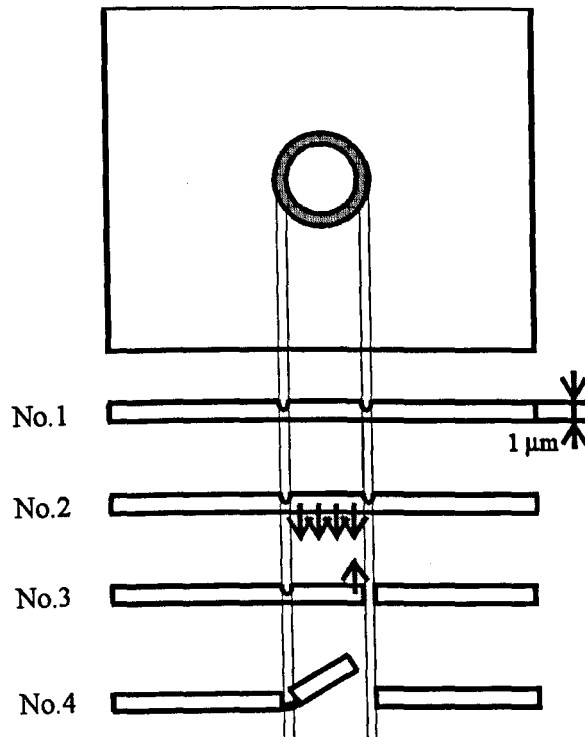
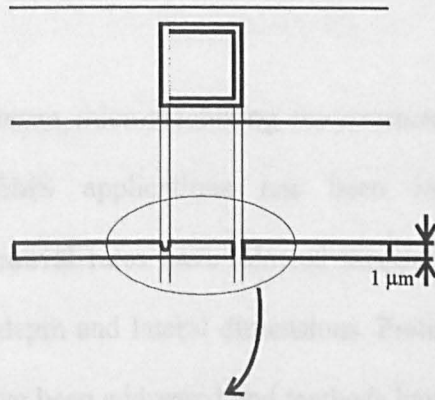


Fig.7.8 : FIB trepanning

7.4.2 Summary

The feasibility of ion beam sputtering for the fabrication of microactuators in different applications has been investigated. Highly controllable material removal rates have been achieved. The scale precision in both depth and lateral dimensions. Preliminary studies of 3-D microfabrication techniques have been investigated for realizing 3-D structures. Approaches to microfabrication techniques for realizing 3-D structures help for further investigations.



< 90 (deg)	90 (deg)	> 90 (deg)

Fig.7.9 : Control of the "pop-up" process

7.5 Conclusions

This thesis has been devoted to investigating the feasibility of ion beam sputtering for the fabrication of microactuators in different applications. The main objective of this work was to study the possibility of realizing 3-D structures. The main objective of this work was to study the possibility of realizing 3-D structures. The main objective of this work was to study the possibility of realizing 3-D structures.

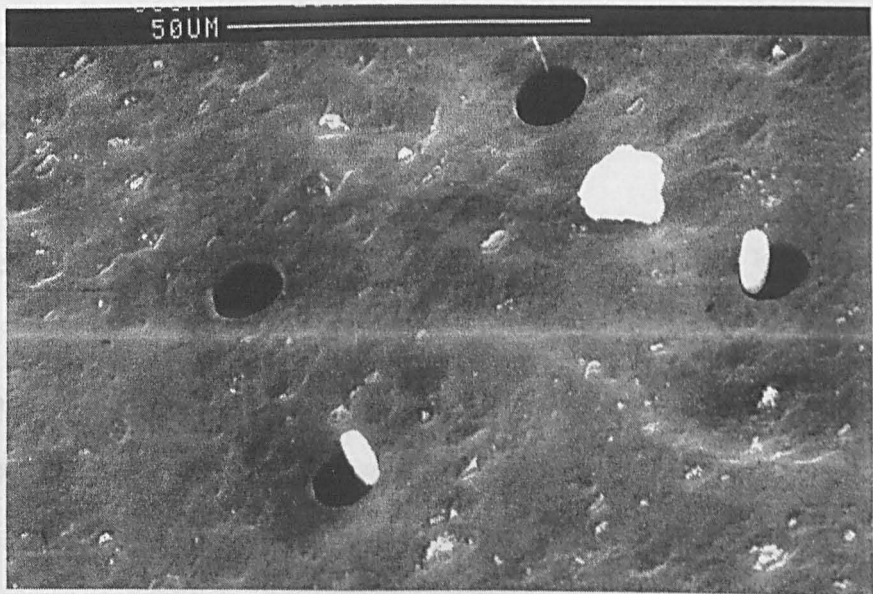


Fig.7.10 : SEM of 3-D out-of plane structures

7.4.2 Summary

The feasibility of ion beam micromachining microstructures for TiNi SMA microactuators in MEMS applications has been investigated. Highly controllable material removal rates have allowed fabrication with nanometre scale precision in both depth and lateral dimensions. Preliminary problems of 3-D microfabrication have been addressed and methods have been proposed for realising 3-D structures by exploiting stresses in ultra-thin self-supporting foils. Approaches to microstructure assembly have been presented which form the basis for further investigations.

7.5 Conclusions

This thesis has been devoted to fabricating TiNi shape memory alloy thin films by an IBSD method. The main achievements of the work have been the growth of TiNi SMA thin films on unheated substrates using non-alloyed targets by IBSD. Potential applications in MEMS have been emphasised throughout.

As described in this thesis, TiNi thin films have been deposited by IBSD and were characterised by X-ray reflectometry, electrical resistivity and resistance measurements. In the characterisation of TiNi SMA films by X-ray reflectometry, the composition was confirmed as being near equi-atomic. Transformation temperature of TiNi SMA films namely A_s , A_p , M_s and R-phase, were estimated as 60 °C, 85 °C, 50 °C and 62 °C, respectively, and electrical resistivity was around 1 $\mu\Omega.m$. Those values were in excellent good agreement

with values quoted for equi-atomic TiNi in the literature.

The chamber pressure during IBSD has also been discussed, in comparison with DC and RF, and magnetron sputtering in Chapter 2 and Chapter 5. Incorporation of impurities during film grown are shown in IBSD, and the density of TiNi films must be low from X-ray reflectometry data. In this thesis, the TiNi films were deposited on to unheated substrates. In conventional deposition methods such as DC and RF, and magnetron sputtering, as-deposited films are amorphous if the substrate temperature is kept below 200 °C, and annealing is needed to produce crystallisation after deposition. Furthermore, the transformation temperature of a TiNi thin film changes by 100 °C per percent change of the composition. In this work, the TiNi composition was controlled by the relative areas of Ti and Ni in segmented non-alloyed targets. Eight sectored Ti/Ni targets were found to be appropriate to provide adequate compositional control. Free-standing TiNi SMA thin films have been investigated for use as microactuators, however, such films are very difficult to anneal and exhibit residual strain. One approach to producing free-standing films would be to deposit TiNi onto copper or Kapton as a sacrificial substrate by IBSD in polycrystalline or single crystal form and then to remove the substrate by chemical etching.

In chapter 6, an alternative strategy to DSC measurements, that of maintaining constant heating power and measuring the rate of change of temperature corresponding to the specific heat capacity change was adopted. Non-contact

measurements were made, by infrared focal plane array camera thermal imaging. Thermal imaging could readily spatially resolve the phase transitions characterising the shape memory effect at different places.

In Chapter 7, the scaling of TiNi shape memory alloy structures for microactuator devices were described. Speed of response for such shape memory alloy structures was then calculated. Cooling rates of TiNi SMA films of 1 μm thickness having lateral dimension (with length equal to width) of 100 μm by radiative heat losses were approximately 500 $^{\circ}\text{C s}^{-1}$. Productions of micro-parts by focused ion beam (FIB) trepanning techniques was then introduced, and implication for SMA microdevices explored. This technique can be employed for fabrication of complex TiNi structures as an alternative to photolithography or LIGA processes. TiNi SMA thin films would be compatible with integrated CMOS (Complementary Metal-Oxide Silicon) due to the low temperature deposition conditions.

References

- 1 H. Fujita : Microactuators and micromachines, Proceedings of the IEEE, Vol.86, No.8, p.1721-1732(1998)
- 2 C.T.-C. Nguyen, L.P.R.Katehi and G.M.Rebeiz : Micromachined devices for wireless communications, Proceedings of the IEEE, Vol.86, No.8, p.1756-1768(1998)
- 3 M. Kohl, K. D. Skrobanek and S. Miyazaki : Development of stress-optimised shape memory microvalves, Sensor and actuators, A72, p.243-259(1999)
- 4 K. Wasa and S. Hayakawa : Handbook of sputter deposition technology, Noyes publications, p.20(1992)
- 5 K. Ikuta : The application of Micro/Miniature mechatronics to medical robots, Proc. of IEEE international workshop on Intelligent Robots and Systems, Tokyo, p.9-14 (1988)
- 6 W. L. Benard, H. Kahn, A. H. Heuer and M. A. Huff : Thin Film Shape-Memory Alloy Actuated Micropumps, J. of Microelectromechanical Systems, Vol.7, 2, p.245-251(1998)
- 7 K. Kuribayashi, S. Shimizu, T. Nishinohara and T. Taniguchi : Trial Fabrication of Micro Sized Arm Using Reversible TiNi Alloy Thin Film Actuators, Proc. Of the IEEE/RSJ International Conference on Intelligent Robots and Systems, Japan, p.1697-1702 (1993)
- 8 T. Tadaki, K. Otsuka, K. Shimizu : Shape memory alloys, Ann. Rev. Mater. Sci., 18, p.25-45 (1988)
- 9 R. H. Wolfe and A. H. Heuer : TiNi(shape memory) films on silicon for MEMS applications, Journal of Microelectromechanical systems, 4, p.206-212 (1995)

- 10 M. C. Montesi, B. Martini, A. Pellegrinetti, P. Dario, L. Lencioni and A. Montano : An SMA-based flexible active endoscope for minimal invasive surgery, *J. Micromech. Microeng.*, 5, p.180-182 (1995)
- 11 K. Kuribarashi, T. Taniguchi, M. Yoshitake and S. Ogawa : Micron sized arm using reversible TiNi alloy thin film actuators, *Mater. Res. Soc. Symp. Proc.*, 276, p.167-175 (1992)
- 12 L. M Schetky. : Shape memory alloys, *Scientific American*, Nov. Ed., p.68-76 (1979)
- 13 Y. Sekiguchi et al : Test-production of TiNi shape memory alloy thin film by vacuum deposition, *Proc. of 32nd Material Society Annual Conference*, p.65 (1983) (in Japanese)
- 14 A. D. Johnson : Vacuum-deposited TiNi shape memory film : characterization and applications in microdevices, *J.Micromech. Microeng.*, 1, p.34-41(1991)
- 15 <http://mems.isi.edu/archives/industry/microflow/MicroFlow1.html>
- 16 W. R.Groove : *Trans. Roy. Soc. London*, 142, p.87(1982), *Philos. Mag*, 5, p203(203) (quoted by J. J. Cuomo, S. M. Rossnagel and H. R. Kaufman "Hand book of ion beam processing technology", Noyes publications, p.78(1989))
- 17 M. Faraday : *Phil. Trans. Roy. Soc. London* 147, p.145(1857) (quoted by A. Kinbara "Sputtering phenomenon in Japanese", Tokyo university publisher, p.1(1984))
- 18 Karl-Heinz Muller : Summary abstract : Molecular dynamic and collision cascade studies of ion-assisted thin film deposition, *J. Vac. Technol.* A5(4), p.2161-2162(1987)
- 19 H. E. Roosendaal, U. Littmark and J. B. Sanders : Spatial distribution of recoiling atoms with a specific momentum generated in a collision, *Physical*

Review B, Vol.26, No.9, p.5261-5263(1982)

20 H. R. Kaufman : Fundamentals of ion-source operation, Commonwealth Science Corporation, p.60(1984)

21 H. R. Kaufman : Broad-Beam Ion Sources : Present Status and Future Directions, J. Vacuum Science and Technology A4, p.764-771(1986)

22 M. Kitabatake and K. Wasa : Growth of diamond at room temperature by an ion-beam sputter deposition under hydrogen-ion bombardment J. Appl. Phys. 58, p.1693-1695(1985)

23 H. Oechsner : Thin Film and Depth Profile Analysis, Springer, Berlin (1984)

24 A. V. Hippel and E. Blechschmidt : Ann. Phys, 81, p.999(1926); 81, p.1043(1926)

25 G. K. Wehner : Phys. Rev. 102, p.690(1956)

26 J. Fine : Physics of Ionized Gases 1980, Invited lectures, ed. By M. Matic, Boris Kidric Institute, Beograd, p.379-420(1980)

27 R. V. Stuart and G. K. Wehner : J. Appl. Phys., 33: 2345(1962)

28 K. Wasa and S. Hayakawa : Handbook of sputter deposition technology, Noyes Publications, p.50(1992)

29 A. W. Hull and H. F. Winter : Phys. Rev., 21, p.211(1923)

30 P. Sigmund : Phys. Rev., 184: p.383(1969)

31 G. K. Wehner : J. Appl. Phys., 30: p.1762(1959)

32 G. K. Wehner and D. L. Rosenberg : J. Appl. Phys., 31: p.177(1960)

- 33 T. Hoffmann, H. L. Dodds, M. T. Robinson and D. K. Holmes : Nucl. Sci. Eng., **68**, p.204(1978)
- 34 R. Seeliger and K. Sommermeyer : Z. Physik, **93**, p.692 (1935)
- 35 J. K. Robertson and C. W. Clapp : Nature **132**, p.479(1933)
- 36 L. I. Maissel, R. Glang : Handbook of Thin Film Technology, New York, McGraw Hill Inc., p.3-25(1970)
- 37 G. K. Wehner, D. L. Rosenberg: J. Appl. Phys., **31**, p.177(1960)
- 38 P. D. Davidse and L. I. Maissel : Trans. 3rd Intern. Vac. Congr., Stuttgart(1965)
- 39 P. D. Davidse and L. I. Maissel : J. Appl. Phys. **37**, p.574(1966)
- 40 F. M. Penning : U.S. Patent 2, 146, 025 (Feb. 1935)
- 41 W. D. Gill and E. Kay : Rev. Sci. Instrum., **36**, p.277(1965)
- 42 J. S. Chapin : Res./Dev., **25**, p.37(1974)
- 43 K. I. Kirov, N. A. Ivanov, E. D. Atansova and G. M. Minchev : Vacuum **26**, p.237(1976)
- 44 N. Hosokawa, T. Tsukada and T. Misumi : J. Vac. Sci. Technol. **14**, p.143(1977)
- 45 J. A. Thornton : J. Vac. Sci. Technol. **15**, 171, p.188(1978)
- 46 J. A. Thornton and A. S. Penfold : Thin Film Processes, ed. V. L. Vossen and W. Kern, Academic Press, New York, p.75(1978)
- 47 B. S. Danilen and V. K. Sirchin : Magnetron systems for ion sputtering of materials., Prib. Teck. Eksp., **4**, p.4-18(1978)

- 48 W. T. Pawlewicz, P. M. Martin, D. D. Hays and I. B. Mann : Recent developments in reactively sputtered optical thin films, Proc. Soc. Photo-Opt. Instrum. Eng. 325, p.105-116(1982)
- 49 S. D. Dahlgren, E. D. McClanahan, J. W. Johnston and A. G. Graybeal : J. Vac. Sci. Technol. 7, p.398(1970)
- 50 M.Matsuoka and K.Ono : Ohyobutsuri in Japanese, 57, p.1301(1988)
- 51 J. J. Cuomo, S. M. Rossnagel and H. R. Kaufman : Handbook of ion beam processing technology, Noyes Publications, p.362-368 (1989)
- 52 G. Carter and M. J. Nobes : The principle of a new method of determining ion beam profile density distribution, Vacuum, Vol.42, No.17, p.1125-1128(1991)
- 53 Gy. A. Nagy and M. Szilagyi : Introduction to the Theory of Space charge optics, 2nd ed. (Holsted, New York, 1974)
- 54 K. K. Foo, R. P. W. Lawson, X. Feng and W. M. Lau : Deceleration and ion beam optics in the regime of 10-200eV, J.Vac. Sci. Technol. A9 (2), Mar/Apr, p.312-316(1991)
- 55 K. Otsuka and C. M. Wayman : Shape memory materials, Cambridge University Press, p.87(1998)
- 56 T. Smy, L. Tan, S. S. Winterton, S. K. Dew and M. J. Brett : Simulation of sputter deposition at high pressures, J. Vac. Sci. Technol., A15, p.2847-2853(1997)
- 57 J. Dembowski, H. Oechsner, Y. Yamamura and M. Urbassek : Energy distributions of neutral atoms sputtered from Cu, V, Nb under different bombardment and ejection angles, Nuc. Inst. Meth., B18, p.464-470(1987)
- 58 G. M. Turner, I. S. Falconer, B. W. James and D. R. McKenzie ; Monte

Carlo calculations of the properties of sputtered atoms at a substrate surface in a magnetron discharge, *J.Vac. Sci. Technol.*, **A10**, p.455-461(1992)

59 N. Laegreid and G. K. Wehner : Sputtering yields of metals for Ar^+ and Ne^+ ions with energies from 50 to 600 eV, *Journal of Applied Physics*, **Vol.32**, No.3, p.365-369(1961)

60 E. G. Spencer and P. H. Schmidt : Ion-beam techniques for device fabrication, *Journal of vacuum science and technology* **Vol.8**, No.5, p.s52-s58(1971)

61 W. L. Benard, H. Kahn, A. H. Heuer and M. A. Huff : Thin-Film Shape-Memory Alloy Actuated Micropumps, *Journal of Microelectromechanical systems*, **Vol.7**, No.2, 245-251(1998)

62 K. Kuribayashi, S. Shimizu, T. Nishinohara and T. Taniguchi : Trial Fabrication of Micro sized Arm Using Reversible TiNi alloy Thin Film Actuators, *Proc. of the IEEE/RSJ International Conference on Intelligent Robots and Systems Yokohama, Japan, July 26-30*, p.1697-1702(1993)

63 M. MacKenzie, N. An, M. Giere, J. Stori and P. Wright : Experiences with shape memory alloy: robot grippers for sub-millimeter hard disk drive components, *SPIE Vol.2906*, p.25-36(1996)

64 A. P. Lee, D. R. Ciarlo, P. A. Krulevitch, S. Lehew and J. Trevino : A practical microgripper by fine alignment, eutectic bonding and SMA actuation, *Sensors and Actuators A54*, p.755-759(1996)

65 A. Gyobu, Y. Kawamura, H. Horikawa and T. Saburi : Martensitic Transformations in Sputter-Deposited Shape Memory Ti-Ni Films, *Materials Transactions Jim.*, **Vol.37**, No.4, p.697-702(1996)

66 Goodfellow Cambridge Ltd., Cambridge Science Park, Cambridge CB4 4DJ, UK

67 K. Tsuchiya and S. T. Davies : Fabrication of TiNi shape memory alloy

- microactuators by ion beam sputter deposition, *Nanotechnology*, **9**, p.67-71(1998)
- 68 J. D. Busch, A. D. Anderson, C. H. Lee and D. A. Stevenson : Shape-memory properties in Ti-Ni sputter deposited film, *J. Appl. Phys.*, **68**, 6224-6228 (1990)
- 69 A. D. Johnson : Vacuum-deposited TiNi shape memory film : characterization and applications in microdevices, *J. Micromech. Microeng.*, **1**, p.34-41 (1991)
- 70 K. R. C. Gisser, J. D. Busch, A. D. Johnson and A. B. Ellis : Oriented nickel-titanium shape memory alloy films prepared by annealing during deposition, *Appl. Phys. Lett.*, **61**, p.1632-1634 (1992)
- 71 H. Funakubo : Shape memory alloy in Japanese, Sangyoutosho, p.1(1984)
- 72 Y. Suzuki : Practical shape memory alloy in Japanese, Kougyoutyousakai, p.71(1987)
- 73 Y. Suzuki : Practical shape memory alloy in Japanese, Kougyoutyousakai, p.4(1987)
- 74 K. Ikuta, M. Hayashi, T. Matsuura and H. Fujishiro : Shape Memory Alloy Thin Film Fabricated by Laser Ablation, *Proc. IEEE Microelectromechanical Systems*, Oiso, Japan, p.355-360 (1994)
- 75 K. R. C. Gisser, J. D. Busch, A. D. Johnson and A. B. Ellis : oriented nickel-titanium shape memory alloy films prepared by annealing during deposition, *Appl. Phys. Lett.* **61**, **14**, p.1662-1634 (1992)
- 76 E. Quandt, C. Halene, H. Holleck, K. Feit, M. Kohl, P. Schloßmacher, A. Skokan and K.D. Skrobanek : Sputter deposition of TiNi, TiNiPd and TiPd films displaying the two-way shape-memory effect, *Sensors and Actuators A* **53**, p.434-439 (1996)

- 77 S. Miyazaki, K. Nomura and A. Ishida : Shape memory effects associated with the martensitic and R-phase transformations in sputter-deposited Ti-Ni thin film, *Journal de physique 5*, **C8**, p.677-682(1995)
- 78 Y. Nakata, T. Takagi, H. Sakamoto, A. Tanaka and K. Shimizu : Effect of heat treatments on morphology and transformation temperatures of sputtered Ti-Ni thin films, *Journal de physique 5*, **C8**, p.671-676(1995)
- 79 L. I. Maissel and R. Glang : Handbook of thin film technology, McGRAW-HILL BOOK Company, chapter.4, p.18(1970)
- 80 D. S. Grummon, L. Hou, Z. Zhao and T. J. Pence : Progress on sputter-deposited thermotractive titanium-nickel films, *Journal. de. Physique 4*, **C8**, 5, p.665-670, (1995)
- 81 P. Krulevitch, P. B. Ramsey, D. M. Makowiecki, A. P. Lee, M. A. Northrup and G.C.Johnson : Mixed-sputter deposition of Ni-TiCu shape memory films, *Thin Solid Films*, **274**, p.101-105(1996)
- 82 H. Holleck, S. Kirchner, E. Quandt, P. Schloßmacher, Preparation and characterization of TiNi SMA thin film, *Proc., Actuator 94*, 4th International Conference on New Actuators, 15-17 June Bremen, Germany, p.361-364(1994)
- 83 C. Huang and W. Y. Lee : X-ray fluorescence and reflectivity analysis of multiple-layer thin films, *Analytical Sciences*, **11**, p.529-532 (1995)
- 84 D. K. G. de Broer, A. J. G. Leenaers and W.W. van den Hoogenhof : Glancing-incidence x-ray analysis of thin-layered materials : a review, *X-ray Spectrometry*, **24**, p.91-102 (1995)
- 85 H. Kiessing : *Ann. Phys. (Leipzig)*10,769(1931) (quoted by D. K.G. de Boer, A.J.G.Leenaers and W.W. van den Hoogenhof "Glancing-incidence x-ray analysis of thin-layered materials : a review, *X-ray Spectrometry*, **24**, p.91-102 (1995)")

- 86 K. Ikuta, H. Fujita, M. Ikeda and S. Yamashita : Crystallographic analysis of TiNi shape memory alloy thin film for micro actuator, IEEE, p.38-39(1990)
- 87 M. Kohl, K. D. Skrobanek, C. M. Goh and D. M. Allen : Mechanical characterisation of shape memory micromaterials, SPIE proc., Vol.2880, P.108-118(1996)
- 88 Y. Q. Yang, H. S. Jia, Z. F. Zhang, H. M. Shen, A.Hu, Y. N. Wang : Transformations in sputter-deposited thin films of TiNi shape memory alloy, Material Letters 22, p.137-140(1995)
- 89 E. Makino, M. Uenoyama and T. Shibata : Flash evaporation of TiNi shape memory thin film for microactuators, Sensors and Actuators, A71, P.187-192(1998)
- 90 K. Kuribayashi, S. Shimizu, M. Yoshitake and S. Ogawa : Fabrication and transformation characteristics of reversible shape memory alloy thin film actuators, JSPE, Vol.63, No.4, p.530-539(1997)
- 91 M. Kohl, K. D. Skrobanek, E. Quandt, P. Schloßmacher, A. Schüßler and D. M. Allen : Development of microactuators based on the shape memory effect, J.de Physique IV, C8, p.1187-1192(1995)
- 92 C. M.Jackson, H. J. Wagner and R. J. Wasilewski, "55-Nitinol - The alloy with a memory : Its physical metallurgy, properties and applications", NASA Report, SP 5110 (1972)
- 93 Cedip SA, 19 Bd G. Bidault F-77183 Croissy Beaubourg, France
- 94 D. P. Dautovich, Z. Melkvi, G. R. Purdy and C. V. Stager : Calorimetric study of a diffusionless phase transition in TiNi, J. Appl. Phys., Vol.37, p.2513-2514(1966)
- 95 S. T. Davies and K. Tsuchiya : Growth and characterisation of shape memory alloy thin films for micropositioning and microactuation, SPIE Vol.3511, p.174-182 (1998)

Bibliography

1. J. J. Cuomo, S. M. Rossnagel and H. R. Kaufman : Handbook of ion beam processing technology, Noyes Publications (1989)
2. K. Wasa and S. Hayakawa : Handbook of deposition sputter deposition technology, Noyes Publications (1992)
3. K. Otsuka and C. M. Wayman : Shape memory materials, Cambridge University Press (1998)

Paper published

1. S. T. Davies, D. A. Hayton and K. Tsuchiya : Fabrication of microstructures by ion beam micromachining, SPIE Vol.2880, p.248-255(1996)
2. S. T. Davies and K. Tsuchiya : Ion sputter deposition of shape memory alloy films for microactuators, SPIE Vol.3223, p.160-167(1997)
3. S. T. Davies and K. Tsuchiya : Growth and characterisation of shape memory alloy thin films for micropositioning and microactuation, SPIE Vol.3511, p.174-182 (1998)
4. K. Tsuchiya and S. T. Davies : Fabrication of TiNi shape memory alloy microactuators by ion beam sputter deposition, Nanotechnology, 9, p.67-71 (1998).
5. S. T. Davies and K. Tsuchiya : TiNi Shape Memory Alloy Thin Films for Micromanipulation and Microactuation, EUSPEN (1999) in press